The performance of the ATLAS missing transverse momentum high-level trigger in 2015 pp collisions at 13 TeV

by

Justin Chiu
B.Sc., University of Victoria, 2014

A Thesis Submitted in Partial Fulfillment of the
Requirements for the Degree of

MASTER OF SCIENCE

in the Department of Physics and Astronomy

The performance of the ATLAS missing transverse momentum high-level trigger in 2015 pp collisions at 13 TeV

by

Justin Chiu
B.Sc., University of Victoria, 2014

Supervisory Committee

Dr. R. Kowalewski, Supervisor
(Department of Physics and Astronomy)

Dr. R. Sobie, Departmental Member
(Department of Physics and Astronomy)

Supervisory Committee

Dr. R. Kowalewski, Supervisor
(Department of Physics and Astronomy)

Dr. R. Sobie, Departmental Member
(Department of Physics and Astronomy)

ABSTRACT

The performance of the ATLAS missing transverse momentum ($E_{\mathrm{T}}^{\mathrm{miss}}$) high-level trigger during 2015 operation is presented. In 2015, the Large Hadron Collider operated at a higher centre-of-mass energy and shorter bunch spacing ($\sqrt{s} = 13\,\mathrm{TeV}$ and 25 ns, respectively) than in previous operation. In future operation, the Large Hadron Collider will operate at even higher instantaneous luminosity ($\mathcal{O}(10^{34}\,\mathrm{cm}^{-2}\,\mathrm{s}^{-1})$) and produce a higher average number of interactions per bunch crossing, $\langle\mu\rangle$. These operating conditions will pose significant challenges to the $E_{\mathrm{T}}^{\mathrm{miss}}$ trigger efficiency and rate. An overview of the new algorithms implemented to address these challenges, and of the existing algorithms is given. An integrated luminosity of $1.4\,\mathrm{fb}^{-1}$ with $\langle\mu\rangle = 14$ was collected from pp collisions of the Large Hadron Collider by the ATLAS detector during October and November 2015 and was used to study the efficiency, correlation with offline reconstruction, and rates of the trigger algorithms. The performance was found to be satisfactory. From these studies, recommendations for future operating specifications of the trigger were made.

Contents

List of Figures

ACKNOWLEDGEMENTS

First, I would like to thank my supervisor, **Dr. Robert Kowalewski**, not only for his advice and expertise, but also for opening doors during my MSc. Through Bob, I met **Dr. Florian Bernlochner**, who I thank for supervising my first studies of the $E_{\mathrm{T}}^{\mathrm{miss}}$ trigger and for teaching me about the online $E_{\mathrm{T}}^{\mathrm{miss}}$ trigger software. I would also like to thank the members of the ATLAS $E_{\mathrm{T}}^{\mathrm{miss}}$ trigger group for their useful feedback on my studies. Finally, I would like to thank **Dr. Randall Sobie** for acting as a committee member throughout my MSc and **Dr. Peter Driessen** for acting as the external examiner.

DEDICATION

To Mom and Dad, and KM, NL, MT, and TK.

Chapter 1

Introduction

The missing transverse momentum ($E_{\mathrm{T}}^{\mathrm{miss}}$) [1] trigger is an essential component of the ATLAS detector at the Large Hadron Collider (LHC). $E_{\mathrm{T}}^{\mathrm{miss}}$ is a signature for processes involving weakly-interacting particles such as neutrinos, dark matter, and supersymmetry particles. The data selected by the $E_{\mathrm{T}}^{\mathrm{miss}}$ trigger has been used in searches for dark matter [1, 2], supersymmetry [3, 4], Higgs boson decay processes [5, 6], and precision measurements [7, 8]. Bunches of protons accelerated by the LHC collide in the ATLAS detector every 25 ns and produce multiple simultaneous proton-proton interactions. In every second of operation, the $E_{\mathrm{T}}^{\mathrm{miss}}$ trigger must select $\mathcal{O}(100)$ particle collision events containing $E_{\mathrm{T}}^{\mathrm{miss}}$ from millions of such events for further analysis.

The key characteristics of the $E_{\mathrm{T}}^{\mathrm{miss}}$ trigger are the overall rate at which it accepts collision events, which is constrained by bandwidth and computational costs, and the efficiency at which it accepts events with genuine $E_{\mathrm{T}}^{\mathrm{miss}}$, which is strongly affected by backgrounds.

Unfortunately, $E_{\mathrm{T}}^{\mathrm{miss}}$ also arises from imperfect measurement of detected particles and particles that escape the detector's coverage. These instrumental backgrounds on $E_{\mathrm{T}}^{\mathrm{miss}}$ are increased when the proton beam intensity (*luminosity*) and energy are increased and the time between colliding bunches of protons is decreased. During "Run-2" of the LHC (years 2015 to 2018), the collider will operate at up to double the luminosity and energy of previous operation ($10^{34}\,\mathrm{cm}^{-2}\,\mathrm{s}^{-1}$ and centre-of-mass energy $\sqrt{s} = 13\,\mathrm{TeV}$, respectively). These operating conditions will pose significant

[1] Missing transverse momentum is synonomous with *missing transverse energy* and with the acronyms *MET* and $E_{\mathrm{T}}^{\mathrm{miss}}$. It is calculated from the projection onto the plane transverse to the beam axis of *energy* deposits; hence it is sometimes referred to as missing transverse energy.

challenges to the $E_{\mathrm{T}}^{\mathrm{miss}}$ trigger.

The main objective of this thesis is to study the performance of the $E_{\mathrm{T}}^{\mathrm{miss}}$ trigger in 2015 operation. This was done by measuring the efficiency and correlation of the $E_{\mathrm{T}}^{\mathrm{miss}}$ trigger against the more-refined $E_{\mathrm{T}}^{\mathrm{miss}}$ calculation done post-trigger, and measuring the rate at which collision events trigger the $E_{\mathrm{T}}^{\mathrm{miss}}$ trigger. Each study was done on an algorithm-by-algorithm basis to facilitate the comparison of $E_{\mathrm{T}}^{\mathrm{miss}}$ trigger algorithms. The results of these studies provide guidelines on future operation of the $E_{\mathrm{T}}^{\mathrm{miss}}$ trigger.

The outline of this thesis is as follows. Chapter 2 will elaborate further on the origins of missing transverse momentum. Chapter 3 will give an overview of the Large Hadron Collider and the ATLAS detector, with particular attention to calorimeter topological clustering and calorimeter calibration as they pertain to $E_{\mathrm{T}}^{\mathrm{miss}}$. Chapter 4 will focus on the layout of the $E_{\mathrm{T}}^{\mathrm{miss}}$ trigger, the high-level $E_{\mathrm{T}}^{\mathrm{miss}}$ trigger algorithms, and the offline reconstruction algorithm. Chapter 5 will detail the data samples used, the event selection criteria, and the signal selection criteria. Chapter 6 will present and discuss the results of the performance studies on the data sample. Chapter 7 summarizes the conclusions drawn from the studies on 2015 operation. The contributions by the author to the $E_{\mathrm{T}}^{\mathrm{miss}}$ trigger and monitoring software are detailed in Appendix A.

Chapter 2

Missing transverse momentum

2.1 Overview

The law of momentum conservation states that the momentum of a system is constant if there are no external forces acting on the system. In the context of *proton-proton* collisions – such as those at the Large Hadron Collider – the law implies that the net momentum of the incoming *partons* (the constituents of protons) should equal the net momentum of the outgoing products. An apparent imbalance in net momentum can result if the outgoing products contain particles that escape the detector's coverage, or are invisible to the detector. $E_{\mathrm{T}}^{\mathrm{miss}}$ is used as a signature for particle production processes that are predicted to produce particles that are invisible to the detector. Imperfect measurement of detected particles can also produce an apparent imbalance.

Imbalances are measured in the transverse plane of the detector. In a *pp* collision, the distribution of longitudinal momentum (i.e. along the beam axis) between the partons of each proton is unknown. Consequently, the net longitudinal momentum of the partons that interact and produce outgoing products is unknown. However, the *transverse* momentum of the incoming protons and their constituents is given by the scale of the parton momenta in the rest frame of the protons and is typically smaller than the proton mass (938 MeV). Therefore, a net transverse momentum of the outgoing products that is substantially above this scale indicates an apparent imbalance and is referred to as *missing transverse momentum* ($E_{\mathrm{T}}^{\mathrm{miss}}$).

$E_{\mathrm{T}}^{\mathrm{miss}}$ is calculated by vectorially projecting the energy of the detected objects, E_i, onto the transverse plane and then vectorially summing over the projections as shown

in Eqs. 2.1 and 2.2 [1] (the angles θ and ϕ are defined in the following paragraph).

$$\begin{aligned} E_x^{\text{miss}} &= -\sum_i E_i \sin\theta_i \cos\phi_i \\ E_y^{\text{miss}} &= -\sum_i E_i \sin\theta_i \sin\phi_i \end{aligned} \tag{2.1}$$

$$\overrightarrow{E_{\text{T}}^{\text{miss}}} = (\sqrt{E_x^{\text{miss}2} + E_y^{\text{miss}2}}, \tan^{-1}\frac{E_y^{\text{miss}}}{E_x^{\text{miss}}}) \tag{2.2}$$

ATLAS uses a right-handed coordinate system with its origin at the nominal interaction point (IP) in the centre of the detector and the z-axis along the beam pipe. The x-axis points from the IP to the centre of the LHC ring, and the y-axis points upward. Cylindrical coordinates (r, ϕ) are used in the transverse plane with ϕ being the azimuthal angle around the z-axis. The pseudorapidity is defined in terms of the polar angle θ as $\eta = -\ln\tan(\theta/2)$. Differences in pseudorapidity are invariant under Lorentz boosts along the longitudinal (beam) axis. This feature makes pseudorapidity useful since the longitudinal boosts of each centre-of-mass frame are unknown (as described above). Quantities such as the angular separation of two objects – given in $\Delta\eta$ and $\Delta\phi$ – can be compared without concern that their centre-of-mass frames may have been boosted by different amounts with respect to the frame of the detector.

A visualization of an event containing $E_{\text{T}}^{\text{miss}}$ is shown in Fig. 2.1.

Fluctuations in the measurement of the energies E_i that constitute $E_{\text{T}}^{\text{miss}}$ lead to a non-zero $E_{\text{T}}^{\text{miss}}$ resolution. This resolution is proportional to $\sqrt{\Sigma E_{\text{T}}}$ (the scalar sum of energy deposits projected onto the transverse plane). Energy contributions from background will broaden the resolution and detrimentally affect $E_{\text{T}}^{\text{miss}}$. The resolution of the energies E_i have non-Gaussian tails that lead to non-Gaussian contributions to the resolutions of E_x^{miss}, E_y^{miss}, and subsequently to distributions of $E_{\text{T}}^{\text{miss}}$.

The goal of the ATLAS $E_{\text{T}}^{\text{miss}}$ trigger is to select – in real-time – events containing physically significant $E_{\text{T}}^{\text{miss}}$. Due to computational constraints, only a few hundred collision events per second can be stored for further analysis, and $E_{\text{T}}^{\text{miss}}$ must be calculated using less sophisticated and computationally inexpensive algorithms. At the offline level, analysts have the liberty of unrestricted computing resources and can consequently use the most sophisticated reconstruction algorithms to optimally

[1] The x- and y- components of $E_{\text{T}}^{\text{miss}}$ are equal to the negatives of the E_x and E_y sums, and are summed in quadrature to give the magnitude of $E_{\text{T}}^{\text{miss}}$, which is therefore always positive.

reconstruct $E_{\mathrm{T}}^{\mathrm{miss}}$.

The ATLAS $E_{\mathrm{T}}^{\mathrm{miss}}$ trigger in "Run-2" comprises of two levels: Level-1 (L1) and the high-level trigger (HLT). The L1 computes, for every collision event, a rough estimate of the $E_{\mathrm{T}}^{\mathrm{miss}}$ in the event using coarse calorimeter quantities. If the amount of $E_{\mathrm{T}}^{\mathrm{miss}}$ determined by the L1 trigger exceeds a pre-defined threshold, the detector information is transferred from the on-detector electronics to the HLT-dedicated computer farm, where a more refined estimate of the $E_{\mathrm{T}}^{\mathrm{miss}}$ is computed using more granular calorimeter quantities and more sophisticated algorithms. If the amount of $E_{\mathrm{T}}^{\mathrm{miss}}$ determined by the HLT trigger exceeds a pre-defined threshold, the full detector information is written to disk for offline reconstruction at a later time.

At a fixed threshold on the minimum amount of $E_{\mathrm{T}}^{\mathrm{miss}}$ present in an event, the rate at which events are accepted by the trigger increases rapidly as the luminosity and energy of the proton beams are increased. The increase in trigger rate must be controlled by either increasing the thresholds or by improving the $E_{\mathrm{T}}^{\mathrm{miss}}$ trigger algorithms. Increasing thresholds is undesirable since higher thresholds reduce sensitivity to the physics of interest. Some production processes may produce $E_{\mathrm{T}}^{\mathrm{miss}}$ that is lower than or close to a threshold and may go undetected. The primary measure of how well the $E_{\mathrm{T}}^{\mathrm{miss}}$ triggers on $E_{\mathrm{T}}^{\mathrm{miss}}$ originating from signals of interest is its *efficiency*. The efficiencies of the $E_{\mathrm{T}}^{\mathrm{miss}}$ trigger in 2015 operation will be shown and discussed in Ch. 6.

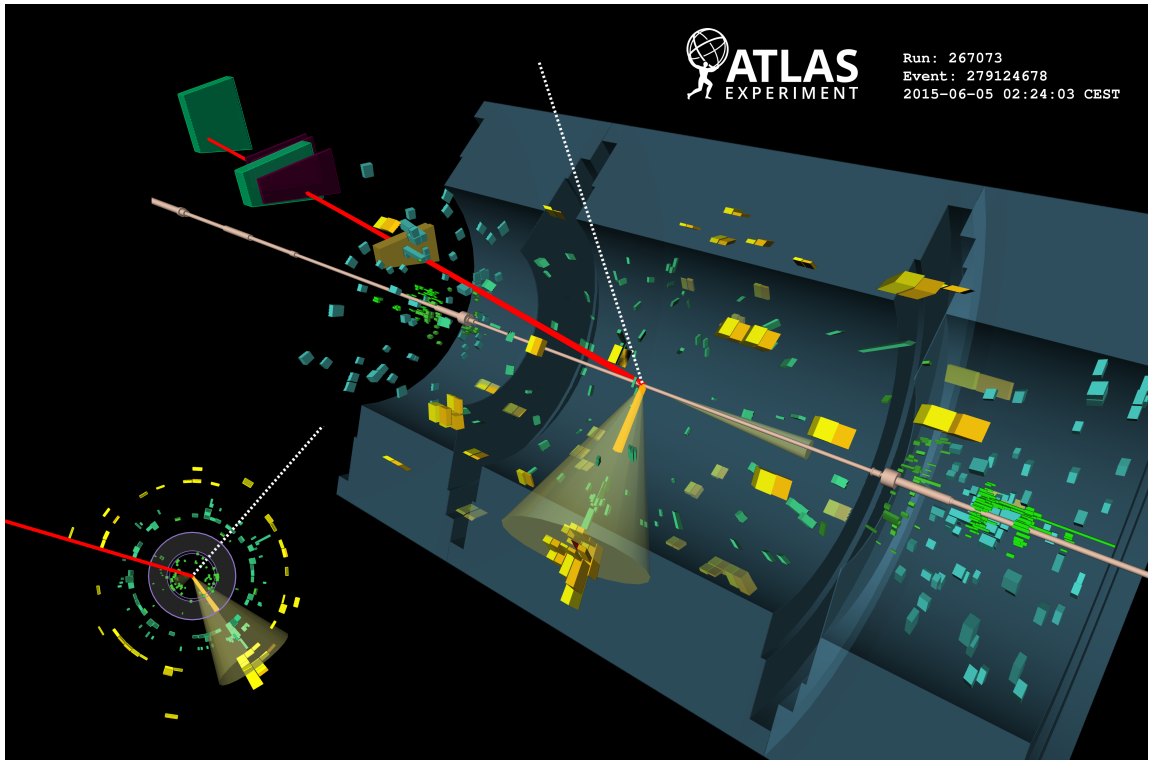

Figure 2.1: Display of event 279124678 in run 267073 recorded on June 5th, 2015 [9]. The topology of this event corresponds to t-channel single top quark production in the muon plus jets channel. The missing transverse momentum, represented by the dotted white line, has a magnitude of $\sim 40\,\text{GeV}$. The reconstructed muon represented by the red line has a transverse momentum (p_T) of $\sim 30\,\text{GeV}$. The green and yellow bars indicate energy deposits in the liquid argon (LAr) and tile calorimeters. From these deposits, two jets have been identified and are contained within the yellow cones. The central jet, with a transverse momentum of $\sim 50\,\text{GeV}$, is identified as having originated from a b-quark (also known as a *b-jet*). The forward jet, with a transverse momentum of $\sim 30\,\text{GeV}$, is close to the beam pipe.

2.2 Production processes

Numerous pp collision processes produce particles that result in genuine $E_{\mathrm{T}}^{\mathrm{miss}}$. Collisions that produce particles that are invisible to the ATLAS detector, such as neutrinos (ν), dark matter, and certain supersymmetric particles will produce $E_{\mathrm{T}}^{\mathrm{miss}}$. These particles are commonly referred to as *weakly-interacting particles*.

$E_{\mathbf{T}}^{\mathbf{miss}}$ from Standard Model production

A Standard Model process that produces genuine $E_{\mathrm{T}}^{\mathrm{miss}}$ is the decay of a W boson to a lepton and neutrino. From the reference frame of the W boson, the lepton and neutrino should have zero net momentum. In both $W \to e\nu$ and $W \to \mu\nu$, the neutrino escapes undetected due to its weak interaction. In the former case, the electron is identified in the calorimeter, and in the latter case, the muon is identified in the muon spectrometer.

While charged leptons (muons, electrons, and taus) can be detected by ATLAS, neutral leptons (neutrinos) cannot be. Another Standard Model process that frequently produces neutrinos is the decay of the Z boson. It decays to two neutrinos roughly 20% of the time [10].

$E_{\mathbf{T}}^{\mathbf{miss}}$ from dark matter production

Dark matter (DM) particles, as the name implies, neither absorb nor emit any electromagnetic radiation. Their existence has been confirmed by studies of gravitational lensing, the cosmic microwave background, and galaxy rotation curves. Because of their extremely weak interaction (or lack thereof), they cannot be directly detected by the ATLAS detector. However, it should be possible to observe them if they are produced alongside Standard Model (SM) particles. In this scenario, SM particles are observed as recoiling against one or more invisible particles. The result is $E_{\mathrm{T}}^{\mathrm{miss}}$, since the momenta of the SM particles is measured but the momenta of the DM particles is not, thus leading to a non-zero net transverse momentum. These models are commonly referred to as "mono-X" models, where X is the SM particle (a jet or a decaying W or Z boson).

$E_{\mathrm{T}}^{\mathrm{miss}}$ from supersymmetric particle production

In theories of supersymmetry, the *lightest stable supersymmetric particle* (LSP) is theorized to interact weakly and consequently would be invisible to the ATLAS detector. Decays of supersymmetric particles into LSP(s) would produce $E_{\mathrm{T}}^{\mathrm{miss}}$ in association with SM particles much in the same way that DM particles would produce $E_{\mathrm{T}}^{\mathrm{miss}}$.

2.3 Pileup and other background effects

To increase the number of physically significant events detected and to probe physics at a higher energy scale, the LHC operated in 2015 with higher instantaneous luminosity and energy and shorter bunch spacing than in previous operation. By reducing the bunch spacing, the average number of interactions per bunch crossing, $\langle\mu\rangle$, decreases. In 2015, the LHC operated at the same instantaneous luminosity as in 2012 ($\mathcal{O}(5 \times 10^{33}\,\mathrm{cm}^{-2}\,\mathrm{s}^{-1})$), but with a shorter bunch spacing (25 ns versus 50 ns). This resulted in a decrease in $\langle\mu\rangle$ from 20 to 14. Since the shortest bunch spacing that can be delivered by the LHC is 25 ns, the *specific luminosity* will have to be increased in order to achieve a higher instantaneous luminosity in future operation. In other words, the intensity of collisions between each pair of bunches will have to be increased, instead of decreasing the spacing between bunches. Consequently, $\langle\mu\rangle$ will increase in future operation of the LHC in order to achieve higher instantaneous luminosity. This increase in $\langle\mu\rangle$ leads to an increase in background effects.

The background effects originating from multiple interactions occurring in the same bunch crossing are commonly referred to as "pileup". Pileup can be divided into two types: in-time, and out-of-time. As their names imply, they arise from the triggered bunch crossing and from previous and future bunch crossings. An explanation of these backgrounds follows.

In-time pileup

As shown in Figs. 2.2 and 2.3, processes have production cross-sections that scale with centre-of-mass energy. For example, the total Standard Model (SM) Higgs Boson production cross-section is approximately three times larger at $\sqrt{s} = 13\,\mathrm{TeV}$ than it is at $\sqrt{s} = 7\,\mathrm{TeV}$. These processes originate from collisions with high momentum transfer (hard scatters). The majority of collisions have low momentum transfer (soft scatters) and represent so-called inelastic "soft QCD" processes. These processes dominate the

$pp \to X$ cross-section and are represented in Fig. 2.2 as the inelastic cross-section as a function of centre-of-mass energy. In the presence of a hard scatter collision, soft scatters give rise to a significant background and are the dominant source of *in-time pileup*. The average of the Poisson mean of the number of interactions per bunch crossing, $\langle\mu\rangle$, is a linear measure of in-time pileup. Shown in Fig. 2.4 is the distribution of μ during 2015 pp collision data taking. A visualization of an event with multiple pp collisions is shown in Fig. 2.5.

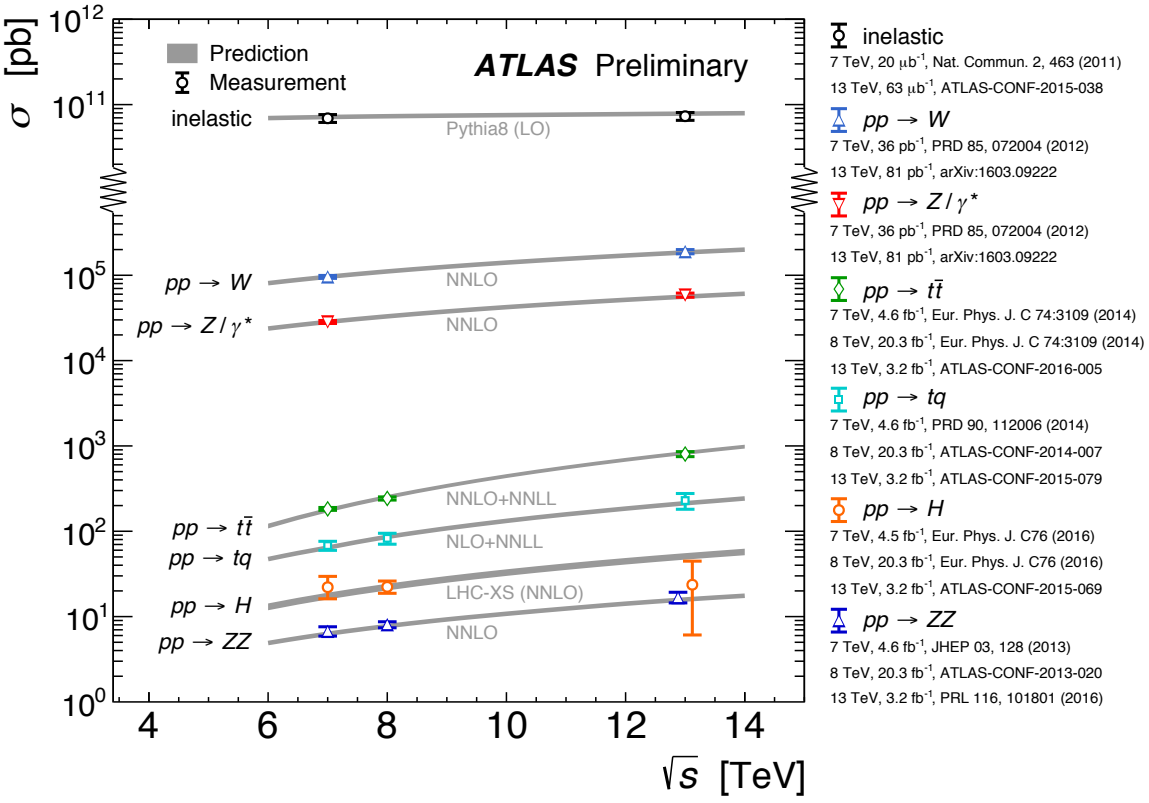

Figure 2.2: Standard Model production cross-section simulations and measurements by ATLAS presented as a function of centre-of-mass energy $\sqrt{s}$ from 7 TeV to 13 TeV for selected processes [11].

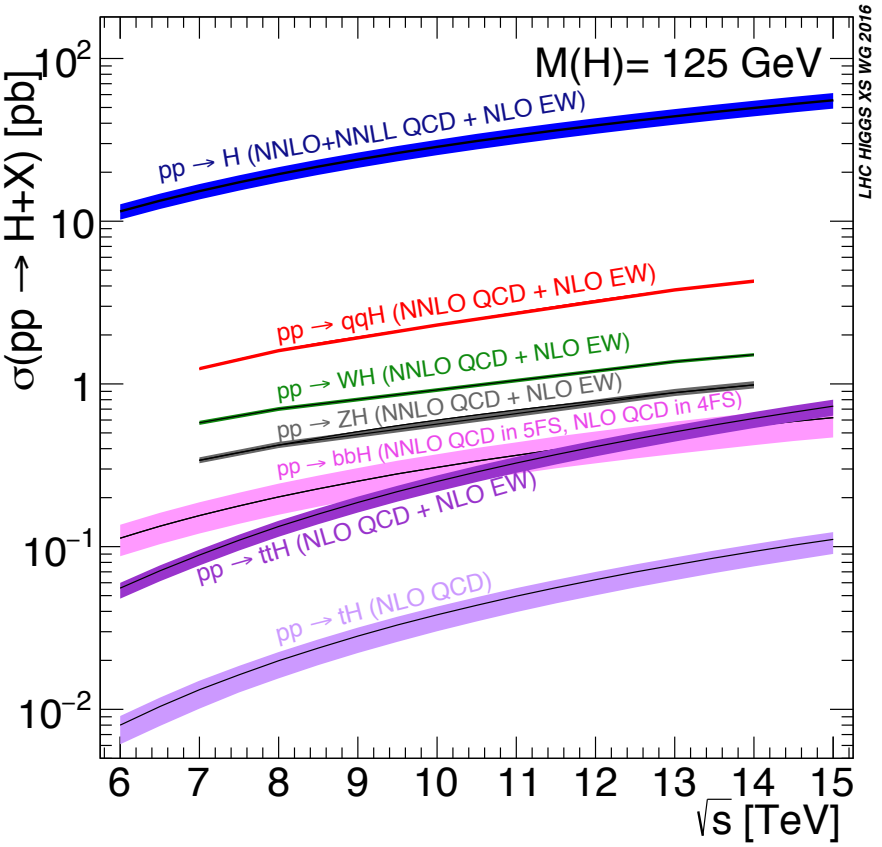

Figure 2.3: Standard Model Higgs boson production cross-sections as a function of centre-of-mass energy (calculated from simulation) [12].

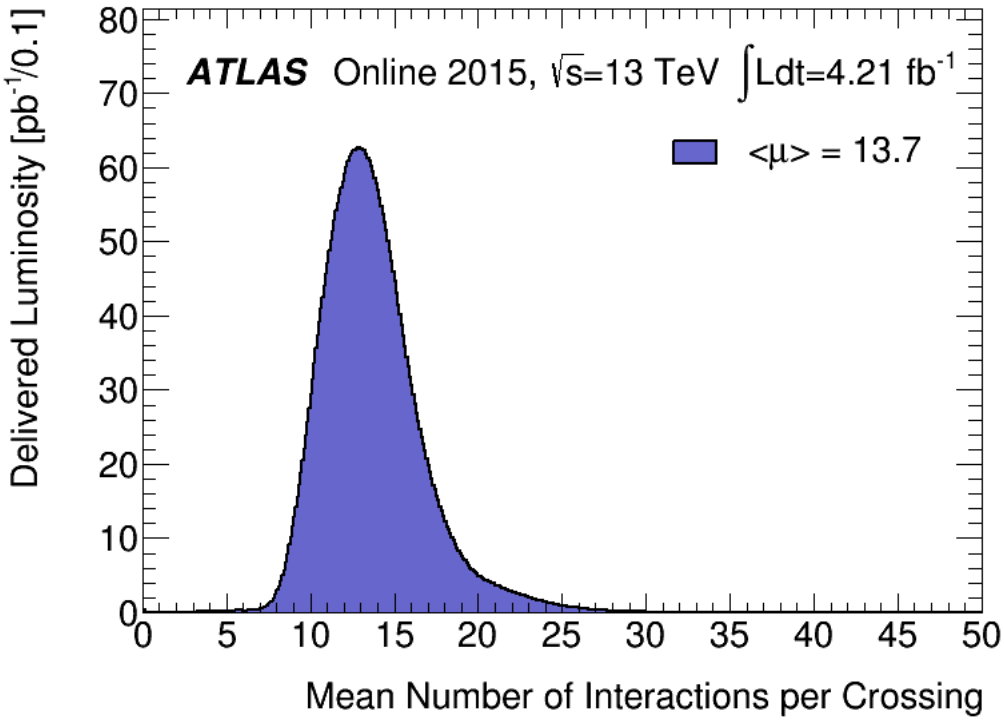

Figure 2.4: Distribution of μ during 2015 pp collision data taking [13].

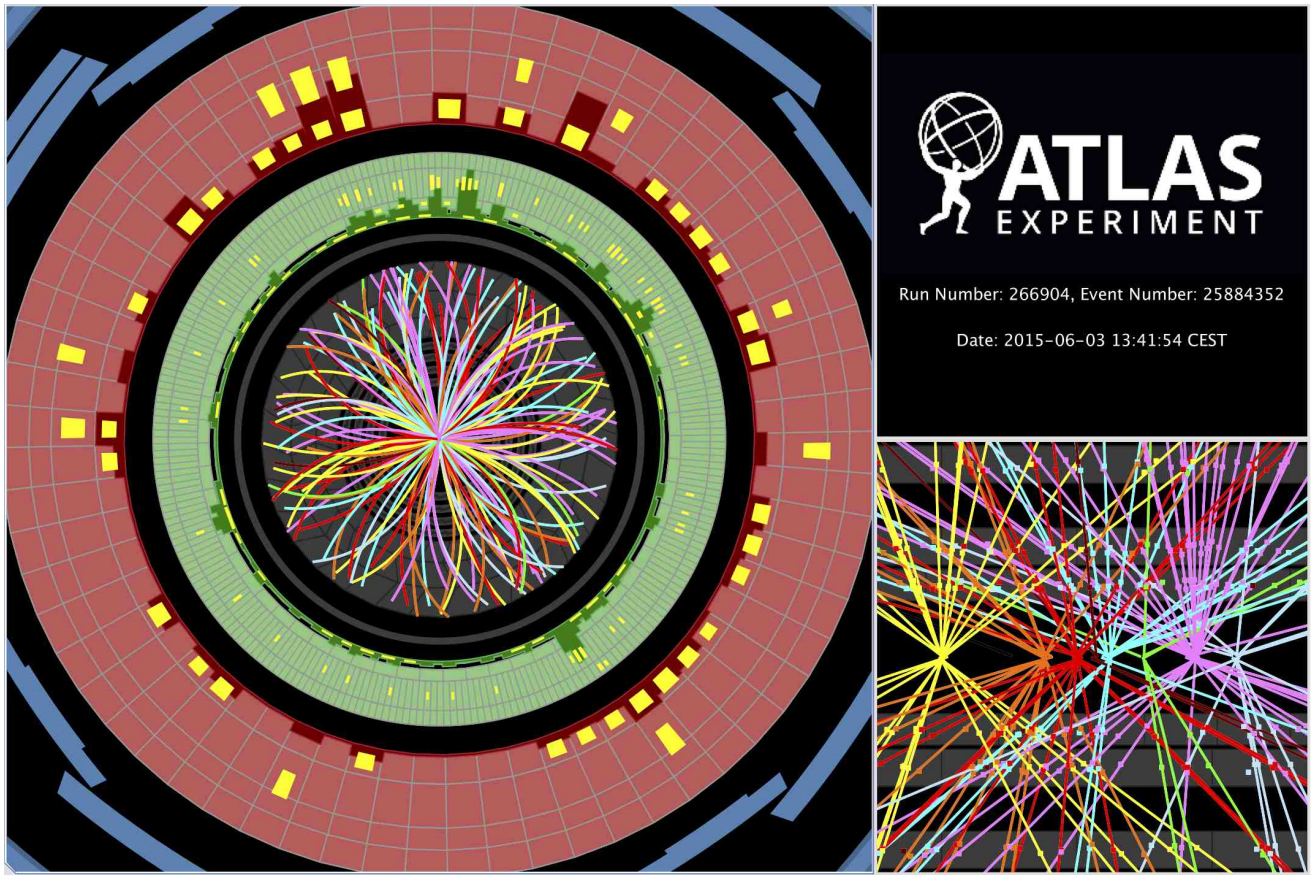

Figure 2.5: Display of event 25884352 in run 266904 recorded on June 3rd, 2015 [9]. In the left panel, tracks reconstructed from hits in the Inner Detector (ID) are shown as arcs curving in the solenoidal magnetic field of the detector. Tracks represent the trajectory of charged particles and originate from vertices, each of which represent a pp collision. The colour assigned to each track represents the vertex from which the track originated from. The yellow rectangles, along with the red and green bars, indicate energy deposits in the liquid argon (LAr) and scintillating-tile calorimeters. In the bottom right panel, tracks are shown to be originating from different vertices and indicate the presence of multiple pp collisions (pileup) in one event.

In a hard scatter, typically only one parton from each proton interacts. However, the interaction of multiple partons originating from the same hard scatter is possible. This type of interaction – *multi-parton interaction* (MPI) – gives rise to another source of in-time pileup. MPI produces an *underlying event* that is dominated by soft QCD processes.

Aside from the energy deposited in the calorimeter by the hard scatter products, soft scatter products deposit additional energy and give rise to an overall increase in the amount of energy deposited and fluctuations in the amount of recorded energy. This leads to an increase in $E_{\mathrm{T}}^{\mathrm{miss}}$ and consequently an increase in the number of events that pass a certain $E_{\mathrm{T}}^{\mathrm{miss}}$ threshold, and also broadens the $E_{\mathrm{T}}^{\mathrm{miss}}$ resolution. $E_{\mathrm{T}}^{\mathrm{miss}}$ from pileup is uniformly distributed over ϕ, and within the pseudorapidity covered by ATLAS ($-5 < \eta < 5$). Note that even in events where there are no hard scatters, the imperfect (i.e. non-zero) resolution gives rise to $E_{\mathrm{T}}^{\mathrm{miss}}$.

The impact of in-time pileup is mitigated by calorimeter clustering and $E_{\mathrm{T}}^{\mathrm{miss}}$ trigger algorithms. Calorimeter clustering attempts to reduce the impact of signal fluctuations arising from pileup and electronic noise by identifying calorimeter cells with signals passing pre-defined thresholds and grouping them together. Calorimeter clustering is described in Ch. 3.2.3.

Out-of-time pileup

Due to strict requirements on calorimeter signal timing and signal precision, calorimeter signal pulses are shaped by differentiation and integration to create a "bi-polar" pulse with zero net area. These pulses consist of a positive peak followed by a negative tail. The duration of each pulse is longer than the time between bunch crossings (indicated by the dots at 25 ns intervals in Fig. 2.6). Consequently, the signals overlap constructively or destructively between consecutive bunches. This affects the measurement of the energy recorded within each bunch crossing and consequently the measurement of $E_{\mathrm{T}}^{\mathrm{miss}}$. This effect, commonly referred to as *out-of-time pileup*, is mitigated by calorimeter signal shaping and by (dynamic) pedestal correction applied by the L1 calorimeter trigger (refer to Appendix A).

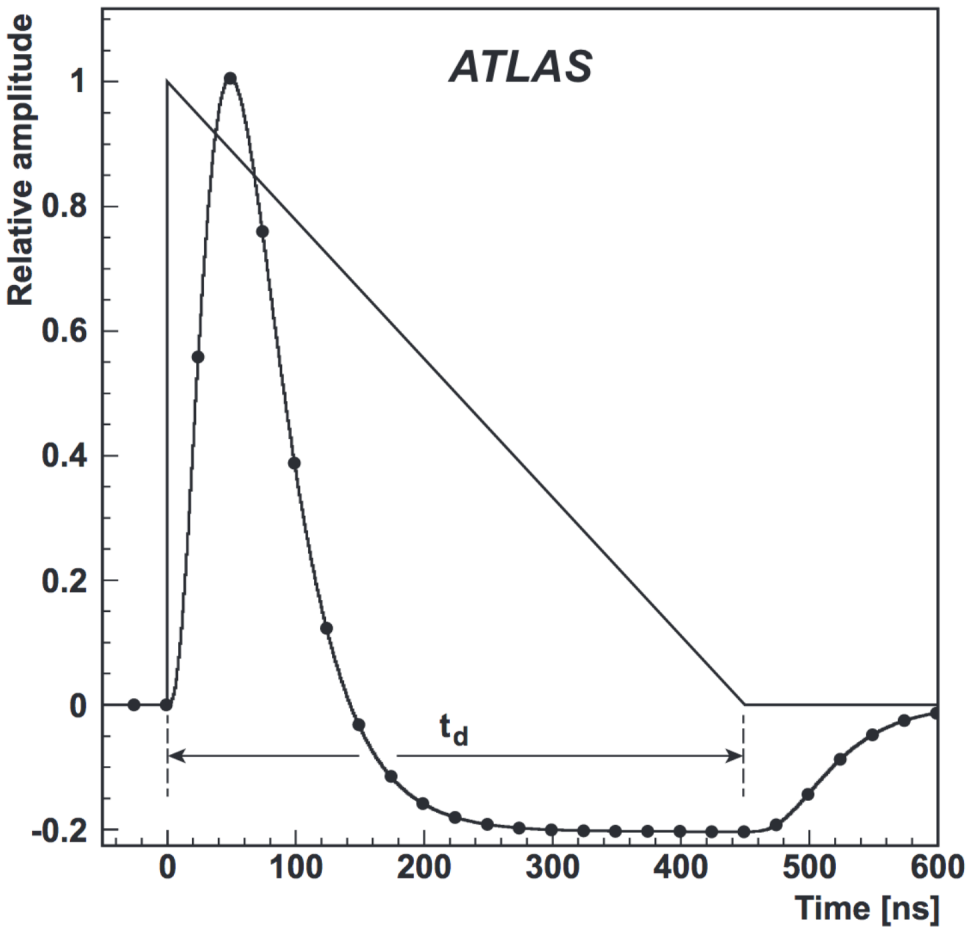

Figure 2.6: Pulse shape in the ATLAS LAr calorimeter [14]. The triangular pulse is the current pulse generated by the ionizing particle. t_d is the duration for which charge is collected from the ionization. The shaped pulse is superimposed.

Electronic noise

While the main background to genuine $E_{\mathrm{T}}^{\mathrm{miss}}$ is pileup, calorimeter noise – in the form of electronic noise and spurious signals – also forms a background to $E_{\mathrm{T}}^{\mathrm{miss}}$. Contrary to in-time pileup, electronic noise is largely independent of $\langle\mu\rangle$. This background is mitigated by calorimeter cell noise thresholds, calorimeter clustering, and noise suppression applied by the L1 calorimeter trigger.

Chapter 3

LHC and ATLAS

This chapter describes the ATLAS detector and the Large Hadron Collider (LHC). The protons produced and accelerated by the LHC are collided inside ATLAS and three other detectors. The ATLAS detector consists of multiple sub-detectors designed to accurately reconstruct particles produced in the collisions and measure properties of the collision such as $E_{\mathrm{T}}^{\mathrm{miss}}$. The reconstructed particles are commonly referred to as "objects". Reconstructing objects entails measuring their momentum, energy, and other properties. Data collected by ATLAS, consisting of objects reconstructed from collisions and event-level quantities such as $E_{\mathrm{T}}^{\mathrm{miss}}$, was used in this thesis to study the performance of the $E_{\mathrm{T}}^{\mathrm{miss}}$ trigger.

3.1 Large Hadron Collider

The Large Hadron Collider is currently the world's most powerful particle accelerator. It is situated, on average, 100 m underground and has a circumference of approximately 27 km. Protons are accelerated by a series of smaller accelerators (*Linac 2*, *Proton Synchrotron Booster*, *Proton Synchrotron*, and the *Super Proton Synchrotron*) before they are injected into the LHC, where they are boosted to a final energy of 6.5 TeV per proton beam. Sixteen radiofrequency cavities situated along the beam pipes accelerate the particles and 1232 dipole and 392 quadrupole magnets guide and focus the beams.

The two counter-rotating beams are focused and collided at four interaction points along the circumference of the LHC. At each interaction point, a detector observes

the resulting *pp* or *Pb-Pb* (heavy ion) collisions [1]. Two of the detectors – ATLAS and CMS – are general purpose detectors that were designed to be sensitive to a wide range of physics phenomena at the TeV scale. The two other detectors are more specialized: ALICE was designed to study heavy ion physics and LHCb was designed to study b-physics (the physics of particles containing b-quarks).

Each 6.5 TeV proton beam contains ~ 2232 proton bunches and each bunch contains $\sim 1.1 \times 10^{11}$ protons. Every 25 ns, bunches are collided ("crossed") at the four interaction points along the circumference of the LHC to produce collisions. This time interval is commonly referred to as the *bunch spacing*.

The instantaneous luminosity quantifies the ability of a collider to produce interactions and is defined as the ratio of the number of events per second to the cross-section, as given in Eq. 3.1. In practice, luminosity can be expressed in terms of beam parameters since neither the cross-section nor the number of events per second can be directly manipulated. Eq. 3.2 expresses luminosity in terms of the revolution frequency f, the number of bunches N_b, the number of protons per bunch N, and the x- and y- RMS beam widths σ_x and σ_y. [2] The luminosity per bunch, L/N_b, is relevant for pileup. In 2015 operation, the transverse RMS widths were $\sigma_{x,y} \approx 20\,\mu\text{m}$ and the longitudinal RMS width was $\sigma_z \approx 5.5\,\text{cm}$ [15].

$$L = \frac{1}{\sigma}\frac{dN}{dt} \tag{3.1}$$

$$L = \frac{1}{4\pi}\frac{f N_b N^2}{\sigma_x \sigma_y} \tag{3.2}$$

The number of protons per bunch gradually decreases throughout a run (each of which lasts approximately half a day). Naturally, the number of interactions per bunch crossing $\langle\mu\rangle$ varies proportionally with the number of protons per bunch. This variation produces a spread in $\langle\mu\rangle$, as shown in Fig. 2.4 in the previous chapter.

[1] The LHC can also accelerate lead ions.

[2] The Gaussian width of the beam is defined as $\sigma(z) = \sqrt{\epsilon\beta(z)}$, where z is the position along the beam, ϵ is the beam emittance, and $\beta(z)$ is the *Twiss parameter*. At the interaction point z_0, the Twiss parameter is optimized to be a minimum and is referred to as the $\beta^\star$ of the beam.

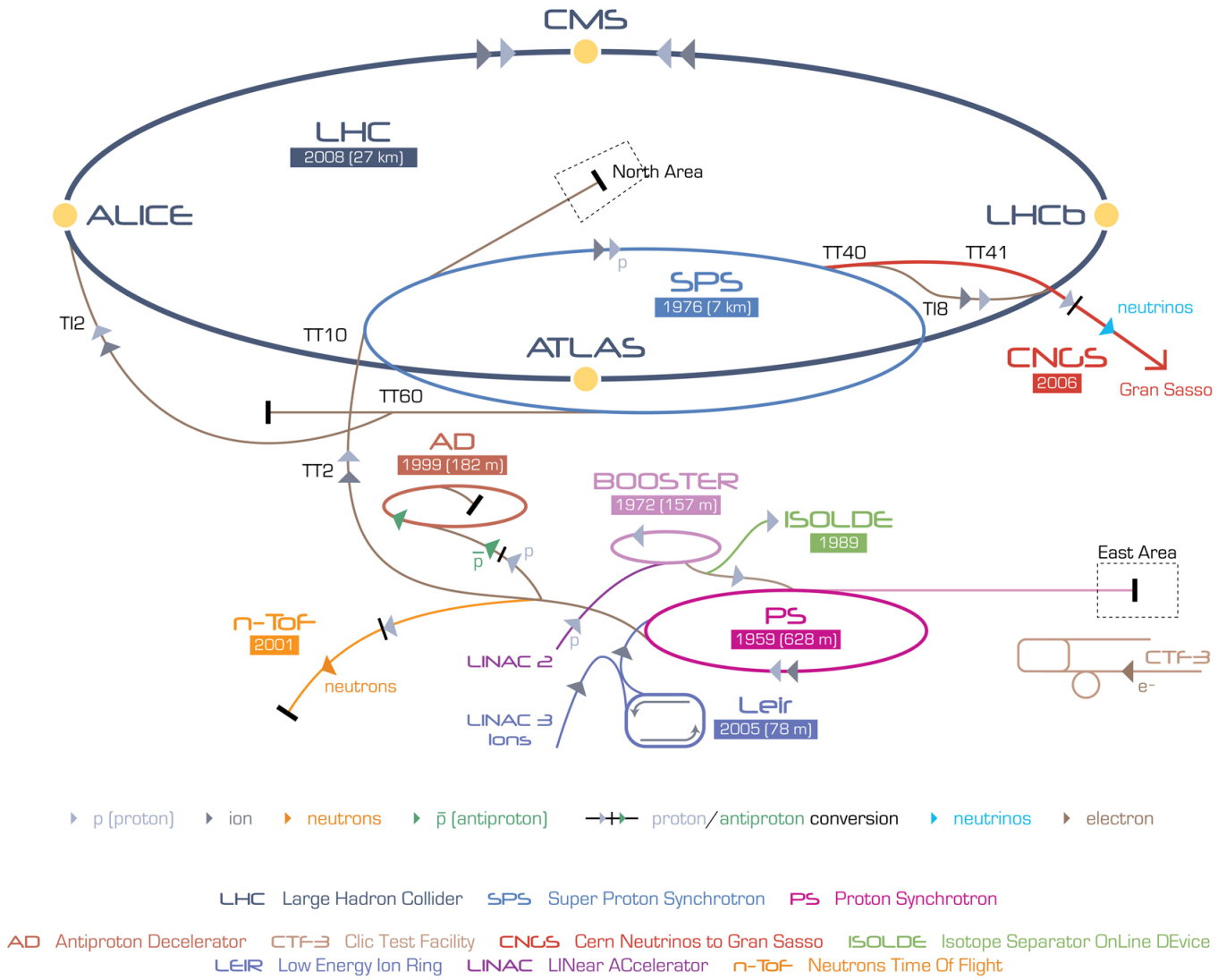

Figure 3.1: Layout of accelerators and detectors at CERN [16].

3.2 ATLAS detector

3.2.1 Overview

The ATLAS detector (shown in Fig. 3.2) was designed to exploit the high energy and luminosity of the LHC in order to explore a wide range of physics ranging from precision measurements of known processes, to discovery of theorized and even unexpected physics. It was designed to meet the following requirements [17]:

- Due to the experimental conditions at the LHC, the detectors require fast, radiation-hard electronics and sensor elements. In addition, high detector granularity is needed to handle the particle fluxes and to reduce the influence of overlapping events.
- Large acceptance in pseudorapidity with almost full azimuthal angle coverage is required.
- Good charged-particle momentum resolution and reconstruction efficiency in the inner tracker are essential. For tagging of tau (τ) leptons and b-jets (jets originating from bottom quarks), vertex detectors close to the interaction region are required to observe secondary vertices.
- Very good electromagnetic calorimetry for electron (e) and photon (γ) identification and measurements, complemented by full-coverage hadronic calorimetry for accurate jet and $E_{\mathrm{T}}^{\mathrm{miss}}$ measurements, are important requirements, as these measurements form the basis of many of the studies mentioned in Ch. 2.2.
- Good muon identification and momentum resolution over a wide range of momenta and the ability to determine unambiguously the charge of high transverse momentum (p_{T}) muons (μ) are fundamental requirements.
- Triggering on the transverse momentum of particles at thresholds that preserve good efficiency for the signals of interest, while operating at computationally sustainable rates by suppressing background.

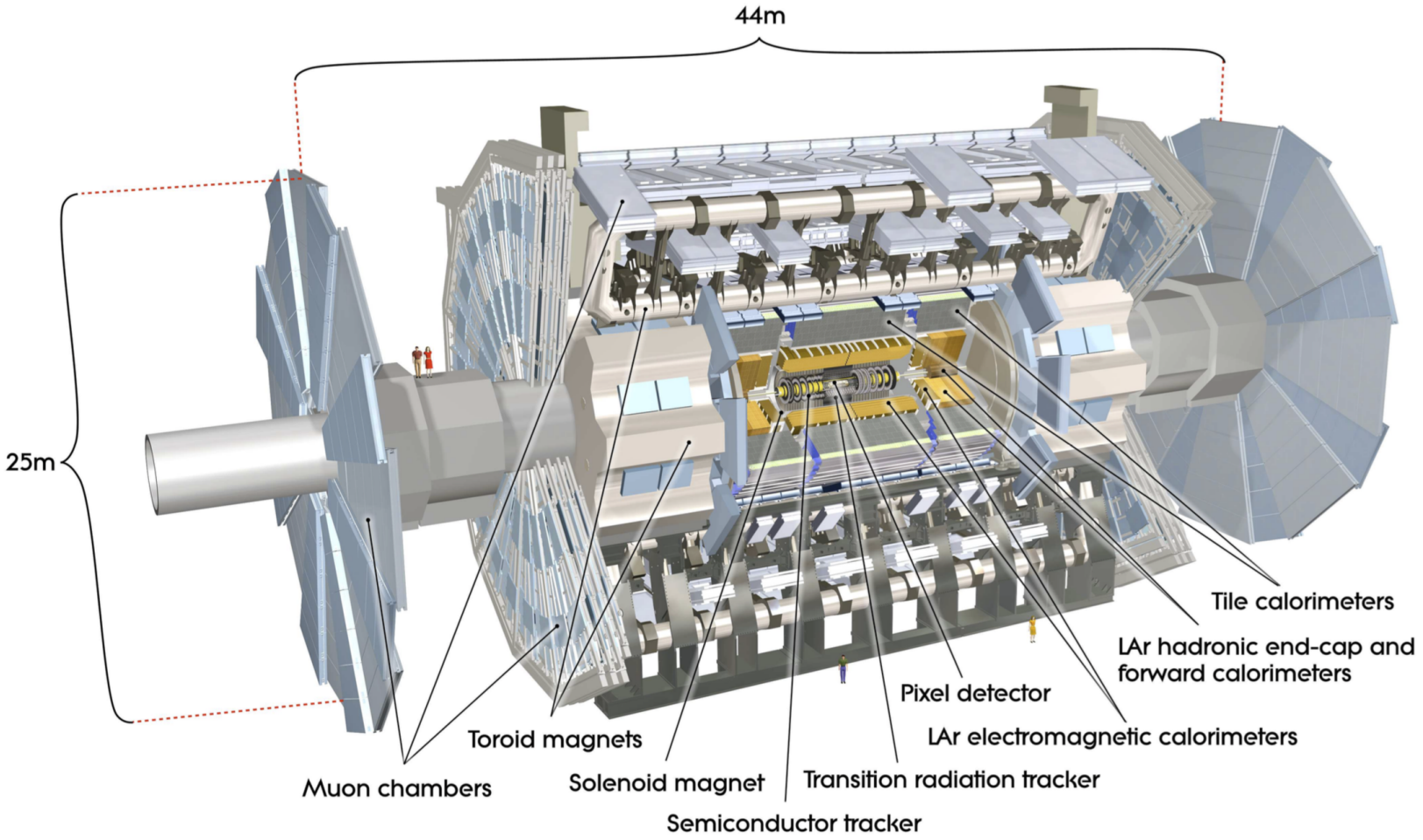

Figure 3.2: Cut-away view of the ATLAS detector [17]. The detector is symmetric with respect to the interaction point and was designed to be as hermetic as possible (i.e. it has close to 4π coverage in solid angle).

The main components of the ATLAS detector are (beginning from the innermost to outermost):

- The **inner detector** (ID), which determines the originating vertices of interactions and identifies charged particles and measures their trajectories via energy deposition in semiconductors and ionization of xenon gas.
- The **electromagnetic and hadronic calorimeters**, which determine the energy of particles that interact electromagnetically (i.e electrons or photons) and hadronically (i.e. jets) by absorbing them and measuring the energy deposited.
- The **muon spectrometer** (MS), identifies muons and measures their trajectories as they pass through and ionize the gas in the MS drift chambers.
- The **magnets**, consisting of a solenoid surrounding the inner detector and three toroid magnets (one barrel toroid and two end-cap toroids). The magnets bend the trajectories of charged particles, thus enabling the inner detector and muon spectrometer to measure their momenta.
- The **trigger and data acquisition system**, which receives and buffers the output of the detector, selects events by performing a fast preliminary reconstruction, and finally writing the event, if selected, to permanent storage.

3.2.2 Inner detector

The ATLAS inner detector (ID) (shown in Fig. 3.3 and 3.4) consists of three subdetectors: the pixel detector, the Semiconductor Tracker (SCT), and the Transition Radiation Tracker (TRT). The entire ID is immersed in a 2 T magnetic field that deflects the trajectories of charged particles. The ID was designed to reconstruct these trajectories (tracks) in the region of the interaction point, within a range of $|\eta| < 2.5$. Interactions happen at an extended distance along the beam pipe due to the spatial spread of the bunches. The ID establishes the origins of the hard scatter and other pp interactions (these are known as *vertices*). The tracking performance requirements and the proximity of the ID to the interaction point and beam pipe impose requirements on the electronics and material thickness: the electronics of the ID must maintain low occupancy amidst high hit rates, have efficient readout and be radiation hard, and the amount of material must be minimized to reduce the number of unwanted photon conversions. As a charged particle passes through the ID, it will

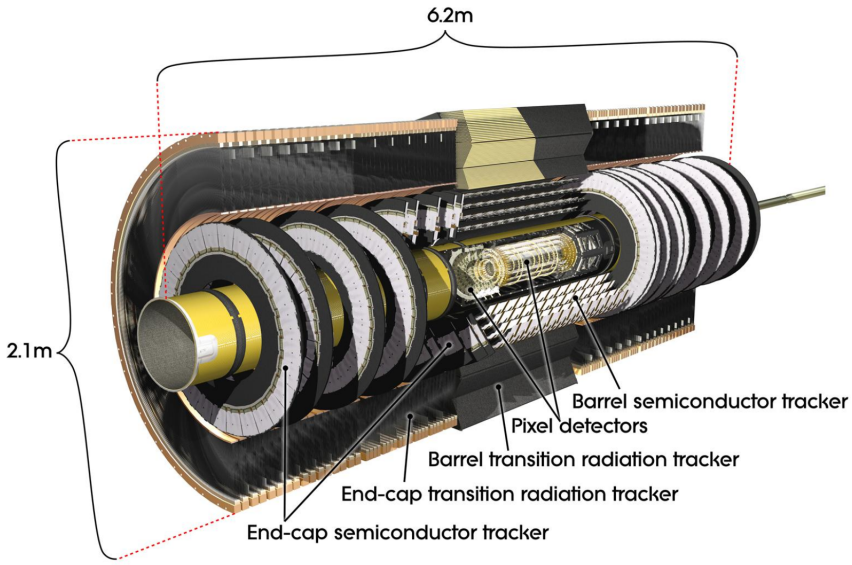

Figure 3.3: Cut-away view of the ATLAS inner detector [19].

register hits in the semiconductors of the pixel detector and SCT, and ionize the gas of the TRT through primary ionization and transition radiation [3].

The pixel detector, the innermost layer of the ID, has four barrel layers and two end-caps with three disks each for a total of 92 million readout channels [20, 21]. The pixel detector has a silicon-covered surface area of approximately $2\,\mathrm{m}^2$. Layer-0 of the pixel detector, the *Insertable B-Layer* (IBL), is new for "Run-2". The reduced distance to the interaction point improves the tracking resolution, which in turn improves the vertexing and b-tagging performance. Furthermore, it affords the pixel detector a margin of robustness against high hit rates by continuing to provide hits even when the readout electronics of the other layers are saturated. The intrinsic measurement accuracy of each sensor is $10\,\mu\mathrm{m}$ in $R-\phi$ and $115\,\mu\mathrm{m}$ in z (for the barrel layers) or R (for the end-caps) [17].

The Semiconductor Tracker (SCT), the middle layer of the ID, has four barrel layers and two end-caps with nine disks. It has a silicon-covered surface area of approximately $60\,\mathrm{m}^2$. It has less granularity than the pixel detector (6.3 million readout channels) and consequently has less accuracy [22]. The intrinsic measurement

[3]Transition radiation consists of photons that are produced when charged particles pass through boundaries, such as the straw tubes of the TRT. The energy of the photons produced is directly proportional to the energy of the particle and inversely proportional to the mass of the particle. Consequently, the energy associated with an electron is significantly greater (8 keV to 10 keV) than the energy associated with a minimally-ionizing particle such as a pion (2 keV) [18]. The main goal of the TRT is to distinguish electrons from other charged particles via this ionization mechanism.

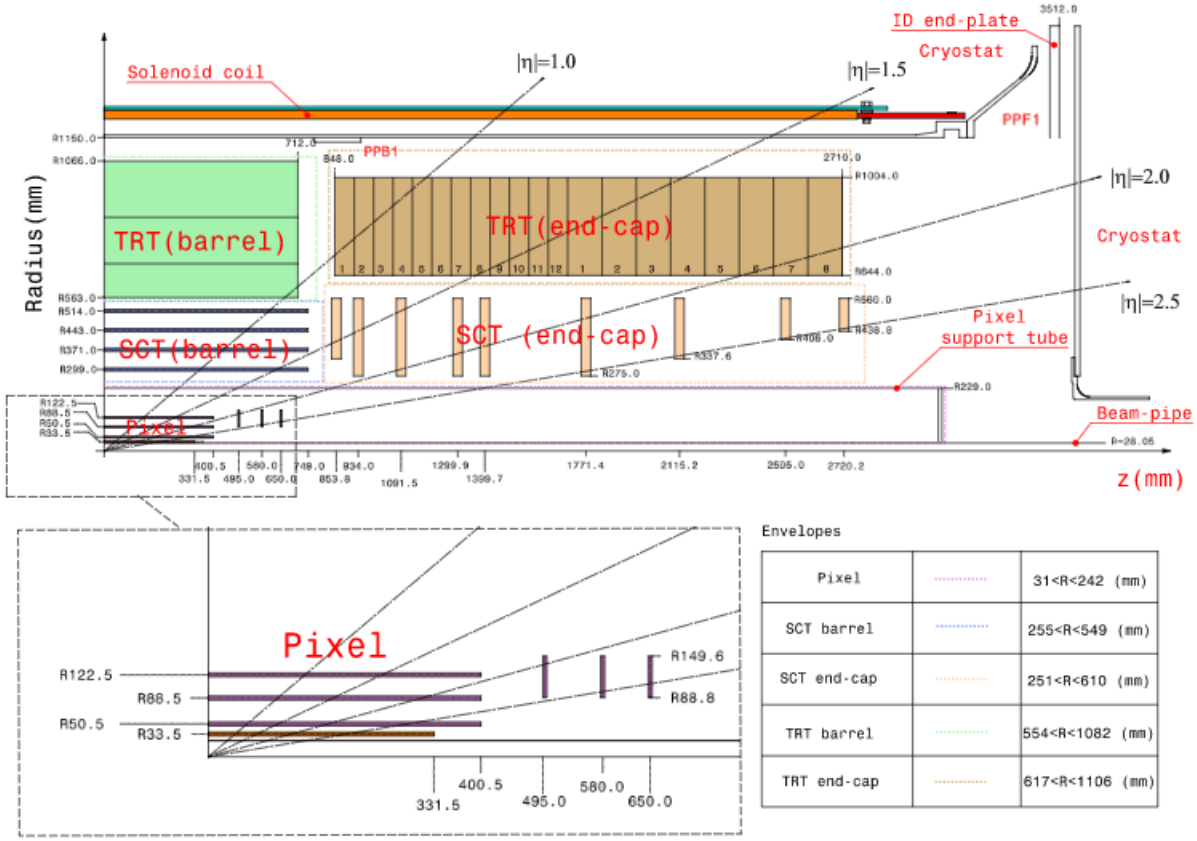

Figure 3.4: Positions and thicknesses of the inner detector components in r (radial distance in the $x-y$ plane) and z (distance along the beam pipe), measured from the centre of the detector [17].

accuracy of each sensor is 17 µm in $R-\phi$, and 580 µm in z (for the barrel layers) or R (for the end-caps) [17].

The Transition Radiation Tracker (TRT), the outermost layer of the ID, is a drift tube system consisting of approximately 350, 000 drift tubes (also referred to as straw tubes) filled with a xenon-based gas. The structure of each drift tube acts as a cathode while the tungsten wire strung along the centre of each tube acts as an anode. When a charged particle passes through, it ionizes the gas and produces ionization charges (electrons and ions). The charges are accelerated by the electric field towards the anode wire and produce further ionization. This additional ionization is commonly referred to as an *ionization cascade*. The charges are then collected on the anode wire, which registers a signal that is proportional to the amount of ionization. The amount of ionization is then proportional to the energy of the charged particle. In addition to the charges of the primary ionization and subsequent ionization cascade,

additional charges are produced by the absorption of *transition radiation* by the gas. Inhomogenous material between straws – fibres and films that create abrupt changes in refractive index – induce transition radiation from charged particles as they pass through. When produced by a highly-relativistic particle, the radiation is in the X-ray range and creates a much larger signal than ionization [23]. The production of transition radiation in the X-ray range is dependent on how relativistically the particle is moving ($\gamma = \gamma(v)$), and by relation, its momentum ($p = \gamma m_o v$). Consequently, it is possible to distinguish electrons from other charged particles by the amount of transition radiation.

3.2.3 Calorimeter

The ATLAS calorimeter comprises of electromagnetic and hadronic calorimeters that cover an overall range of $|\eta| < 4.9$ [17]. It is of a sampling design; each calorimeter consists of passive, absorbing material and an active, measurement medium. When a particle is absorbed, it generates a cascade of secondary particles (a *shower*) that ionizes the active medium. In the electromagnetic calorimeters, the hadronic end-cap calorimeters, and the forward calorimeters, particles are absorbed with plates and the ionization of the liquid argon (LAr) is measured by charge collection on electrodes. LAr was chosen as the active medium because of its linear response and radiation hardness. In the tile calorimeter, particles are absorbed by steel plates and ultraviolet light from the ionization of scintillating polystyrene tiles is collected by photomultiplier tubes. The ATLAS calorimeter is of a non-compensating design: it possesses a greater response to electromagnetic showers than to hadronic showers due to invisible and escaped energy in hadronic interactions that is not immediately compensated for. It is crucial that this difference in response is properly accounted for through calibration (refer to Ch. 3.2.3).

The specifications of the calorimeters are shown in Table. 3.5.

The LAr electromagnetic calorimeter consists of a barrel calorimeter covering up to $|\eta| < 1.475$ and two end-cap calorimeters (EMEC) covering up to $|\eta| < 3.2$. Its high granularity enables it to precisely measure electrons and photons in conjunction with the ID. The absorbing media (lead plates) and active media (LAr) are organized in an accordion geometry (Fig. 3.7 and 3.6). This geometry provides full coverage in ϕ without any cracks and provides enough depth – at least 22 radiation lengths in the barrel and at least 24 radiation lengths in the end-caps – to contain most showers.

	Barrel		End-cap	
EM calorimeter				
Number of layers and $\|\eta\|$ coverage				
Presampler	1	$\|\eta\| < 1.52$	1	$1.5 < \|\eta\| < 1.8$
Calorimeter	3	$\|\eta\| < 1.35$	2	$1.375 < \|\eta\| < 1.5$
	2	$1.35 < \|\eta\| < 1.475$	3	$1.5 < \|\eta\| < 2.5$
			2	$2.5 < \|\eta\| < 3.2$
Granularity $\Delta\eta \times \Delta\phi$ versus $\|\eta\|$				
Presampler	0.025×0.1	$\|\eta\| < 1.52$	0.025×0.1	$1.5 < \|\eta\| < 1.8$
Calorimeter 1st layer	$0.025/8 \times 0.1$	$\|\eta\| < 1.40$	0.050×0.1	$1.375 < \|\eta\| < 1.425$
	0.025×0.025	$1.40 < \|\eta\| < 1.475$	0.025×0.1	$1.425 < \|\eta\| < 1.5$
			$0.025/8 \times 0.1$	$1.5 < \|\eta\| < 1.8$
			$0.025/6 \times 0.1$	$1.8 < \|\eta\| < 2.0$
			$0.025/4 \times 0.1$	$2.0 < \|\eta\| < 2.4$
			0.025×0.1	$2.4 < \|\eta\| < 2.5$
			0.1×0.1	$2.5 < \|\eta\| < 3.2$
Calorimeter 2nd layer	0.025×0.025	$\|\eta\| < 1.40$	0.050×0.025	$1.375 < \|\eta\| < 1.425$
	0.075×0.025	$1.40 < \|\eta\| < 1.475$	0.025×0.025	$1.425 < \|\eta\| < 2.5$
			0.1×0.1	$2.5 < \|\eta\| < 3.2$
Calorimeter 3rd layer	0.050×0.025	$\|\eta\| < 1.35$	0.050×0.025	$1.5 < \|\eta\| < 2.5$
Number of readout channels				
Presampler	7808		1536 (both sides)	
Calorimeter	101760		62208 (both sides)	
LAr hadronic end-cap				
$\|\eta\|$ coverage			$1.5 < \|\eta\| < 3.2$	
Number of layers			4	
Granularity $\Delta\eta \times \Delta\phi$			0.1×0.1	$1.5 < \|\eta\| < 2.5$
			0.2×0.2	$2.5 < \|\eta\| < 3.2$
Readout channels			5632 (both sides)	
LAr forward calorimeter				
$\|\eta\|$ coverage			$3.1 < \|\eta\| < 4.9$	
Number of layers			3	
Granularity $\Delta x \times \Delta y$ (cm)			FCal1: 3.0×2.6	$3.15 < \|\eta\| < 4.30$
			FCal1: $\sim$ four times finer	$3.10 < \|\eta\| < 3.15$,
				$4.30 < \|\eta\| < 4.83$
			FCal2: 3.3×4.2	$3.24 < \|\eta\| < 4.50$
			FCal2: $\sim$ four times finer	$3.20 < \|\eta\| < 3.24$,
				$4.50 < \|\eta\| < 4.81$
			FCal3: 5.4×4.7	$3.32 < \|\eta\| < 4.60$
			FCal3: $\sim$ four times finer	$3.29 < \|\eta\| < 3.32$,
				$4.60 < \|\eta\| < 4.75$
Readout channels			3524 (both sides)	
Scintillator tile calorimeter				
	Barrel		Extended barrel	
$\|\eta\|$ coverage	$\|\eta\| < 1.0$		$0.8 < \|\eta\| < 1.7$	
Number of layers	3		3	
Granularity $\Delta\eta \times \Delta\phi$	0.1×0.1		0.1×0.1	
Last layer	0.2×0.1		0.2×0.1	
Readout channels	5760		4092 (both sides)	

Figure 3.5: Specifications of the ATLAS calorimeter [17]. Note the increased granularity in the EM calorimeter, especially in region closest to the interaction point. The calorimeter has a total of $187,652$ cells.

Additional depth to contain hadronic showers is provided by the surrounding hadronic calorimetry. A presampler covering up to $|\eta| < 1.8$ consisting of one layer of LAr accounts for the energy lost in front of the EM calorimeter (i.e. in the innermost region of the detector).

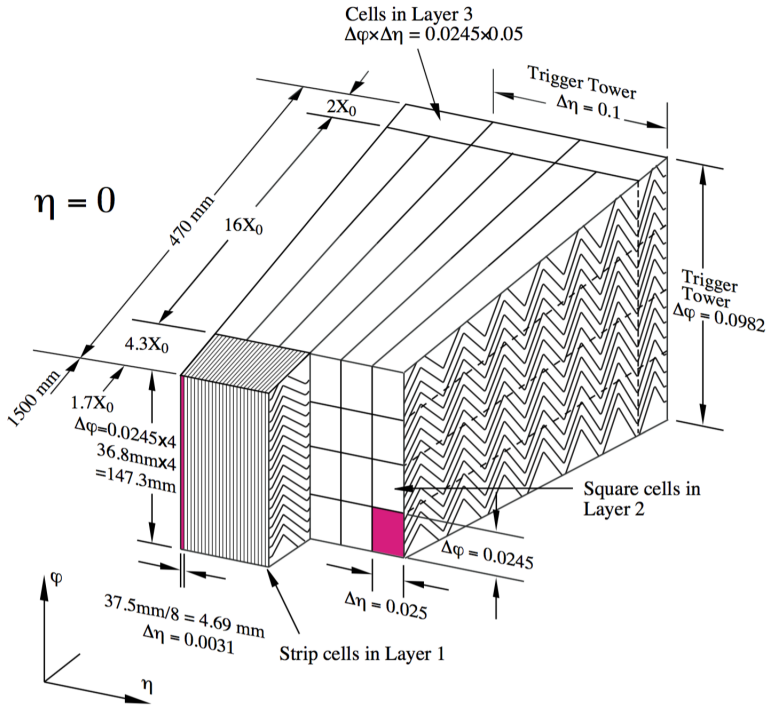

Figure 3.6: Barrel module of the LAr electromagnetic barrel calorimeter [17]. Note how the granularity in ϕ decreases with increasing radial distance. Each half-barrel consists of seven rings with sixteen modules each.

The hadronic calorimeter consists of two LAr end-caps calorimeters (HEC), a tile calorimeter, and two LAr forward calorimeters (FCal). The end-caps, covering $1.5 < |\eta| < 3.24$, use LAr as the active medium due to the increased radiation close to the beam pipe and are interleaved with copper plates. The tile calorimeter, covering up to $|\eta| < 1.7$, uses scintillating tiles and photomultiplier tubes and is interleaved with steel plates (Fig. 3.8). The geometry of the tile calorimeter enables full coverage in ϕ. The forward calorimeters, covering $3.1 < |\eta| < 4.9$, each consist of three modules: an electromagnetic module that is closest to the interaction point, and behind it, two hadronic modules. For the absorbing media, copper is used in the EM module and tungsten is used in the hadronic modules.

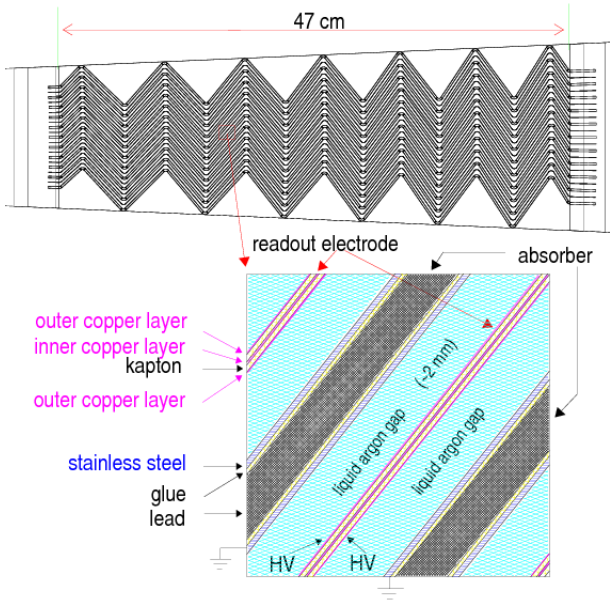

Figure 3.7: Cut-away view of the LAr electromagnetic barrel calorimeter [24]. Note how the absorbing medium and active medium are interleaved.

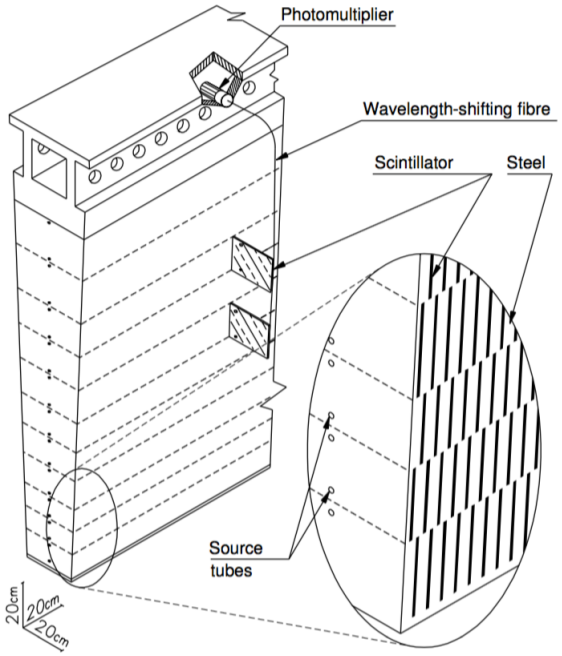

Figure 3.8: Module of the tile hadronic calorimeter [17]. The scintillating tiles and steel plates are oriented radially. Each of the three barrels (one central and two extended) consists of 64 modules.

Calorimeter and jet calibration

A hadronic shower begins with the interaction of a proton and nucleus and generates a variety of particles (mainly pions (π), muons, electrons, neutrinos, photons, and neutrons). The development of a hadronic shower is shown in Fig. 3.9. The release of nuclear binding energy – released in the initial proton-nucleus interaction, as well as in successive interactions – is invisible to the calorimeter. In addition, neutrinos and particles that enter dead zones of the calorimeter (i.e. cracks and non-instrumented service material) escape the coverage of the calorimeter. These sources can account for up to approximately 35% of the shower's energy [25]. The missing energy resulting from invisible and escaped particles must be accounted for through calibration and correction. Furthermore, the division of energy between the decay particles fluctuates greatly, thus detrimentally affecting the resolution in a manner similar to how additional calorimeter energy deposits affects $E_{\mathrm{T}}^{\mathrm{miss}}$ resolution. Additional effects on jets apart from calorimeter-based effects, such as the loss of soft jet constituents due to magnetic bending and pileup contributions to jets, are corrected for at a later stage [4].

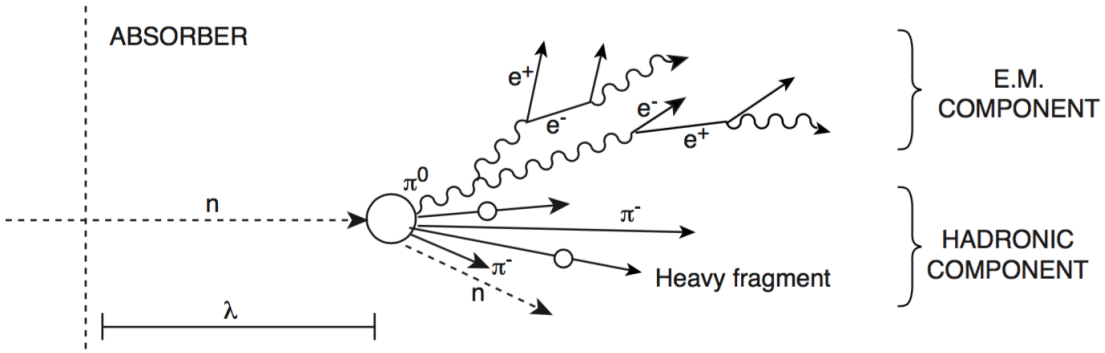

Figure 3.9: Development of electromagnetic and hadronic showers [27].

A number of schemes have been devised for calibrating calorimeter quantities and correcting jets: *EM+JES* (electromagnetic scale plus jet energy scale calibration), *Local Cluster Weighting* (LCW), *Global Cell Weighting* (GCW), and *Global Sequential Calibration* (GS) [28, 29]. In the case of topocluster-based $E_{\mathrm{T}}^{\mathrm{miss}}$, the LCW scheme is

[4]The former is a flavour-dependent effect. Gluon-initiated jets and light quark-initiated jets shower differently. Gluon-initiated jets are wider and have more (but softer) constituent particles while light quark-initiated jets, with their more energetic constituent particles, penetrate deeper. Consequently, the calorimeter responds differently and this difference should be accounted for in calibration [26]. The five variables in global sequential calibration are correlated with how a jet showers.

used. Jets are typically reconstructed from clusters with or without LCW, corrected for pileup, assigned the correct vertex (origin correction), and calibrated for energy scale again with JES, and then finally calibrated for optimal energy resolution with GSC.

In the simplest JES scheme, jet energy correction factors are derived as functions of jet p_{T} and η. The JES scheme can be applied on non-calibrated (i.e. electromagnetic scale) jets (EM+JES) or on LCW-calibrated jets (LCW+JES). In both cases, the response of simulated jets (reconstructed jet p_{T} divided by true jet p_{T}) is considered in bins of $p_{\mathrm{T}} - \eta$. The response is then inverted to give a correction factor that is a function of p_{T} and η. The full-fledged JES scheme performs pileup correction derived from minimum bias and a vertex correction before calibrating for lower hadronic response.

In the Local Cluster Weighting (LCW) scheme, cluster calibration weights derived from simulations of charged and neutral pion interactions are used to calibrate the clusters individually before they are fed into the $E_{\mathrm{T}}^{\mathrm{miss}}$ and jet reconstruction algorithms. The hadronic calibration weights are functions of location and four cluster shape properties (cluster energy density, depth, isolation, and how its energy is divided between calorimeter layers). Additional weights account for out-of-cluster energy and energy lost in cracks. LCW is also referred to as Local Hadron Calibration.

The Global Cell Weighting (GCW) and Global Sequential Calibration (GS) schemes are described in Appendix A.

Calorimeter topological clustering

The multitude of backgrounds – in-time and out-of-time pileup, MPI, and calorimeter noise – make it difficult to disentangle the calorimeter signals arising from the products of the hard scatter. The goal of topological clustering is to identify calorimeter cells with physically significant energy deposits and group them into *topoclusters*. Each topocluster is intended to represent a significant fraction of the calorimeter's response to a particle. The clusters are topological in the sense that the clustering algorithm builds clusters by selecting seed cells and then successively collects neighbouring cells if their signal meets or exceeds pre-defined thresholds, without a fixed window.

The main variable that is used to judge whether a cell should be collected into a

cluster or not is the cell signal significance, $\zeta_{\text{cell}}^{\text{EM}}$:

$$\zeta_{\text{cell}}^{\text{EM}} = \frac{E_{\text{cell}}^{\text{EM}}}{\sigma_{\text{noise,cell}}^{\text{EM}}} \tag{3.3}$$

$\zeta_{\text{cell}}^{\text{EM}}$ is a function of the cell's energy at the electromagnetic scale and of the average expected noise in the cell (determined in previous operation). The criteria for a cell to be selected as a cluster seed, as a neighbour to be collected into a cluster, or neither are:

$$|\zeta_{\text{cell}}^{\text{EM}}| > S \tag{3.4a}$$

$$|\zeta_{\text{cell}}^{\text{EM}}| > N \tag{3.4b}$$

$$|\zeta_{\text{cell}}^{\text{EM}}| > P \tag{3.4c}$$

where $S = 4$, $N = 2$, $P = 0$, typically.

The algorithm can be summarized as follows:

1. The algorithm begins by forming *proto-clusters* by selecting seed cells according to Eq. 3.4a.

2. If a cell neighbouring a seed cell satisfies Eq. 3.4b, it is collected into the proto-cluster.

3. The proto-cluster grows by collecting neighbouring cells that satisfy Eq. 3.4b.

4. If a neighbouring cell satisfies Eq. 3.4c but not Eq. 3.4b, the cell is included into the proto-cluster and the clustering stops. These cells form the perimeter of the cluster.

By considering the absolute value of the cell signal significance, negative cell signals are permitted to be cluster constituents. These signals originate primarily from pulses over 100 ns before and after the current bunch crossing (i.e. distant out-of-time pileup) and to a lesser extent, from electronic noise. Such distant signals are often significant enough to create clusters of negative total energy and vice versa for close out-of-time pileup (i.e. pulses under 100 ns before and after the current bunch crossing but not during the same bunch crossing) and electronic noise. Consequently, the net effect of including clusters containing cells with negative signals is a global cancellation of

the effects of pileup [5] and electronic noise. Observables where such a cancellation is appropriate – such as $E_{\mathrm{T}}^{\mathrm{miss}}$ – include clusters with negative total energy while particle-level observables such as jets only make use of clusters with positive total energy.

The formation of clusters is visualized in Fig. 3.10. The merging of proto-clusters and further details of the algorithm are given in [14].

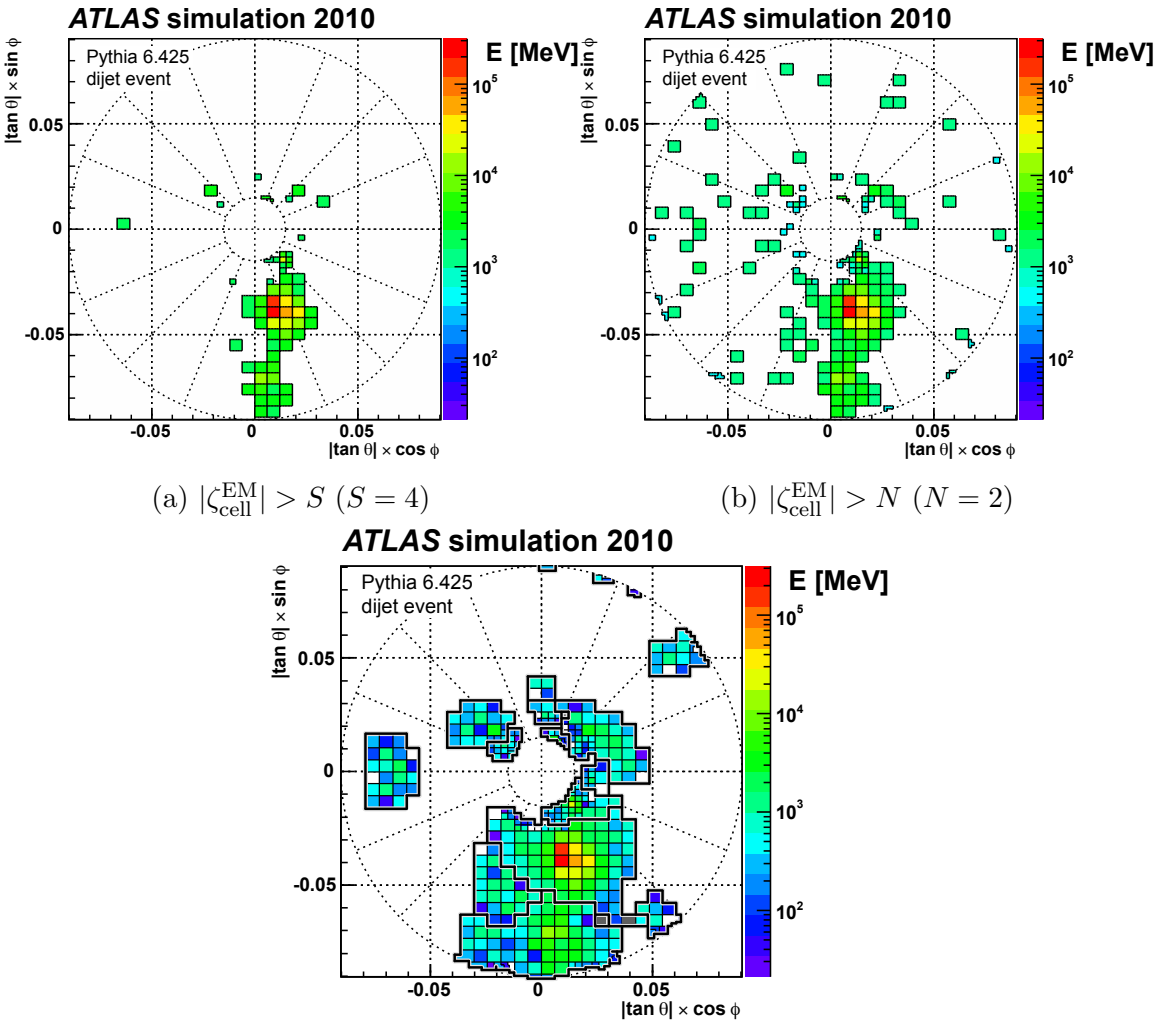

(a) $|\zeta_{\mathrm{cell}}^{\mathrm{EM}}| > S$ $(S = 4)$

(b) $|\zeta_{\mathrm{cell}}^{\mathrm{EM}}| > N$ $(N = 2)$

(c) All clustered cells (cluster boundaries in black)

Figure 3.10: Visualization of topocluster formation in the forward calorimeter [14]. The grid is dimensionless and each square represents a cell. Cells that are black have negative energy.

[5] Signal contributions from in-time pileup are also partially cancelled.

3.2.4 Muon spectrometer

The muon spectrometer (MS) is the outermost sub-detector of the ATLAS detector. It was designed to measure muons with momenta ranging from 3 GeV to 3 TeV within a range of $|\eta| < 2.7$. The overall performance goal was to have a stand-alone p_{T} resolution (i.e. without the assistance of other detectors) of $\lesssim 10\%$ for muon tracks of 1 TeV in p_{T} [17, 30]. The MS operates within a magnetic field produced by one barrel toroid covering $|\eta| < 1.4$ and two end-cap toroids covering $1.6 < |\eta| < 2.7$ (with the transition region covered by a combination of the fields produced by the barrel and end-cap). The magnetically-deflected muon trajectories are measured by a combination of drift chambers, as shown in Fig. 3.11.

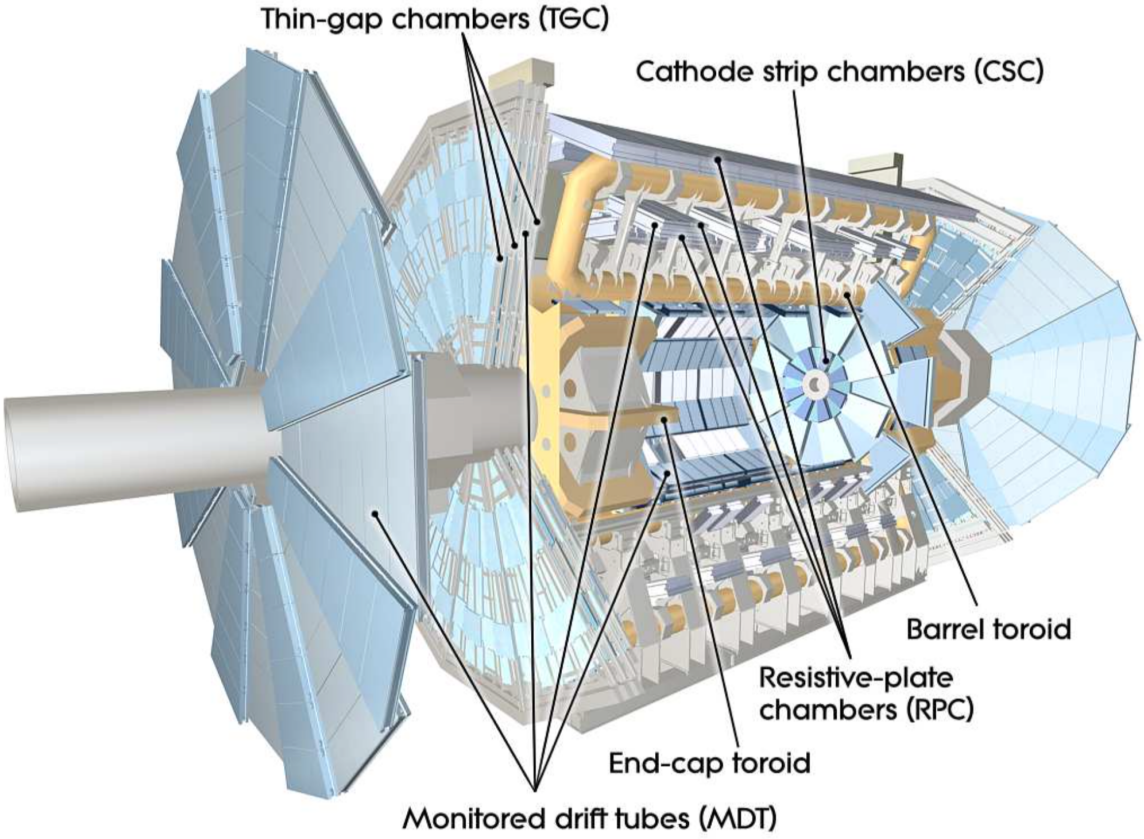

Figure 3.11: Cut-away view of the ATLAS detector with components of the muon spectrometer labelled [17].

The method used to measure muons in the MS is similar to the method used to measure charged particles in the TRT. The structure of each chamber (tube) acts as a cathode while the wire strung along the centre of each chamber (tube) acts as an

anode. The gas mixture used consists of 97% argon and 3% carbon dioxide.

In the barrel region, tracking is provided by monitored drift tubes (MDTs) with a resolution of 35 µm in z and triggering is provided by resistive plate chambers (RPCs) with a resolution of 10 mm in z and ϕ within $|\eta| < 1.05$. In the end-cap region, tracking is also provided by MDTs, up to $|\eta| < 2$, and triggering is provided by thin gap chambers (TGCs) with a resolution of 2 to 6 mm in R and 3 to 7 mm in ϕ within $|\eta| < 2.4$. In the forward region ($2 < |\eta| < 2.7$), where the hit rate and muon track density are higher, cathode strip chambers (CSCs) with a resolution of 40 µm in R and 5 mm in ϕ are used.

A challenge in muon triggering is maintaining resolution in p_{T} over η. Muon momentum, on average, increases with η. In addition, hit rates from background are greater in the forward region and the TGCs are outside of the magnetic field. These challenges necessitate increased granularity in the end-cap region, provided by the TGCs.

Reconstruction of muons can be done with the MS alone or in combination with the ID and/or calorimeter by extrapolation and association of tracks between components.

3.2.5 Trigger and data acquisition system

The ATLAS detector features a multi-level trigger and data acquisition system (TDAQ) to reduce the raw event rate provided by the LHC (40 MHz) to a manageable 1 kHz [17]. The system receives the output of the detectors and within 2.5 µs, identifies object candidates and forms a decision on whether or not to accept the event for further processing. This decision, made by the *Level-1* (L1) trigger using coarse detector output, reduces the rate from 40 MHz to 100 kHz. If the event is accepted by the L1 trigger, the full detector output and regions-of-interest (ROIs) identified by the L1 trigger are passed onto the *High-Level Trigger* (HLT). The HLT, within 0.2 s, makes a final decision using more complex algorithms and access to the full granularity of the detector. If the event is accepted by the HLT, the full detector output, along with any objects reconstructed by the trigger, is written to permanent storage for offline reconstruction and analysis. The layout of the ATLAS TDAQ system is shown in Fig. 3.12.

Trigger configuration

The L1 and HLT triggers are configured by their respective *trigger menus*. These trigger menus are the result of balancing competing demands for bandwidth from different physics signatures and ultimate determine what physics processes ATLAS will be able to record for further analyses. The trigger menu used in 2015 operation for runs at peak luminosity is given in Appendix A.

The L1 trigger menu is organized in *trigger items*. Each trigger item defines the objects to be triggered on, along with the object thresholds and multiplicities that must be met in order for the L1 trigger to form an affirmative decision. For example, the trigger item `L1_2MU4` translates to a requirement of at least two muon candidates with $p_{\mathrm{T}} \geq 4\,\mathrm{GeV}$ identified at L1.

The HLT trigger menu is organized in *trigger chains*. Each trigger chain defines the initiating L1 trigger item, the HLT feature extraction algorithms (FEXes) that should be run, the hypothesis algorithms (hypos) against which the result should be compared, and any pre-scale on the rate if required [6]. If the hypo fails the L1 result, the chain is terminated and the HLT algorithm is not executed. The trigger menu software parses the trigger chain to identify the FEXes and hypos required and configures the HLT steering software and algorithms such that all trigger chains will be executed. For example, the trigger chain `['j400_a10_lcw_L1J100', 'L1_J100'...]` translates to a requirement of at least one $\geq 100\,\mathrm{GeV}$ jet candidate identified at L1 and a requirement of at least one $\geq 400\,\mathrm{GeV}$ jet candidate identified with the anti-k_t algorithm ($R = 1.0$) from LCW-calibrated topological clusters. The FEX is the anti-k_t algorithm from the FastJet jet finding package configured to find jets within a cone of $R = 1.0$. The hypo is a requirement of at least one $\geq 400\,\mathrm{GeV}$ jet.

Data flow

The on-detector Front End readout electronics outputs detector data to the L1 trigger and buffers the data in pipeline memories while waiting for a decision from the L1 trigger (the L1A signal). If the event is accepted by the L1 trigger, the data is forwarded from the Front End readout electronics to the ReadOut Drivers. The ReadOut Drivers perform compression, aggregation, and other data manipulation tasks. The raw nature and rate of the data flowing into L1 necessitates custom

[6] A prescale reduces the trigger rate by allowing only a pre-defined fraction of the trigger item to pass.

hardware such as FPGAs and ASICs. The data processed by the ReadOut Drivers is then sent to the ReadOut System. The ReadOut System buffers the data on commodity-level computers while waiting for a decision from the HLT, and can feed detector data to the HLT through the Data Collection Network. If the event is accepted by the HLT, the data is forwarded from the ReadOut System to the SubFarm Output, which writes the data to permanent storage.

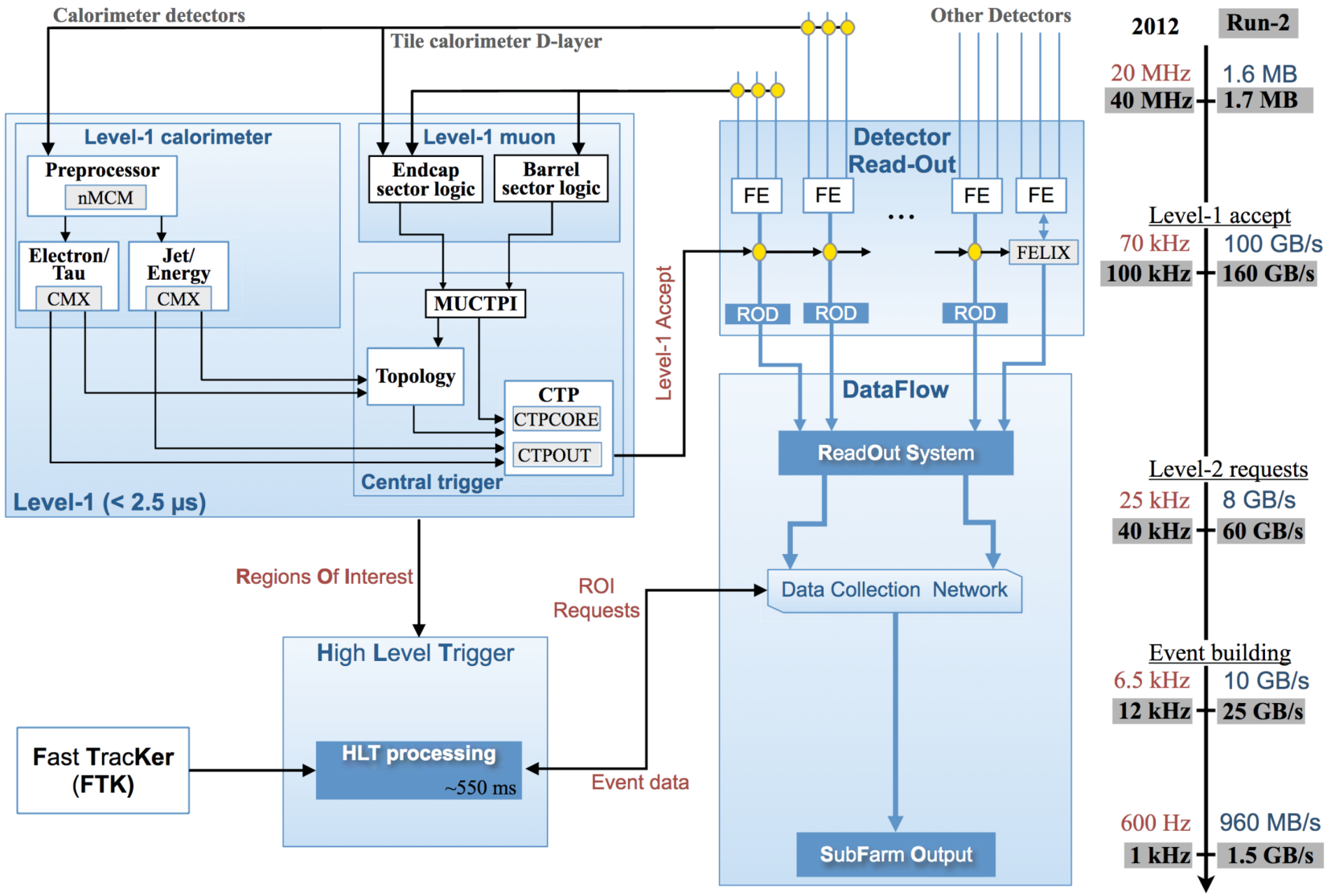

Figure 3.12: Layout of the ATLAS TDAQ system [31]. Shown are the rates at which (i) L1 accepts events, (ii) L2 algorithms retrieve granular data in L1-seeded ROIs, (iii) events are built for the Event Filter algorithms.

Level-1 trigger

The L1 trigger identifies object candidates in the calorimeter and muon spectrometer, calculates energy in the calorimeter, and produces a decision on whether or not to pass the event onto the HLT. Muons, electrons, photons, jets, and taus can be identified and $E_{\mathrm{T}}^{\mathrm{miss}}$ and ΣE_{T} can be computed. The L1 muon trigger utilizes the full granularity of the triggering components of the MS – the RPCs and the TGCs – while the L1 calorimeter trigger (L1Calo) utilizes approximately 7000 analog *trigger towers* of reduced granularity spanning the entire volume of the calorimeter.

An overview of the L1 trigger is given in the following sections. More detail is given in Appendix A.

Level-1 calorimeter trigger

The Level-1 calorimeter trigger (L1Calo) receives coarse granularity data from the calorimeters, performs digitization, noise suppression and pileup subtraction, and identifies object candidates and calculates energy quantities. The trigger consists of pre-processors which receive input directly from the calorimeter front-end electronics and processors dedicated to object identification and energy calculation.

The front-end electronics of the LAr-based calorimeters consist of front-end boards and tower builders/drivers, as shown in Fig. A.1 (in the appendix). The front-end boards amplify, shape, and perform analog-to-digital conversion of the calorimeter channels in full granularity and forward the output to the ReadOut drivers for buffering. The tower builders sum the analog output of the calorimeter channel in towers of $\Delta\eta \times \Delta\phi = 0.1 \times 0.1$ up to $|\eta| < 2.4$, as shown in Fig. 3.6. At larger η (i.e. in parts of the end-cap and forward calorimeters), the towers are larger. Each channel corresponds to a calorimeter cell. The number of calorimeter cells that make up a trigger tower ranges from a few in the end-cap calorimeters to up to sixty in the LAr barrel electromagnetic calorimeter. In the tile calorimeter, the towers are built in a similar fashion by analog summation of five neighbouring photomultiplier tube signals.

The trigger towers are pre-processed by the new Multi-Chip Modules [32]. The new Multi-Chip Modules (i) perform analog-to-digital conversion of the trigger towers, (ii) apply dynamic pedestal subtraction and autocorrelation filters, (iii) perform bunch crossing identification, and (iv) both electromagnetic and hadronic scale calibration with look-up tables. The trigger towers calibrated at electromagnetic scale

are forwarded to the Cluster Processor and the trigger towers calibrated at hadronic scale are first summed into *jet elements* of $\Delta\eta \times \Delta\phi = 0.2 \times 0.2$ before being forwarded to the Jet/Energy Processor. More detail on the new Multi-Chip Modules is given in Appendix A.

The Cluster Processor uses a sliding-window algorithm to identify electrons, photons, and taus. The algorithm looks for clusters – consisting of 2×2 trigger towers – in which at least one of the four possible two-tower sums exceeds a pre-defined threshold. A cluster is shown in Fig. 3.13. Additional thresholds are imposed on the towers around it to ensure that the object is isolated.

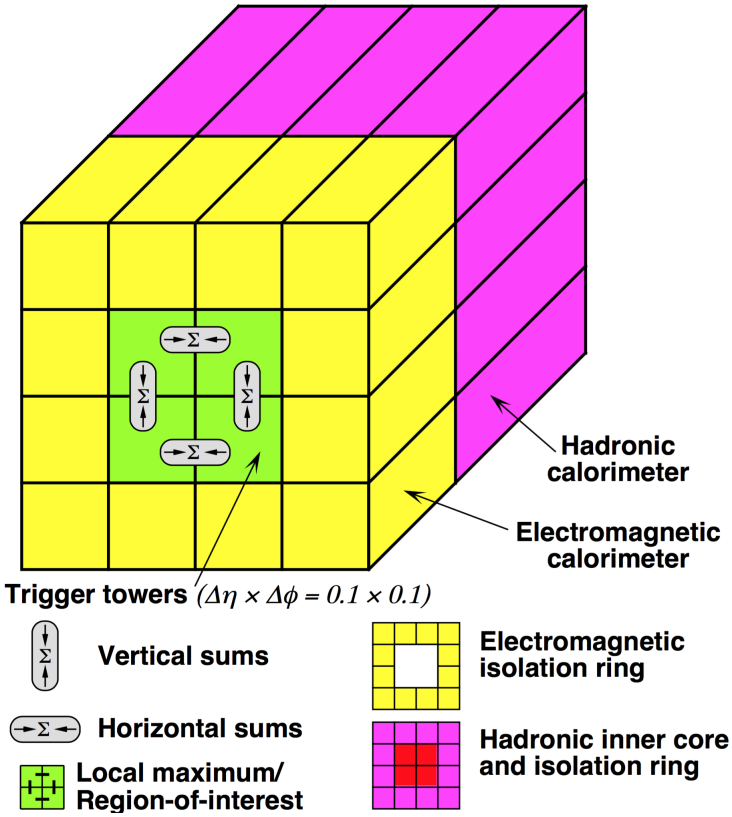

Figure 3.13: Cluster window considered by the L1Calo Cluster Processor [17].

The Jet/Energy Processor works similarly. Jet elements from both the electromagnetic and hadronic calorimeters are combined to form windows consisting of 2×2, 3×3, or 4×4 jet elements. Jet candidates are identified by comparing the ΣE_{T} within each window to pre-defined thresholds. The Jet/Energy Processor also calculates $E_{\mathrm{T}}^{\mathrm{miss}}$, ΣE_{T}, E_x, and E_y and compares $E_{\mathrm{T}}^{\mathrm{miss}}$ and ΣE_{T} to pre-defined thresholds.

The particle candidates identified by the Cluster Processors and the jet candi-

dates and energy quantities identified by the Jet/Energy Processors are forwarded to extended Common Merger Modules as trigger objects. Each trigger object specifies a Region-of-Interest (ROI) containing the object candidate and the E_{T} of the ROI. The trigger objects are finally forwarded to the L1 topological processor (L1Topo) and the L1 Central Trigger Processor (CTP).

Level-1 muon trigger

The L1 muon trigger (L1Muon) operates by requiring spatial coincidence of hits in either the TGCs or RPCs [17]. Each muon p_{T} threshold is assigned a spatial *road width* within which a hit found in one group of TGC/RPC layers can qualify as being in spatial coincidence with a hit in another group of TGC/RPC layers. The higher the threshold, the narrower the road. If spatial coincidence is found, the track candidate is forwarded to the Muon to Central Trigger Processor Interface (MUCTPI). The MUCTPI counts the multiplicity of muon track candidates – taking care to avoid overlaps – and forwards the final multiplicities and ROIs to the L1 CTP.

Level-1 Central Trigger Processor

The L1 CTP receives the object candidates and threshold results from L1Calo, L1Muon, and L1Topo and forms a decision on whether or not the event should be accepted at Level-1. L1Calo and L1Muon can supply a maximum of 320 signals combined (124 signals each) and L1Topo can supply a maximum of 192 signals. Up to 512 trigger items are programmed into look-up tables (LUTs). A trigger item can be a combination of requirements. For example, an item can require a minimum number of a certain object passing a certain threshold and a minimum amount of $E_{\mathrm{T}}^{\mathrm{miss}}$. The trigger input signals are compared with the pre-defined LUTs using logical operations. Further logical operations impose bunch crossing requirements and if required, pre-scales. A veto can be forced at this stage if any of the detectors report dead-time. Finally, a L1A signal is formed by a logical OR between all of the final trigger items. The L1A signal then is sent to the detector FEs, which will forward the buffered data onwards if the L1A signal is affirmative.

Level-1 topological processor

The Level-1 topological processor (L1Topo) calculates geometric and kinematic relationships between objects identified by the various Level-1 triggers. These relation-

ships can be used to improve the discrimination of objects over background by, for example, imposing requirements on object isolation and removal of energy in overlapping objects. Most importantly, however, it can improve the discrimination of signals originating from physics of interest. The signatures of interesting physics processes usually have characteristic *topological* relationships between their products. For instance, the invariant mass of two ROIs (e.g. two muons) can be reconstructed by L1Topo and can be used as a trigger item. Such a trigger item might require the dimuon mass to be within a window around the J/Ψ, B_s, or Υ mass. Other examples include requirements on angular separation between objects (e.g. $\Delta\phi$ between a jet and $E_{\mathrm{T}}^{\mathrm{miss}}$) and requirements on ΣE_{T} of multiple objects (e.g. multiple jets for identification of fat jets). L1Topo enables trigger items to mimic their offline counterparts by triggering on topological relationships between objects.

High-Level Trigger

Upon receiving an affirmative L1A signal from the L1 CTP, the High-Level Trigger (HLT) performs more accurate identification of object candidates by harnessing the full granularity of the detector with more complex algorithms. The rate reduction by the Level-1 trigger affords the HLT a window of time ($\lesssim 550\,\mathrm{ms}$) in which to reconstruct objects and form a decision on whether or not to accept the event. The HLT runs on a farm of commodity-level computers and reduces the trigger rate from 100 kHz – the rate at which events are triggered by Level-1 – to 1 kHz (the rate at which events are written to permanent storage).

In "Run-2", the architecture of the HLT was revamped. Notably, the two pre-existing HLT farms – Level-2 (L2) and Event Filter (EF) – were merged into one farm. However, for most objects, a L2 trigger continues to precede an EF trigger for rate reduction reasons. The L2 trigger for most objects is seeded by the ROIs identified by the L1 trigger and uses reconstruction algorithms that are more complex and slower than those at L1 but are less complex and faster than those at the EF level. With the liberty of additional computational resources, the EF trigger uses reconstruction algorithms that are similar to those used offline. They may lack additional features such as advanced calibration, isolation, overlap removal, and the knowledge of other objects in the event. As described in Ch. 3.2.5, each level consists of at least one feature extraction (FEX) algorithm with a corresponding hypothesis algorithm (hypo).

For high-level triggering on electrons and photons, two trigger levels are used. The L2 trigger receives a list of ROIs from the L1 CTP and retrieves the contents of each ROI from the ROS. The ROIs in this case consist of clusters of 2×2 trigger towers. The position of each cluster is used as the centre for a calorimeter cell-level reconstruction of size $\Delta\eta \times \Delta\phi = 0.4 \times 0.4$. The L2 reconstruction uses the most energetic cell as its seed. Shower variables such as their shape (e.g. width in η, ratio between the highest energy maxima) and energy and the presence of a matching track are used for electron and photon identification. If pre-defined thresholds on the identified candidates are met, the EF trigger performs a more precise reconstruction, with its cluster seed determined by a sliding-window algorithm. The reconstruction is followed by more precise track reconstruction and matching.

For high-level triggering on jets and $E_{\mathrm{T}}^{\mathrm{miss}}$, only one trigger level is used. The high-level $E_{\mathrm{T}}^{\mathrm{miss}}$ trigger is described in the following chapter.

The high-level jet trigger can construct jets from either trigger towers or topological clusters (with or without LCW calibration) and with or without additional calibration (JES) and pileup subtraction. In all cases, the anti-k_t algorithm from the FastJet jet finding package is used [33].

For high-level triggering on muons, two trigger levels are used. The reconstruction of ID tracks is not done at L1 due to computational limits; however, it becomes possible at the HLT. In a manner similar to offline reconstruction, the HLT muon trigger reconstructs tracks in the MS and matches them with tracks reconstructed by the ID HLT.

Chapter 4

High-level $E_{\mathrm{T}}^{\mathrm{miss}}$ trigger algorithms and offline $E_{\mathrm{T}}^{\mathrm{miss}}$ reconstruction

The high-level $E_{\mathrm{T}}^{\mathrm{miss}}$ trigger hosts a variety of FEX algorithms for calculating $E_{\mathrm{T}}^{\mathrm{miss}}$. The algorithms use calorimeter cells, topological clusters, and trigger-level jets as input and can apply pileup subtraction or correction schemes. The $E_{\mathrm{T}}^{\mathrm{miss}}$ calculated by these different algorithms can have different energy scales and can be affected differently by pileup. These attributes are determined by the calibration and pileup resistance of their inputs (respectively) and any additional pileup subtraction/correction applied by the HLT $E_{\mathrm{T}}^{\mathrm{miss}}$ algorithm. Furthermore, these attributes lead to different trigger rates for each algorithm (even when operated at the same threshold). This chapter describes each of the algorithms in detail.

All of the algorithms are calorimeter-based. EF-level muons, identified by the MS, can optionally be included in the final value of $E_{\mathrm{T}}^{\mathrm{miss}}$. This option is available for all HLT FEX algorithms [1].

All of the algorithms were run in parallel during 2015 operation.

4.0.1 From calorimeter cells

The `EFMissingETFromCells` algorithm calculates energy quantities from calorimeter cells. The algorithm divides the calorimeter into twelve samplings: LAr electromagnetic samples 0-3, LAr hadronic samples 0-3, Tile, FCal EM, and FCal hadronic samples 0-1. The algorithm calculates E_x, E_y, E_{T}, ΣE_{T}, and $E_{\mathrm{T}}^{\mathrm{miss}}$ in each sampling,

[1] This option was not enabled during 2015 operation. Consequently, the trigger $E_{\mathrm{T}}^{\mathrm{miss}}$ studied in this thesis is purely calorimeter-based.

with a two-sided noise suppression cut of $|E_{cell}| > 2\sigma$ and $E_{cell} > -5\sigma$ imposed on each cell. The two-sided nature of the noise threshold avoids a bias in ΣE_{T} and is similar to the noise suppression used in calculating the calorimeter-based soft term in offline $E_{\mathrm{T}}^{\mathrm{miss}}$ reconstruction. The algorithm forwards the energy quantities of each sampling into the `TrigMissingET` EDM data structure (event data model) as well as the corresponding calorimeter-wide values.

Unlike the topoclusters used by the topocluster-based $E_{\mathrm{T}}^{\mathrm{miss}}$ algorithm (described in the following section), the calorimeter cells used by this algorithm are at electromagnetic scale. The L1 $E_{\mathrm{T}}^{\mathrm{miss}}$ algorithm uses calorimeter towers that are also at electromagnetic scale.

The most computationally costly operation in this algorithm is the unpacking of the data structure containing the calorimeter cells. This takes approximately 100 ms. The projection and summation of energies has insignificant computational cost.

The advantage of this algorithm is that it is computationally inexpensive since it only performs vectorial summation with no manipulation of the calorimeter cells beforehand. The disadvantages are that (i) the calorimeter cells are not hadronically calibrated and (ii) it has no advanced pileup/noise suppression scheme.

4.0.2 From calorimeter topoclusters

The `EFMissingETFromClusters` algorithm calculates energy quantities from topological clusters. The formation of these clusters is described in Ch. 3.2.3.[2] The clusters can be un-calibrated (i.e. at electromagnetic scale) or can be calibrated with local cluster weights (described in Ch. 3.2.3). The most computationally costly operation is the construction and calibration of the clusters. As is the case with the cell-based algorithm, the projection and summation of energies has insignificant computational cost.

The advantage of this algorithm is that its constituents are hadronically calibrated. Consequently, the $E_{\mathrm{T}}^{\mathrm{miss}}$ calculated by this algorithm will be at hadronic scale (rather than at electromagnetic scale). This brings the trigger $E_{\mathrm{T}}^{\mathrm{miss}}$ closer to the true value (as will be evident in the correlation plots shown later in Ch. 6). In 2015, the thresholds on topocluster $E_{\mathrm{T}}^{\mathrm{miss}}$ (and jet-based $E_{\mathrm{T}}^{\mathrm{miss}}$ as well) were the same as the threshold on cell $E_{\mathrm{T}}^{\mathrm{miss}}$. Since cell $E_{\mathrm{T}}^{\mathrm{miss}}$ is at a lower energy scale (electromagnetic) than topocluster and jet-based $E_{\mathrm{T}}^{\mathrm{miss}}$ (hadronic), the rates of topocluster and jet-based

[2] In 2015, the thresholds used in cluster formation were $|\zeta_{\mathrm{cell}}^{\mathrm{EM}}| > 4, 2, 0$.

$E_{\mathrm{T}}^{\mathrm{miss}}$ will be higher than the rate of cell $E_{\mathrm{T}}^{\mathrm{miss}}$ at equal thresholds.[3] The disadvantage of this algorithm is that the formation of topoclusters is computationally expensive. The pileup subtraction and correction schemes applied onto topoclusters can improve pileup resistance but have additional computational cost.

The `EFMissingETFromClustersPS` and `EFMissingETFromClustersPUC` algorithms use hadronically calibrated topoclusters as input to pileup subtraction/correction schemes.

With pileup subtraction in rings of η

The `EFMissingETFromClustersPS` algorithm divides the calorimeter into rings of η, estimates and applies a pileup subtraction per ring, and re-calculates the overall $E_{\mathrm{T}}^{\mathrm{miss}}$. The pileup contribution is estimated by omitting the most energetic clusters and calculating the energy density. By default, the calorimeter is divided into ten rings of η. The algorithm is as follows:

1. In ring i, the average energy $E_{\mathrm{cl,avg}}$, total energy $\Sigma E_{\mathrm{all},i}$ and standard deviation in energy $\sigma_{E,i}$ are calculated.

2. In the same ring, the total energy is recalculated with energetic clusters $E_{\mathrm{cl}} > E_{\mathrm{cl,avg}} + 2\sigma_{E,i}$ omitted. This quantity, $\Sigma E_{\mathrm{pileup},i}$, is divided by the solid angle of the ring to give the average energy density of the pileup contributions, $\rho_{\mathrm{pileup},i}$.

3. In the same ring, the pileup contribution to each cluster is subtracted from its original energy. The amount subtracted is proportional to the solid angle of the cluster: $\Omega_{\mathrm{cl}} \times \rho_{\mathrm{pileup},i}$.

4. The overall $E_{\mathrm{T}}^{\mathrm{miss}}$ is calculated by a vectorial sum over the corrected clusters.

The pileup subtraction is only applied to clusters whose energy before subtraction is positive, and whose energy after subtraction is still positive. The correction for each ring in η is greater in the forward region, where there is more pileup. This algorithm is computationally inexpensive and can be applied to cells as well.

[3] Event rejection on the basis of pileup could potentially lower the rates of hadronic scale $E_{\mathrm{T}}^{\mathrm{miss}}$ below the rates of electromagnetic scale $E_{\mathrm{T}}^{\mathrm{miss}}$.

With pileup correction derived from χ^2 minimization

The `EFMissingETFromClustersPUC` algorithm suppresses pileup in two stages. The algorithm uses towers of $\Delta\phi \times \Delta\eta \approx 0.7 \times 0.7$ formed from clusters. The first stage rejects the event if no tower has E_{T} above a pre-defined threshold. This stage alone strongly suppresses events with no significant $E_{\mathrm{T}}^{\mathrm{miss}}$. For surviving events, the second stage derives a pileup correction for the towers satisfying the aforementioned threshold by constraining the $E_{\mathrm{T}}^{\mathrm{miss}}$ of the towers failing the threshold and the unknown pileup contributions to the towers above the thresholds, to be zero. The algorithm is as follows:

1. Towers of $\Delta\phi \times \Delta\eta \approx 0.7 \times 0.7$ are formed from clusters. Eight bins in ϕ and fourteen bins in η are used to form a total of 112 towers. The E_x, E_y, and E_{T} are calculated for each tower from their constituent clusters.

2. If the event has no tower with E_{T} above a pre-defined threshold, the algorithm reports zero $E_{\mathrm{T}}^{\mathrm{miss}}$ for the event and consequently, the hypo rejects the event. If the E_{T} requirement is satisfied, the algorithm proceeds to the second stage.

3. The towers with E_{T} above the threshold are masked off and are deemed to be non-pileup contributions. The towers with E_{T} below the threshold are deemed to be pileup contributions and are used in the following step to derive a pileup correction for the masked towers.

4. A χ^2 function $\chi^2 = \chi^2(\mathcal{E}_{T_k}, E_{N_i}, A_o, A_k)$ is minimized to give $\mathcal{E}_{T_k}$, the pileup contributions to the masked towers. E_{N_i} are x- and y-projected energies of the unmasked towers, A_o is the total area of the unmasked towers, and A_k is the area of each masked tower k.

5. Each masked tower is corrected by subtracting from its original energy the corresponding pileup contribution estimated in the previous step.

6. The overall $E_{\mathrm{T}}^{\mathrm{miss}}$ is calculated by a vectorial sum over the corrected masked towers. The unmasked towers are omitted.

The χ^2 function is formulated with a covariance matrix. Two uncertainties contribute to the covariance matrix:

- The dominant uncertainty is the resolution on the energy of the towers, $\sigma_i = r\sqrt{E_{T_i}}$, where r is the scale of the measurement resolution (by default, $r = 0.5\,\mathrm{GeV}^{1/2}$).

- Another uncertainty arises from the discrete nature of pileup. The pileup contribution to each tower can be expressed as $\mathcal{E}_{T_k} = N_{\mathrm{pileup},k}\langle E_{T,\mathrm{pileup}}\rangle$, where $N_{\mathrm{pileup},k}$ is the number of pileup particles in masked tower k and $\langle E_{T,\mathrm{pileup}}\rangle$ is the average transverse energy of pileup particles. $\langle E_{T,\mathrm{pileup}}\rangle$ falls exponentially and has a variance $var(\langle E_{T,\mathrm{pileup}}\rangle) = \langle E_{T,\mathrm{pileup}}\rangle^2/N_{\mathrm{pileup},k}$.

This algorithm is computationally inexpensive. The first stage rejects the majority of events and the minimization involves a nearly diagonal, sparse, and square matrix. This algorithm could also use cells as input [4]

4.0.3 From trigger-level jets

The `EFMissingETFromJets` algorithm calculates energy quantities from jets identified by the HLT jet trigger. This trigger is commonly referred to as the missing hadronic trigger ($H_{\mathrm{T}}^{\mathrm{miss}}$) due to the energy scale of its constituents.

By default, `a4tclcwsubjesFS` jets with $p_{\mathrm{T}} > 35\,\mathrm{GeV}$ are used. These jets have the following specifications:

- Input: all topological clusters from the calorimeter (i.e. *full scan*), calibrated with local cluster weights

- Jet finding algorithm: anti-k_t with cone size $R = 0.4$ (from the FastJet jet finding package)

- Jet energy scale: calibrated with JES (described in Ch. 3.2.3) and pileup subtraction (using the calorimeter-wide topological cluster energy density)

Notably, these jets lack offline features such as origin correction (assigning of the correct originating vertex), global sequential calibration and η-intercalibration (calibration to equalize jet response over η).

[4] The use of cells as input has not been implemented as of writing.

4.0.4 Offline $E_{\mathrm{T}}^{\mathrm{miss}}$ reconstruction

The offline $E_{\mathrm{T}}^{\mathrm{miss}}$ reconstruction uses objects reconstructed offline to construct the best estimate of $E_{\mathrm{T}}^{\mathrm{miss}}$. It serves as the benchmark when studying trigger-level $E_{\mathrm{T}}^{\mathrm{miss}}$. It is defined as:

$$\begin{aligned} E_{\mathrm{T}}^{\mathrm{miss}} &= -\Big[\sum p_T^{\text{hard objects}} + \sum p_T^{\text{soft objects}}\Big] \\ &= -\Big[\underbrace{\sum p_T^{e} + \sum p_T^{\gamma} + \sum p_T^{\tau} + \sum p_T^{\mu} + \sum p_T^{\text{jets}}}_{\text{hard term}} + \underbrace{\sum p_T^{\text{tracks}}}_{\text{soft term}}\Big] \end{aligned} \tag{4.1}$$

where each summation represents a vectorial sum over the transverse momenta of objects passing a pre-defined selection criteria. The objects – provided by their respective offline reconstruction algorithms – are fully calibrated and must pass a pre-defined selection. The criteria on which the object selection is based are analysis-dependent. Examples include p_{T}, object identification quality, requirement of associated tracks, and presence within well-instrumented η ranges of the detector.

The *soft term* is constructed from ID tracks and consists of energy from soft *charged* particles. The tracks are required to originate from the primary vertex; consequently, this term is largely insensitive to pileup but does not include soft *neutral* particles. In comparison to the calorimeter-based soft term used in past ATLAS analyses, this track-based soft term has less contributions from pileup but must be corrected to account, on average, for contributions from soft neutral particles.

Objects that enter into the offline $E_{\mathrm{T}}^{\mathrm{miss}}$ reconstruction may originate from overlapping detector signals and lead to over-counting of energy. To resolve this, each type of object is assigned a priority in the offline $E_{\mathrm{T}}^{\mathrm{miss}}$ reconstruction sequence. The order of the terms in Eq. 4.1 from left to right is the default priority. A lower-priority object is not included in the $E_{\mathrm{T}}^{\mathrm{miss}}$ summation if it originates from detector signals which overlap with those of a higher-priority object. Jets may partially contribute if there is not more than 50% overlap in detector signal with higher-priority objects.

Chapter 5

Data and selection criteria

The data used in this study were collected from pp collisions of the Large Hadron Collider by the ATLAS detector during October and November 2015. The `physics_Main` stream, consisting of events accepted by all triggers, was considered. From this stream, events containing certain physics processes or passing certain triggers were selected. These selections provide different contexts in which to study the performance of the $E_{\mathrm{T}}^{\mathrm{miss}}$ trigger. All studies, except those on simulated $ZH \to \nu\bar{\nu}b\bar{b}$ samples, were based on 2015 collision data.

The `physics_Main` stream and the selections are described in this chapter.

5.1 Data

The approximate trigger rate of the `physics_Main` stream was $\sim 1\,\mathrm{kHz}$. The main trigger menu used is shown in Fig. A.2 in Appendix A. The `physics_Main` stream is typically used for analyses while other streams, such as `express_express`, `calibration_vdM`, and `physics_ZeroBias`, are used for data quality/monitoring, calibration, and studies of trigger rates.

The `physics_ZeroBias` stream, consisting of events accepted by a random trigger on colliding bunches, was used to generate distributions of $E_{\mathrm{T}}^{\mathrm{miss}}$ background. The amount of data in this stream statistically limited the possibility of further background studies.

First, an event selection was imposed to ensure acceptable data quality. In the surviving events, (i) events with processes of interest were identified by imposing object-level criteria and (ii) specific trigger streams were isolated by requiring trigger

acceptance. An overview of the selection criteria used and of the processes and trigger streams is given in the following sections.

5.2 Event selection criteria

An event is considered for analysis only if it passes the following selection:

Good Run List: A list of luminosity blocks ("lumiblocks") during which the detector operated without trouble. Each luminosity block corresponds to 1 minute of data taking. The GRL can be updated if problems with the detector are resolved in offline *data reprocessing* (e.g. the masking of noisy calorimeter cells).

LAr and Tile calorimeter errors: The event is vetoed if any errors (corruption or noise bursts) are reported from the calorimeters.

The total integrated luminosity considered in this study after imposing the above data quality selection was $1435.25\,\mathrm{pb}^{-1}$.

5.3 Physics processes and trigger selections

To perform a complete study of the performance of the $E_{\mathrm{T}}^{\mathrm{miss}}$ trigger, it is necessary to consider:

- processes known *a priori* to produce $E_{\mathrm{T}}^{\mathrm{miss}}$,
- events selected by triggers other than the $E_{\mathrm{T}}^{\mathrm{miss}}$ trigger, and
- the rates of each $E_{\mathrm{T}}^{\mathrm{miss}}$ trigger algorithm, which are dominated by events without genuine $E_{\mathrm{T}}^{\mathrm{miss}}$.

Events with processes producing genuine $E_{\mathrm{T}}^{\mathrm{miss}}$ are used to study how efficiently the $E_{\mathrm{T}}^{\mathrm{miss}}$ trigger accepts such events and how correlated the $E_{\mathrm{T}}^{\mathrm{miss}}$ measured by the trigger is with the $E_{\mathrm{T}}^{\mathrm{miss}}$ reconstructed offline. The performance at different energy scales and of $E_{\mathrm{T}}^{\mathrm{miss}}$ from different objects can be assessed by studying processes with different kinematics and final state particles.

The following physics processes were identified and studied. The selections used to identify the processes are given in Appendix A.

$W \to e\nu$**:** The electron deposits its energy in the electromagnetic calorimeter and the neutrino is invisible to the detector. This process results in genuine $E_{\mathrm{T}}^{\mathrm{miss}}$ at the electromagnetic scale. The purity of $W \to e\nu$ was estimated to be $\sim 92\%$ [34]. The dominant background contribution is from semi-leptonic decays of quarks, mis-identified leptons, and non-prompt leptons (leptons originating not from the hard scatter, but from secondary interactions). This "multi-jet" background was estimated to be $\sim 8\%$ (expressed as the percentage of the total number of such simulated background events passing the signal selection).

$W \to \mu\nu$**:** The muon is detected in the muon spectrometer and similarly, the neutrino is invisible to the detector. If the trigger $E_{\mathrm{T}}^{\mathrm{miss}}$ does not take into account the muon (i.e. if it is calorimeter-only $E_{\mathrm{T}}^{\mathrm{miss}}$) then genuine $E_{\mathrm{T}}^{\mathrm{miss}}$ arises only from the p_{T} of the W boson. The purity of $W \to \mu\nu$ was estimated to be $\sim 96\%$ [34]. The multi-jet background was estimated to be $\sim 4\%$.

$Z \to \mu\mu$**:** The muons are produced "back-to-back". If muons are not taken into consideration, then genuine $E_{\mathrm{T}}^{\mathrm{miss}}$ arises only from the p_{T} of the Z boson. The purity of $Z \to \mu\mu$ was estimated to be $\sim 99\%$ [34]. $t\bar{t}$ production (the dominant background) was estimated to be $\sim 0.5\%$. The multi-jet background was estimated to be $< 0.1\%$.

$t\bar{t} \to X$ The top quark decays almost 100% of the time in the SM to a W boson and a bottom quark [10]. The W boson then decays to a $q\bar{q}$ pair approximately two-thirds of the time or a ℓ and ν approximately one-third of the time. Consequently, about 44.4% of top quark pairs decay completely hadronically (i.e. into six jets), 44.4% of pairs decay semi-leptonically into four jets and a ℓ and ν, and $\sim$ 11% of pairs decay di-leptonically into two jets, two ℓ, and two ν. Due to the high degree of hadronic activity in their decays, $t\bar{t}$ can be used to study $E_{\mathrm{T}}^{\mathrm{miss}}$ produced at the hadronic scale. The purity of $t\bar{t}$ was estimated to be $\sim 96\%$ [35]. The dominant background contribution is from Wt production.

In addition, a sample of Monte Carlo simulated $ZH \to \nu\bar{\nu}b\bar{b}$ events was studied. This sample was made by generating the $ZH \to \nu\bar{\nu}b\bar{b}$ process with pileup interactions at the event level with the `PYTHIA` event generator and then simulating the detector response with the `GEANT` simulator. The production cross-section of $ZH \to \nu\bar{\nu}b\bar{b}$ is dwarfed by the production cross-sections of soft QCD processes that also produce two b-jets and $E_{\mathrm{T}}^{\mathrm{miss}}$. This background, which produces fake $E_{\mathrm{T}}^{\mathrm{miss}}$, makes it impossible

to solely select $ZH \to \nu\bar{\nu}b\bar{b}$ events in data. This process produces genuine $E_{\mathrm{T}}^{\mathrm{miss}}$ at the hadronic scale and can only be selected on the basis of $E_{\mathrm{T}}^{\mathrm{miss}}$ and jets. Unlike the above processes, $ZH \to \nu\bar{\nu}b\bar{b}$ cannot be identified by a lepton trigger as it simply does not possess a charged lepton; its signature is purely $E_{\mathrm{T}}^{\mathrm{miss}}$ and jets. Therefore, $ZH \to \nu\bar{\nu}b\bar{b}$ is an excellent use case for $E_{\mathrm{T}}^{\mathrm{miss}}$ trigger performance. The average number of interactions per bunch crossing in this sample was $\langle\mu\rangle = 21$.

The HLT muon and jet triggers do not select events on the basis of $E_{\mathrm{T}}^{\mathrm{miss}}$ and offer two different contexts in which to study the $E_{\mathrm{T}}^{\mathrm{miss}}$ trigger.

In order to study the performance of the $E_{\mathrm{T}}^{\mathrm{miss}}$ trigger with minimal selection bias, the sample of events must have been triggered by criteria independent of $E_{\mathrm{T}}^{\mathrm{miss}}$. Events selected by a random trigger (zero-bias) are ideal but the sample was statistically limiting. Events triggered by muon triggers are an alternative to events triggered by a random trigger with one caveat. Randomly triggered events are dominantly background-only events with low p_{T} products and $E_{\mathrm{T}}^{\mathrm{miss}}$. However, in events with a muon, the underlying event has on average a higher p_{T} than a background event would have simply due to the p_{T} scale of muons ($\mathcal{O}(25\,\mathrm{GeV})$). This is still relatively small in comparison to jet-triggered events, where the p_{T} scale of jets is $\mathcal{O}(100\,\mathrm{GeV})$. Furthermore, muons deposit insignificant energy in the calorimeter, whereas jets deposit all their energy in the calorimeter. This fact, along with the relatively low p_{T} scale of muons, makes muon-triggered events somewhat representative of events with background $E_{\mathrm{T}}^{\mathrm{miss}}$ in the calorimeter.

Jet-triggered events can be used to study the effect of mis-measurement from high p_{T} objects. Di-jet events from hard scatters form the second largest fraction of all collision events, after events without hard scatters. The fake $E_{\mathrm{T}}^{\mathrm{miss}}$ in these events arises from mis-measurement of jets and is significant enough, again due to the high p_{T} scale of jets, to contribute to the $E_{\mathrm{T}}^{\mathrm{miss}}$ trigger rate.

The following triggers were used to select events for study:

`HLT_j*`: Trigger requiring the presence of at least one jet identified by the HLT jet trigger. It should be noted that, while no requirements were imposed in the study on the multiplicity, p_{T} or η of the jets, requirements were imposed by the trigger menu at the time of operation [1].

`HLT_e24_lhmedium`: Trigger requiring at least one electron identified by the HLT electron trigger with $p_{\mathrm{T}} \geq 20\,\mathrm{GeV}$ and medium likelihood (a measure of signal over

[1] The lowest unprescaled jet triggers were `HLT_j260_320eta490` and `HLT_j360`

background of the electron's object identification). Events passing this trigger are primarily vector boson decays containing electrons (e.g. $W \to e\nu$ and $Z \to e^+e^-$). Note that combined electron and $E_{\mathrm{T}}^{\mathrm{miss}}$ triggers were in operation (e.g. `HLT_e60_lhloose_xe60noL1`).

`HLT_mu24_imedium`: Trigger requiring the presence of at least one muon identified by the HLT muon trigger with $p_{\mathrm{T}} \geq 24\,\mathrm{GeV}$ and medium isolation.

Chapter 6

Results and discussion

This chapter presents the distributions, correlations, efficiencies, and rates of the HLT $E_{\mathrm{T}}^{\mathrm{miss}}$ trigger in 2015 operation and discusses them in detail. Aspects such as the energy scale of $E_{\mathrm{T}}^{\mathrm{miss}}$, the proportion of events above or below a threshold on $E_{\mathrm{T}}^{\mathrm{miss}}$, and the presence of triggers can be deduced from distributions of $E_{\mathrm{T}}^{\mathrm{miss}}$. Correlation plots show the degree to which trigger algorithms reproduce the offline value. The effects of hadronic calibration on the constituents of trigger $E_{\mathrm{T}}^{\mathrm{miss}}$ and the effects of pileup subtraction and correction can be studied in correlation plots. Efficiency plots quantify how well a trigger accepts physics events of interest and rejects background. These plots are constructed with equal rejection rates across all trigger $E_{\mathrm{T}}^{\mathrm{miss}}$ algorithms and are instrumental in judging the performance of an algorithm.

The most important performance metric is efficiency at equal rejection rates. Correlation and distribution plots provide additional information, such as the correlation between different algorithms and the $E_{\mathrm{T}}^{\mathrm{miss}}$ resolution and energy scale. It is the efficiency that directly measures how well the trigger meets its objective: to accept physics of interest at the required level of background rejection.

6.1 Distributions

A distribution of $E_{\mathrm{T}}^{\mathrm{miss}}$ is a histogram that shows the number of events per bin of $E_{\mathrm{T}}^{\mathrm{miss}}$. The $E_{\mathrm{T}}^{\mathrm{miss}}$ distribution of the `physics_Main` stream reflects the rates of all triggers in operation. For example, the `L1_XE50` trigger will reject/accept events with L1 $E_{\mathrm{T}}^{\mathrm{miss}}$ below/above its threshold of 50 GeV. This is observed as a bump at 50 GeV

in the cell $E_{\mathrm{T}}^{\mathrm{miss}}$ distribution shown in Fig. 6.1.

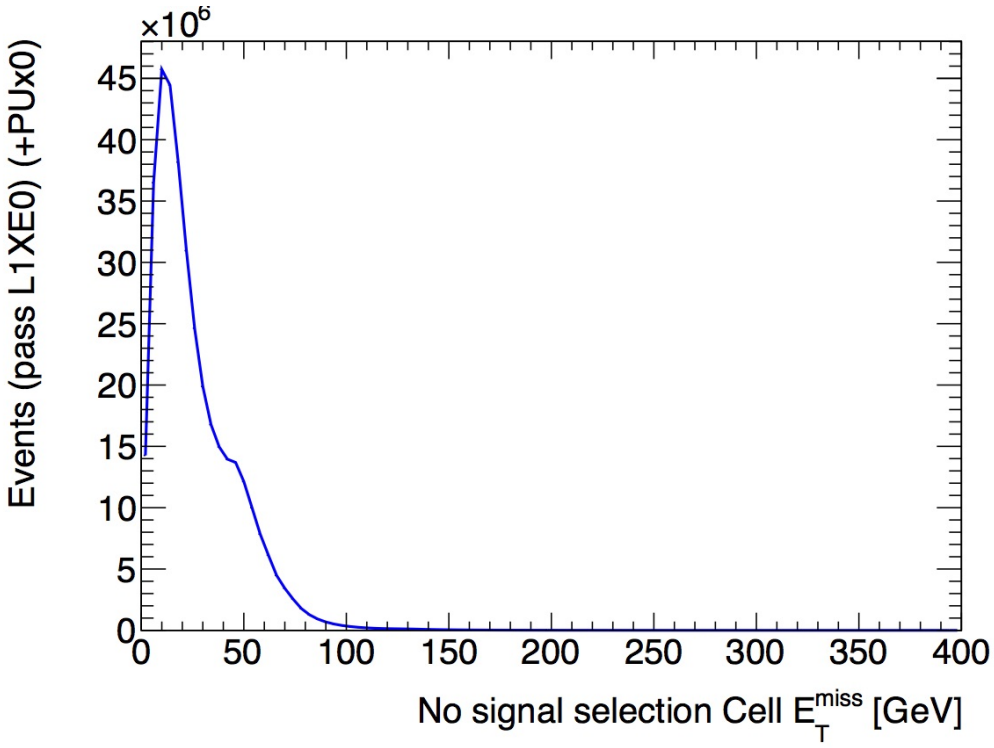

Figure 6.1: Cell $E_{\mathrm{T}}^{\mathrm{miss}}$ distribution of events in the `physics_Main` stream.

In order to keep the trigger rate at a computationally sustainable level, the trigger may be *prescaled*. A prescaled trigger accepts only a fraction of the events that pass its threshold. Typically, the lowest threshold/highest rate $E_{\mathrm{T}}^{\mathrm{miss}}$ trigger is heavily prescaled. Prescaled triggers are used for monitoring and performance studies (e.g. to monitor the distribution of $E_{\mathrm{T}}^{\mathrm{miss}}$ without a high threshold requirement). As an example, the trigger `HLT_noalg_L1XE50` has a 50 GeV threshold on L1 $E_{\mathrm{T}}^{\mathrm{miss}}$ and no requirement at HLT. Due to its very high rate, it was prescaled by a factor of up to 7590; in other words, only one out every 7590 events passing the trigger were accepted. The contribution to the overall trigger rate of prescaled triggers is small compared to that of unprescaled triggers, such as `HLT_xe70_L1XE50`. Out of all unprescaled triggers, the one with the lowest threshold is commonly referred to as the *lowest unprescaled trigger*. The lowest unprescaled $E_{\mathrm{T}}^{\mathrm{miss}}$ trigger in 2015 operation was `HLT_xe70_L1XE50`.

The effect of the `L1_XE50` trigger on HLT $E_{\mathrm{T}}^{\mathrm{miss}}$ distributions is shown as the dashed lines in the following figures. Fig. 6.2a shows the HLT $E_{\mathrm{T}}^{\mathrm{miss}}$ distributions of events passing the `HLT_mu24_imedium` trigger. As described in the previous chapter,

the events selected by this trigger contain pre-dominantly background $E_{\mathrm{T}}^{\mathrm{miss}}$. During data taking, the majority of events are accepted by non-$E_{\mathrm{T}}^{\mathrm{miss}}$ triggers and form the `physics_Main` distributions shown in Fig. 6.2b. The variety of triggers contributing events to a $E_{\mathrm{T}}^{\mathrm{miss}}$ distribution – each of which have different rates – makes it difficult to pinpoint the origin of $E_{\mathrm{T}}^{\mathrm{miss}}$ features. For this reason, the data were separated by imposing trigger requirements.

The distributions of jet-triggered events and of the `physics_Main` stream have a higher fraction of events passing the `L1_XE50` trigger than in distributions of muon-triggered and electron-triggered events. This is because jet-triggered events have on average a higher p_{T} scale muon- or electron-triggered events. In the case of the `physics_Main` stream, this is because $E_{\mathrm{T}}^{\mathrm{miss}}$ and jet triggers are included.

Shown in Fig. 6.2 and 6.3 are the distributions of $E_{\mathrm{T}}^{\mathrm{miss}}$ in events passing trigger selections, with the dashed lines corresponding to an additional `L1_XE50` requirement. The muon contribution to the offline $E_{\mathrm{T}}^{\mathrm{miss}}$ was removed to make the offline $E_{\mathrm{T}}^{\mathrm{miss}}$ comparable to the trigger $E_{\mathrm{T}}^{\mathrm{miss}}$ [1]. The effect of hadronic calibration on offline objects and online topoclusters and jets is reflected by the consistently higher scale (rightwards shift) of their respective $E_{\mathrm{T}}^{\mathrm{miss}}$ relative to that of cell $E_{\mathrm{T}}^{\mathrm{miss}}$. This is clearly evident in the correlations shown in Ch. 6.2. The `L1_XE50` trigger suppresses events in the low $E_{\mathrm{T}}^{\mathrm{miss}}$ region up to $\sim 60\,\mathrm{GeV}$ and has diminished effect in the tail region, as intended. For a significant portion of events, the `TopoclPUC` algorithm did not find a tower with E_{T} above a threshold of 45 GeV and registered zero $E_{\mathrm{T}}^{\mathrm{miss}}$ for the event.

The distributions of events triggered on random colliding bunches is shown in Fig. 6.3. The events in these distributions have insignificant (if any) genuine $E_{\mathrm{T}}^{\mathrm{miss}}$ and only have pileup interactions and other backgrounds. In comparison to signal and object triggered-distributions, zero-bias distributions are peaked at very low $E_{\mathrm{T}}^{\mathrm{miss}}$ and fall steeply.

Shown in Fig. 6.4 are the distributions of $E_{\mathrm{T}}^{\mathrm{miss}}$ in events passing signal selections, with the dashed lines corresponding to an additional `L1_XE50` requirement. A bias in $E_{\mathrm{T}}^{\mathrm{miss}}$ will result from imposing any threshold cuts on $E_{\mathrm{T}}^{\mathrm{miss}}$ in the event selection. The $W \to e\nu$ and $W \to \mu\nu$ selections both impose cuts on offline $E_{\mathrm{T}}^{\mathrm{miss}}$ and the reconstructed transverse W mass (which is a function of offline $E_{\mathrm{T}}^{\mathrm{miss}}$) [2]. These cuts

[1] By removing the muon contribution, the offline $E_{\mathrm{T}}^{\mathrm{miss}}$ becomes a calorimeter and track-based quantity. The trigger $E_{\mathrm{T}}^{\mathrm{miss}}$ is unaffected and continues to be a calorimeter-based quantity, since the muon correction built into the trigger was not enabled during 2015 operation.

[2] $m_T = \sqrt{2p_T^{\ell} E_{\mathrm{T}}^{\mathrm{miss}}[1 - cos\Delta\phi(p_T^{\ell}, E_{\mathrm{T}}^{\mathrm{miss}})]}$

Figure 6.2: Distributions of HLT $E_{\mathrm{T}}^{\mathrm{miss}}$ in events passing trigger selections for different HLT algorithms.

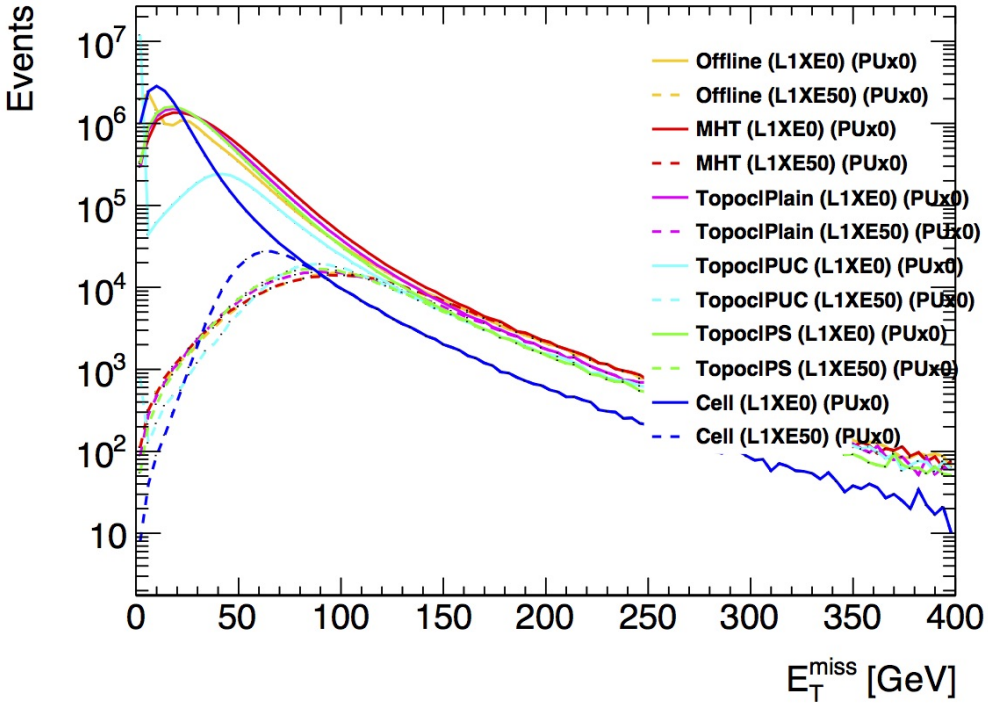

(a) With `HLT_mu24_imedium` selection

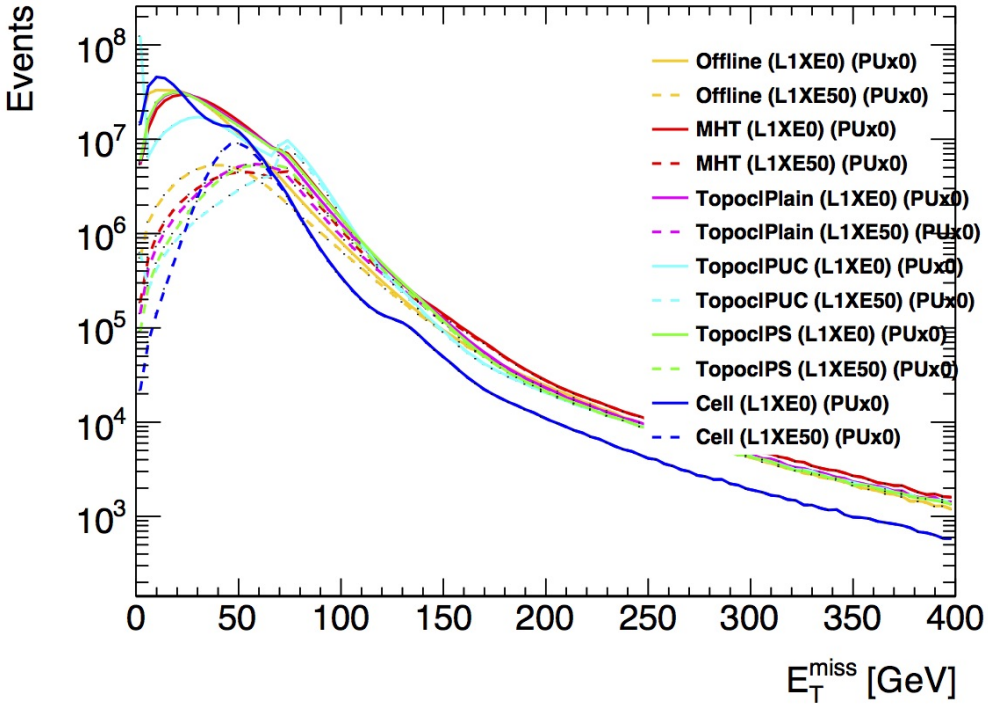

(b) `physics_Main` stream

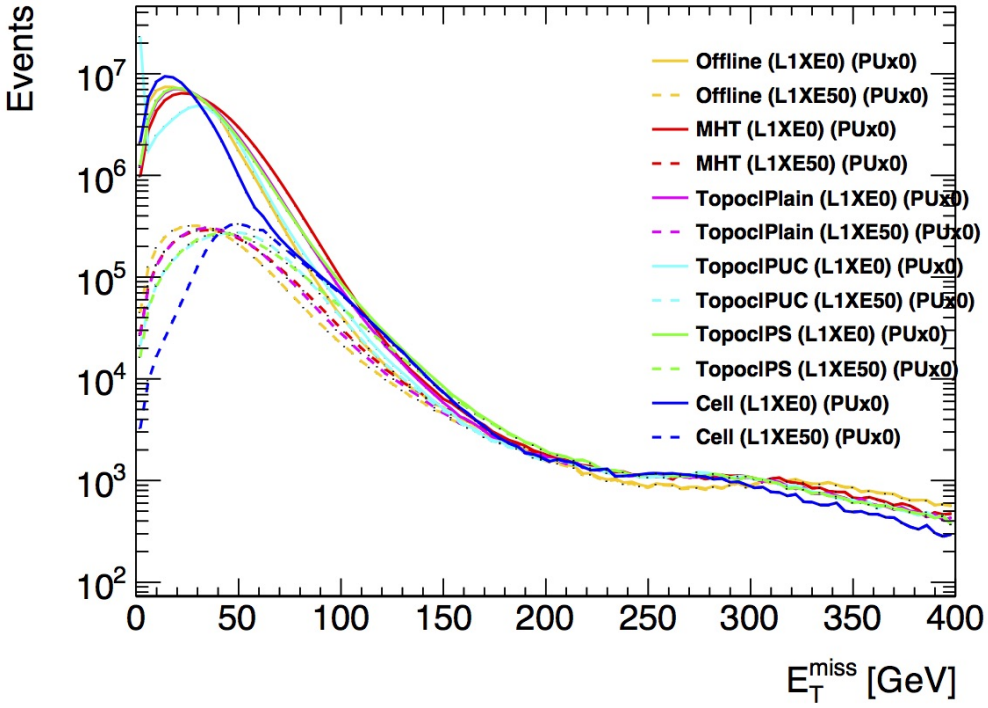

(c) With `HLT_e24_lhmedium` selection

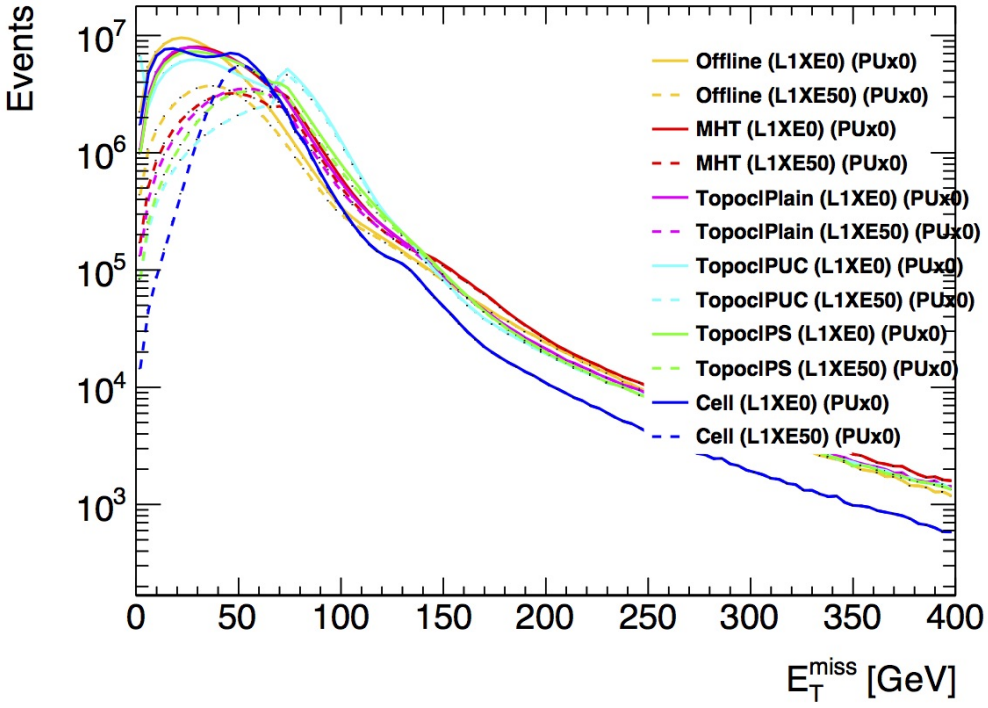

(d) With `HLT_j*` selection

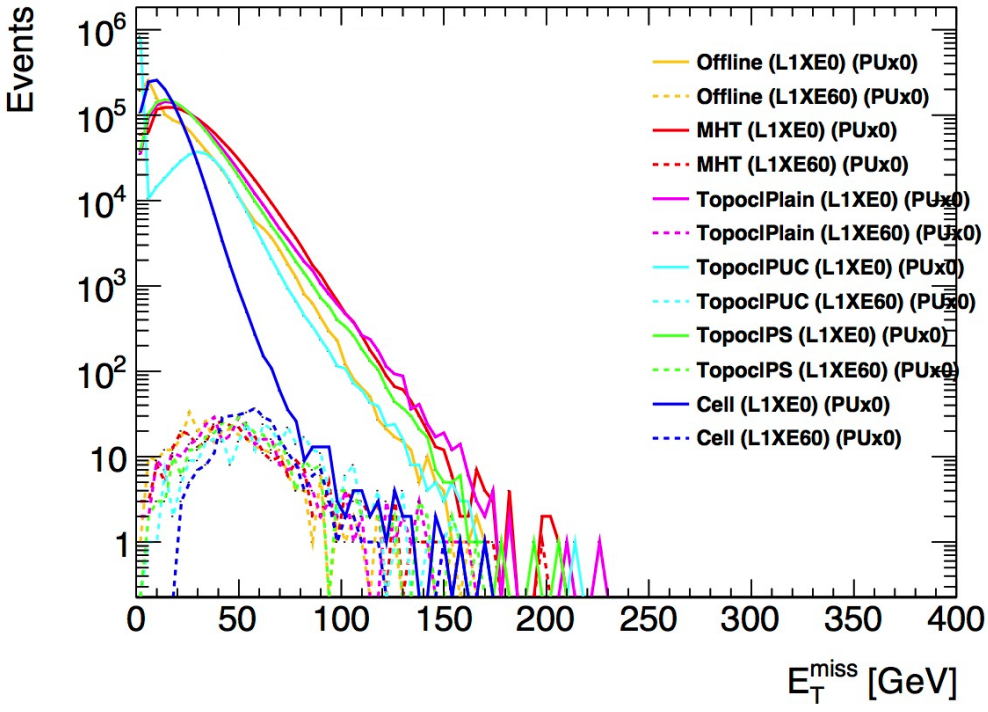

Figure 6.3: Distributions of HLT $E_{\mathrm{T}}^{\mathrm{miss}}$ in events triggered on random colliding bunches (zero-bias) for different HLT algorithms. Note that the dashed lines correspond to a `L1_XE60` requirement.

will bias the $E_{\mathrm{T}}^{\mathrm{miss}}$ distributions towards higher $E_{\mathrm{T}}^{\mathrm{miss}}$.

Judging from the distribution of $W \to e\nu$ events and zero-bias, the shifted peak in the distribution of $W \to e\nu$ events ($\sim 40\,\mathrm{GeV}$) is due to genuine $E_{\mathrm{T}}^{\mathrm{miss}}$. However, note that it would be unfeasible to select these events on the basis of $E_{\mathrm{T}}^{\mathrm{miss}}$ alone, since the rate of events with zero genuine $E_{\mathrm{T}}^{\mathrm{miss}}$ is dominant at this threshold. The presence of muons in both $Z \to \mu\mu$ and `HLT_mu24_imedium` result in similar trigger $E_{\mathrm{T}}^{\mathrm{miss}}$ distributions.

The comparison of trigger $E_{\mathrm{T}}^{\mathrm{miss}}$ to offline $E_{\mathrm{T}}^{\mathrm{miss}}$ is best done by looking at event-by-event correlation and efficiency, as shown in Ch. 6.2 and Ch. 6.3, respectively.

Figure 6.4: Distributions of HLT $E_{\mathrm{T}}^{\mathrm{miss}}$ in events passing signal selections for different HLT algorithms.

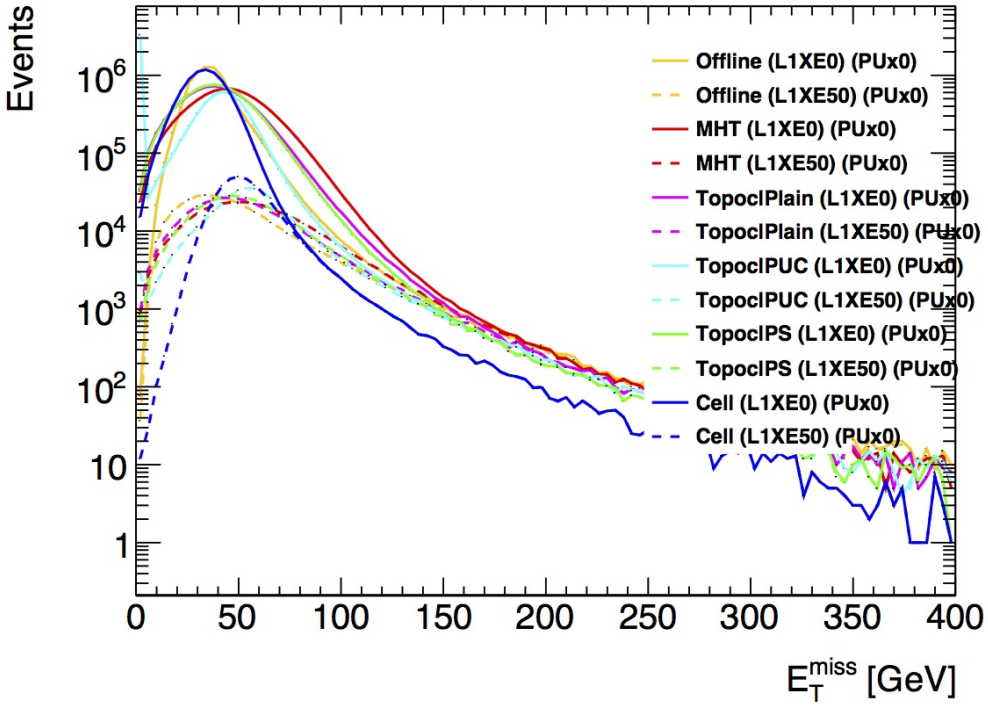

(a) With $W \to e\nu$ selection

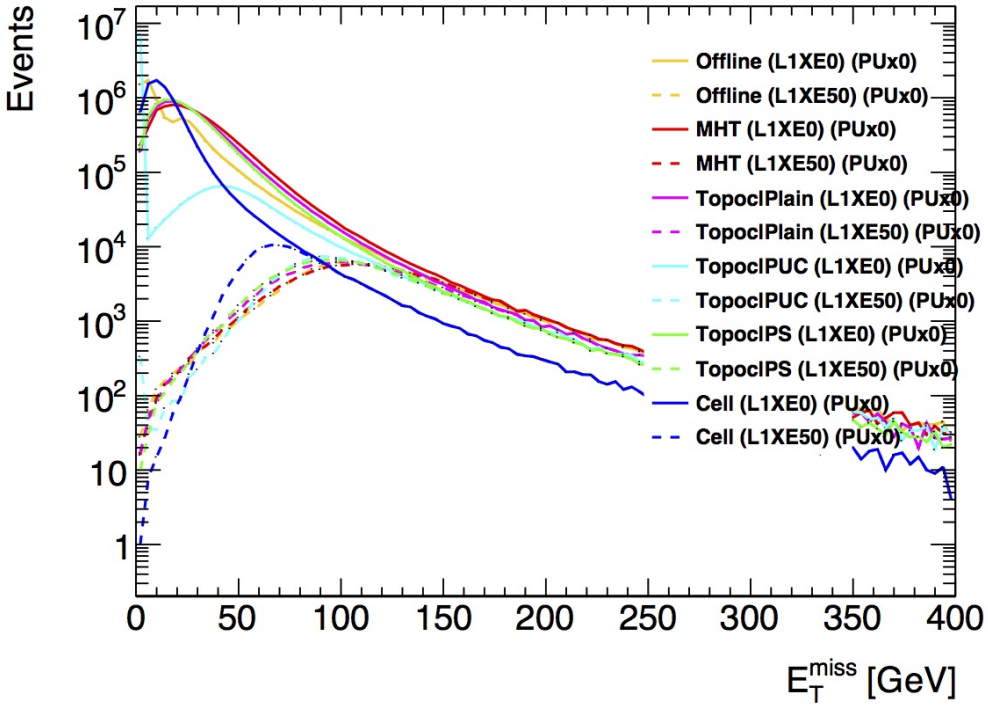

(b) With $W \to \mu\nu$ selection

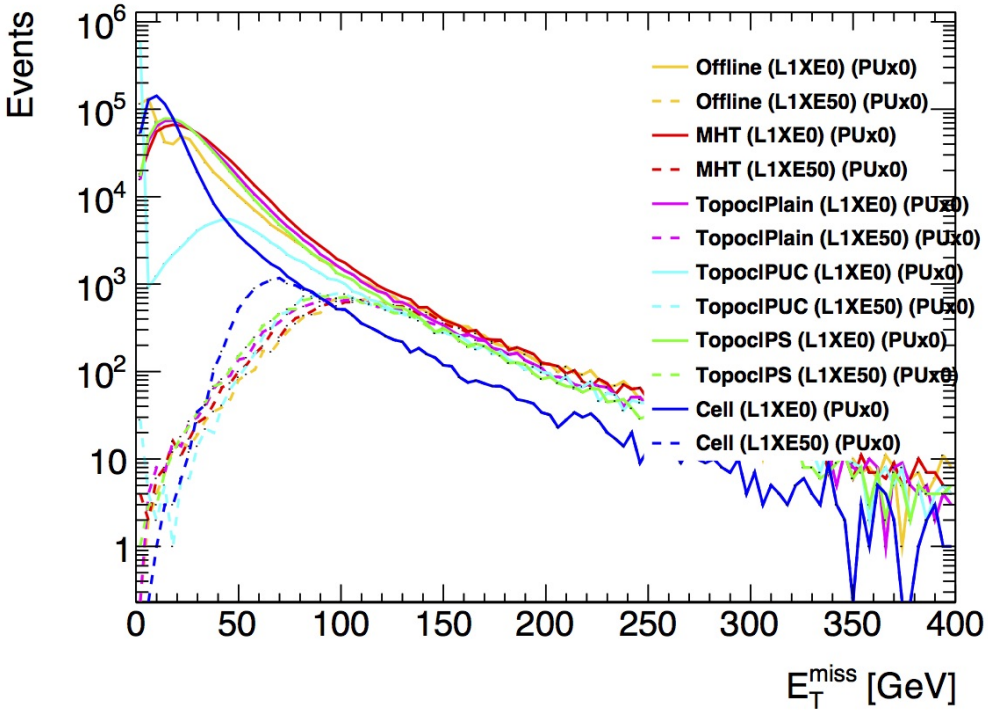

(c) With $Z \to \mu\mu$ selection

6.2 Correlations

Offline reconstructed $E_{\mathrm{T}}^{\mathrm{miss}}$ is the benchmark against which trigger $E_{\mathrm{T}}^{\mathrm{miss}}$ is compared. The degree to which $E_{\mathrm{T}}^{\mathrm{miss}}$ trigger algorithms reproduce offline $E_{\mathrm{T}}^{\mathrm{miss}}$ is given by their event-by-event correlation. Ideally, the trigger $E_{\mathrm{T}}^{\mathrm{miss}}$ would equal the offline $E_{\mathrm{T}}^{\mathrm{miss}}$ in every event. This would result in perfect correlation. A correlation plot is a two-dimensional histogram binned in trigger $E_{\mathrm{T}}^{\mathrm{miss}}$ and offline $E_{\mathrm{T}}^{\mathrm{miss}}$ with the z-axis (colour axis) representing the number of events in each trigger $E_{\mathrm{T}}^{\mathrm{miss}}$ - offline $E_{\mathrm{T}}^{\mathrm{miss}}$ bin. Perfect correlation between the two $E_{\mathrm{T}}^{\mathrm{miss}}$ variables would result in a diagonal pattern in a correlation plot.

In a correlation plot of L1 $E_{\mathrm{T}}^{\mathrm{miss}}$ versus HLT $E_{\mathrm{T}}^{\mathrm{miss}}$, events in the upper left corner have a high L1 $E_{\mathrm{T}}^{\mathrm{miss}}$ and low HLT $E_{\mathrm{T}}^{\mathrm{miss}}$. In these events, the L1 algorithm over-estimated the amount of $E_{\mathrm{T}}^{\mathrm{miss}}$, relative to the HLT value. These events would be rejected by the HLT. Events in the lower right corner have a low L1 $E_{\mathrm{T}}^{\mathrm{miss}}$ and a high HLT $E_{\mathrm{T}}^{\mathrm{miss}}$. In these events, the L1 algorithm under-estimated the amount of $E_{\mathrm{T}}^{\mathrm{miss}}$ relative to the HLT value. These events were rejected by L1 but would not be rejected by the HLT. Clearly, this pre-mature rejection by L1 is undesirable. Similarly, the events in the lower right corner of a HLT $E_{\mathrm{T}}^{\mathrm{miss}}$ versus offline $E_{\mathrm{T}}^{\mathrm{miss}}$ correlation plot correspond to events that were rejected by HLT but would be accepted on the basis of their offline $E_{\mathrm{T}}^{\mathrm{miss}}$ value.

The most significant factor in correlation with offline $E_{\mathrm{T}}^{\mathrm{miss}}$ is hadronic calibration. Shown in Fig. 6.5 are the correlations between trigger $E_{\mathrm{T}}^{\mathrm{miss}}$ and offline $E_{\mathrm{T}}^{\mathrm{miss}}$ for `HLT_mu24_imedium`-triggered events. Cell $E_{\mathrm{T}}^{\mathrm{miss}}$, which uses calorimeter cells at electromagnetic scale, has on average lower $E_{\mathrm{T}}^{\mathrm{miss}}$ than offline, as evidenced by the correlation (Fig. 6.5a), which is tilted downwards. The same behaviour is seen in L1 $E_{\mathrm{T}}^{\mathrm{miss}}$ (Fig. 6.6a) since the constituents of L1 $E_{\mathrm{T}}^{\mathrm{miss}}$ (calorimeter towers) are also at electromagnetic scale.

This is resolved in topocluster $E_{\mathrm{T}}^{\mathrm{miss}}$ and $H_{\mathrm{T}}^{\mathrm{miss}}$, which use LCW- (and JES-) calibrated constituents. Topocluster $E_{\mathrm{T}}^{\mathrm{miss}}$ and $H_{\mathrm{T}}^{\mathrm{miss}}$ have on average closer values to offline, as evidenced by their more diagonal correlation (Fig. 6.5b and 6.5e, respectively). The correlation of topocluster $E_{\mathrm{T}}^{\mathrm{miss}}$ is unaffected by pileup subtraction (PS) (Fig. 6.5c) and is similar to that of $H_{\mathrm{T}}^{\mathrm{miss}}$. Note that the correlation of topocluster (PUC) $E_{\mathrm{T}}^{\mathrm{miss}}$ (Fig. 6.5d) excludes events where the `TopoclPUC` algorithm registered zero $E_{\mathrm{T}}^{\mathrm{miss}}$; hence, the correlation looks markedly better.

The double lobes seen at low $E_{\mathrm{T}}^{\mathrm{miss}}$ arise from a small fraction of events where

the muon contribution was not fully removed from the offline $E_{\mathrm{T}}^{\mathrm{miss}}$. This feature is also seen in $E_{\mathrm{T}}^{\mathrm{miss}}$ distributions of $W \rightarrow \mu\nu$, $Z \rightarrow \mu\mu$, and muon-triggered events (Fig. 6.4b, 6.4c, and 6.2a).

Not surprisingly, tower-based L1 $E_{\mathrm{T}}^{\mathrm{miss}}$ correlates well with cell $E_{\mathrm{T}}^{\mathrm{miss}}$, as shown in Fig. 6.6c. This is because both use electromagnetic scale constituents and are based on similar quantities (the latter builds towers out of calorimeter cells). The observed spread in correlation arises from differences in gain, timing, calibration, noise suppression, and resolution. The lobe at low L1 $E_{\mathrm{T}}^{\mathrm{miss}}$ extending to high topocluster $E_{\mathrm{T}}^{\mathrm{miss}}$ seen in Fig. 6.6b is due to a higher $E_{\mathrm{T}}^{\mathrm{miss}}$ scale for topocluster $E_{\mathrm{T}}^{\mathrm{miss}}$ arising from hadronic calibration.

The effect of hadronic calibration is clear in correlations of $t\bar{t}$ events, which have hadronic activity. The scale difference is more evident in $t\bar{t}$ events because $t\bar{t}$ events always have significant hadronic activity, whereas the events shown in the preceding correlation plots (muon-triggered events) do not always have hadronic activity. By using hadronic scale constituents, topocluster $E_{\mathrm{T}}^{\mathrm{miss}}$ and offline $E_{\mathrm{T}}^{\mathrm{miss}}$ significantly improve the correlation, as shown in Fig. 6.7. Fig. 6.8 shows the scale difference at the trigger level, without the additional calibration and corrections of offline $E_{\mathrm{T}}^{\mathrm{miss}}$, by plotting the correlation of cell $E_{\mathrm{T}}^{\mathrm{miss}}$ versus topocluster $E_{\mathrm{T}}^{\mathrm{miss}}$.

Figure 6.5: Correlations between trigger $E_{\mathrm{T}}^{\mathrm{miss}}$ and offline $E_{\mathrm{T}}^{\mathrm{miss}}$ in events passing the `HLT_mu24_imedium` trigger.

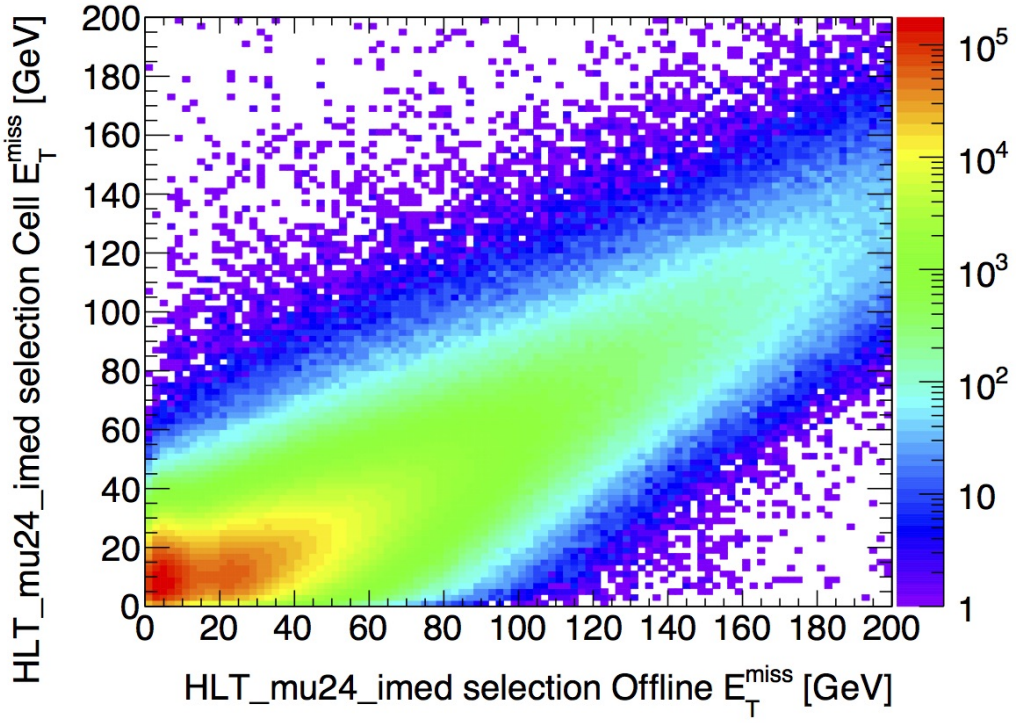

(a) Cell $E_{\mathrm{T}}^{\mathrm{miss}}$

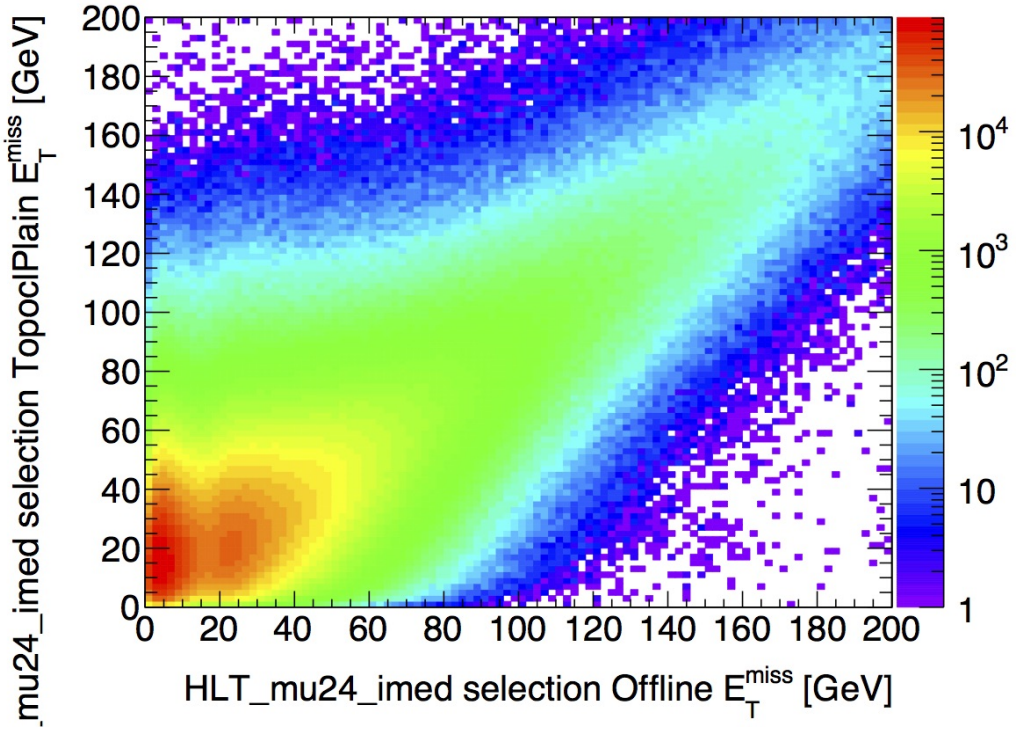

(b) Topocluster $E_{\mathrm{T}}^{\mathrm{miss}}$

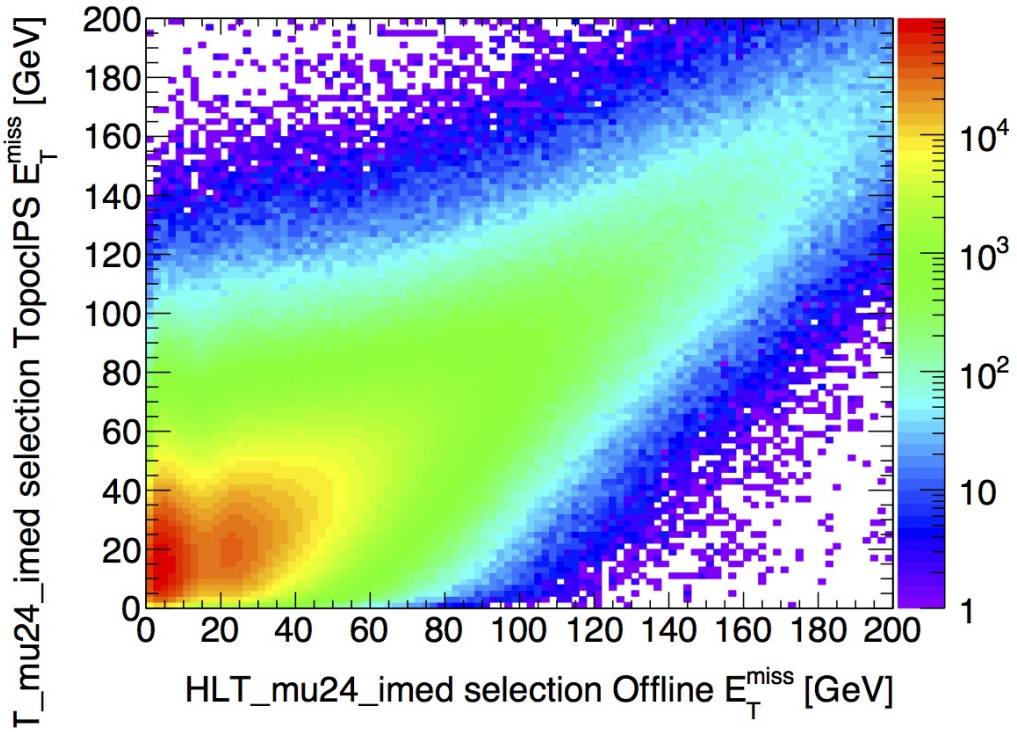

(c) Topocluster (PS) $E_{\mathrm{T}}^{\mathrm{miss}}$

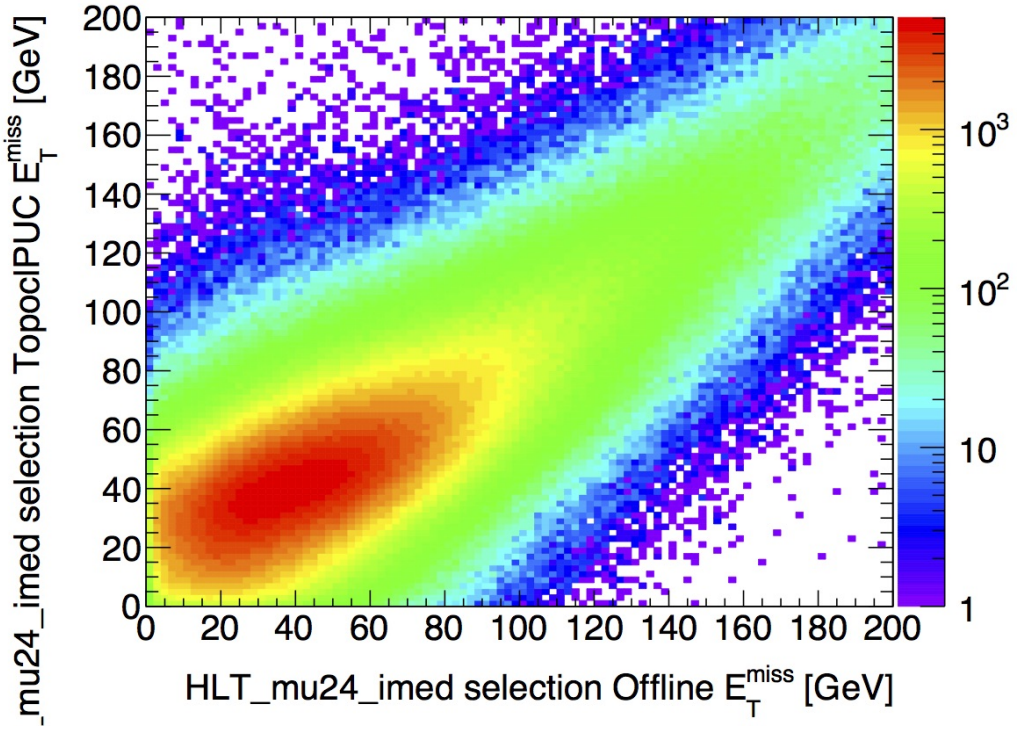

(d) Topocluster (PUC) $E_{\mathrm{T}}^{\mathrm{miss}}$

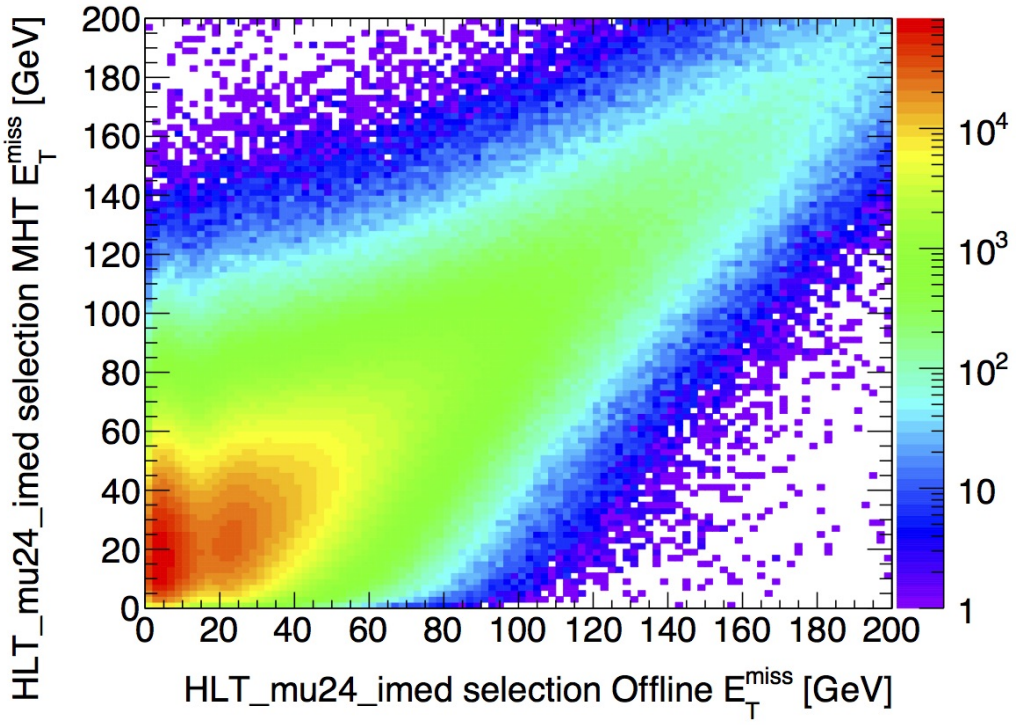

(e) $H_{\mathrm{T}}^{\mathrm{miss}}$

Figure 6.6: Correlations with L1 $E_{\mathrm{T}}^{\mathrm{miss}}$ in events passing the `HLT_mu24_imedium` trigger.

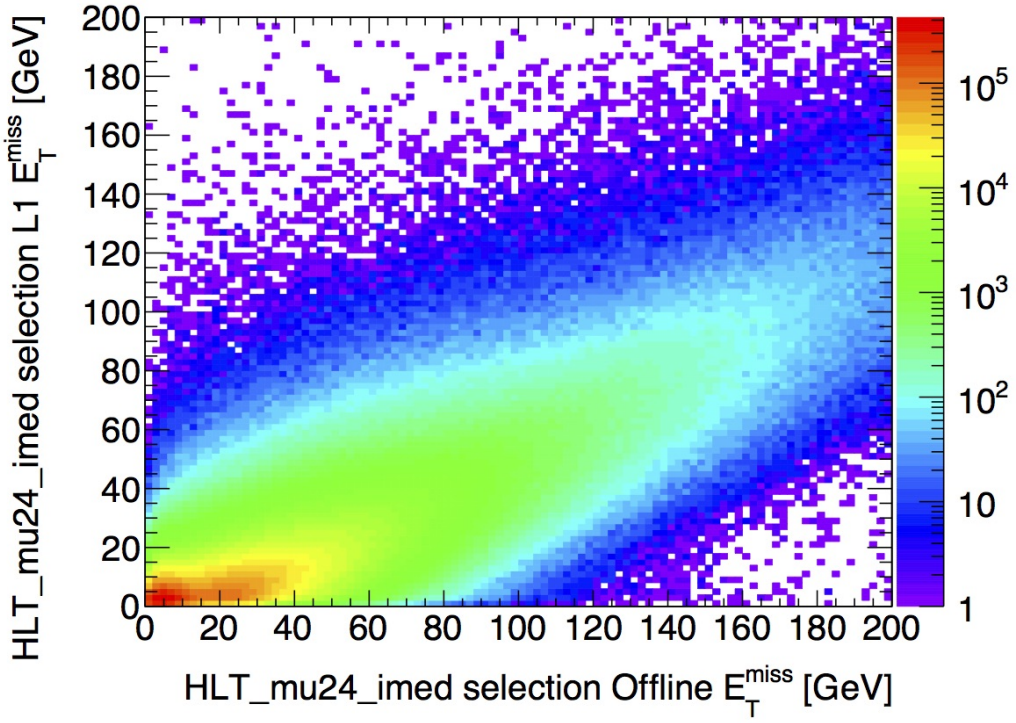

(a) L1 $E_{\mathrm{T}}^{\mathrm{miss}}$ vs. Offline $E_{\mathrm{T}}^{\mathrm{miss}}$

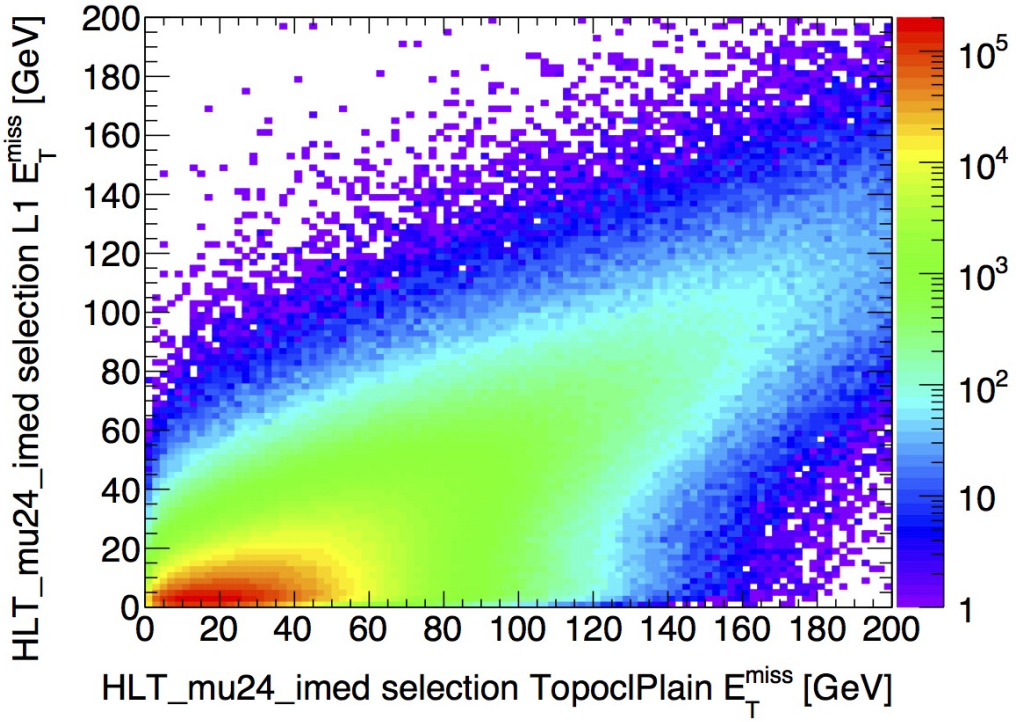

(b) L1 $E_{\mathrm{T}}^{\mathrm{miss}}$ vs. Topocluster $E_{\mathrm{T}}^{\mathrm{miss}}$

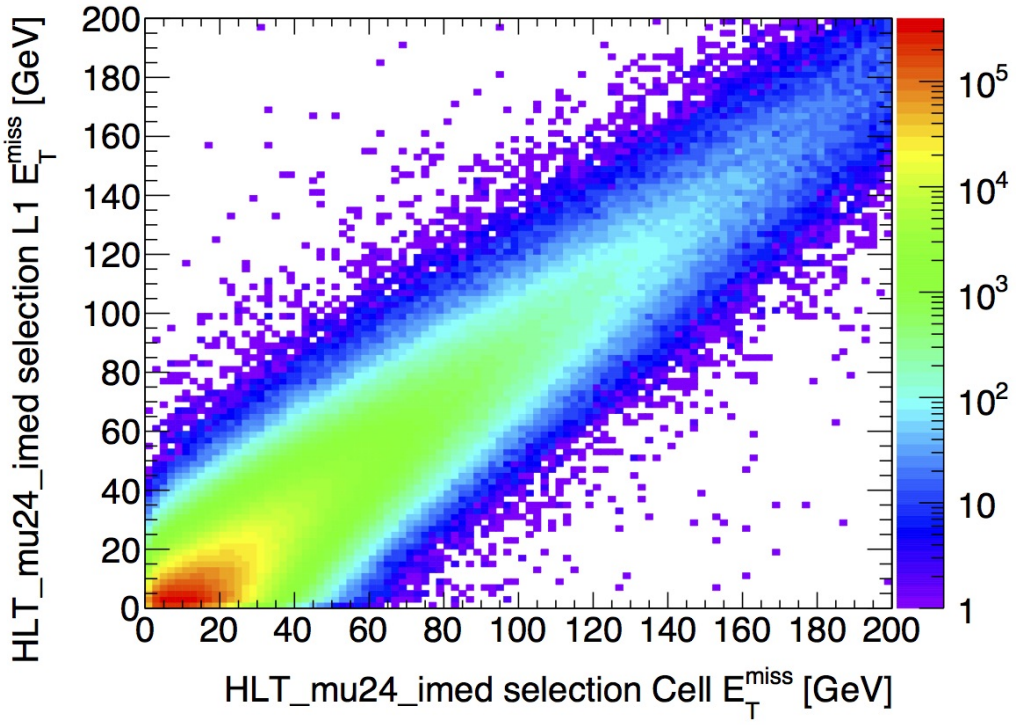

(c) L1 $E_{\mathrm{T}}^{\mathrm{miss}}$ vs. Cell $E_{\mathrm{T}}^{\mathrm{miss}}$

Figure 6.7: Correlations between trigger $E_{\mathrm{T}}^{\mathrm{miss}}$ and offline $E_{\mathrm{T}}^{\mathrm{miss}}$ in $t\bar{t}$ events.

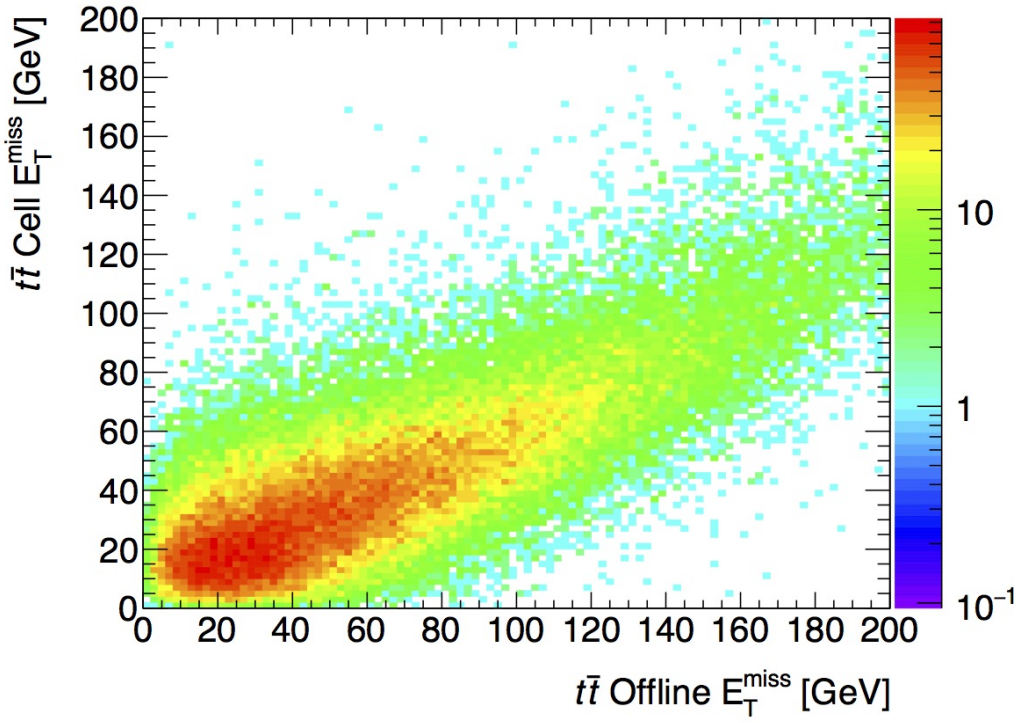

(a) Cell $E_{\mathrm{T}}^{\mathrm{miss}}$

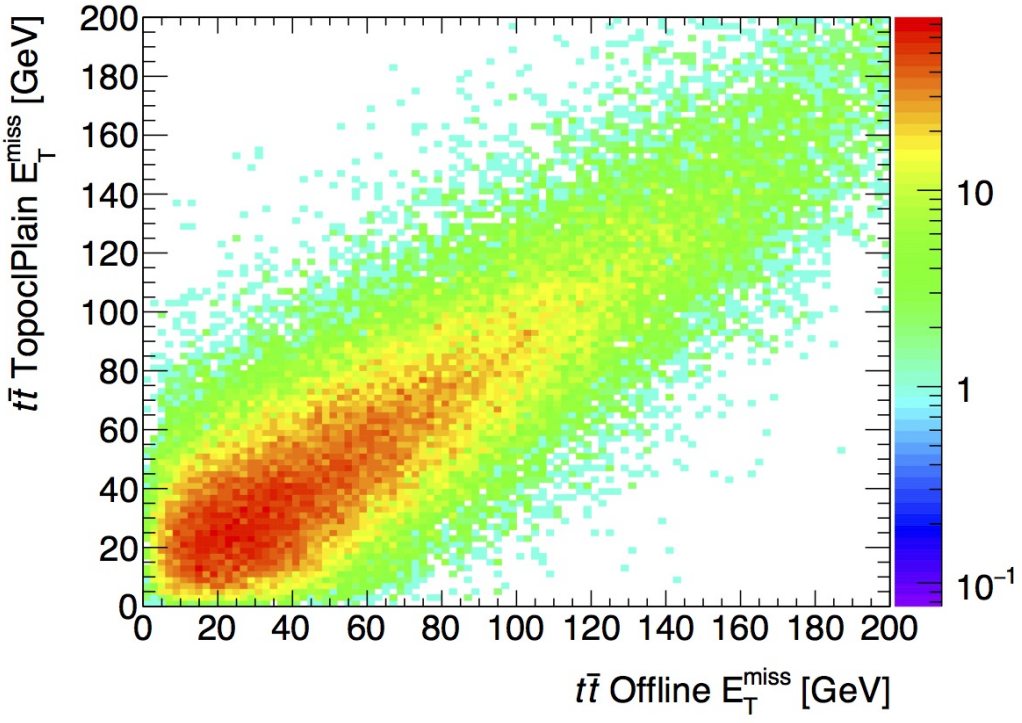

(b) Topocluster $E_{\mathrm{T}}^{\mathrm{miss}}$

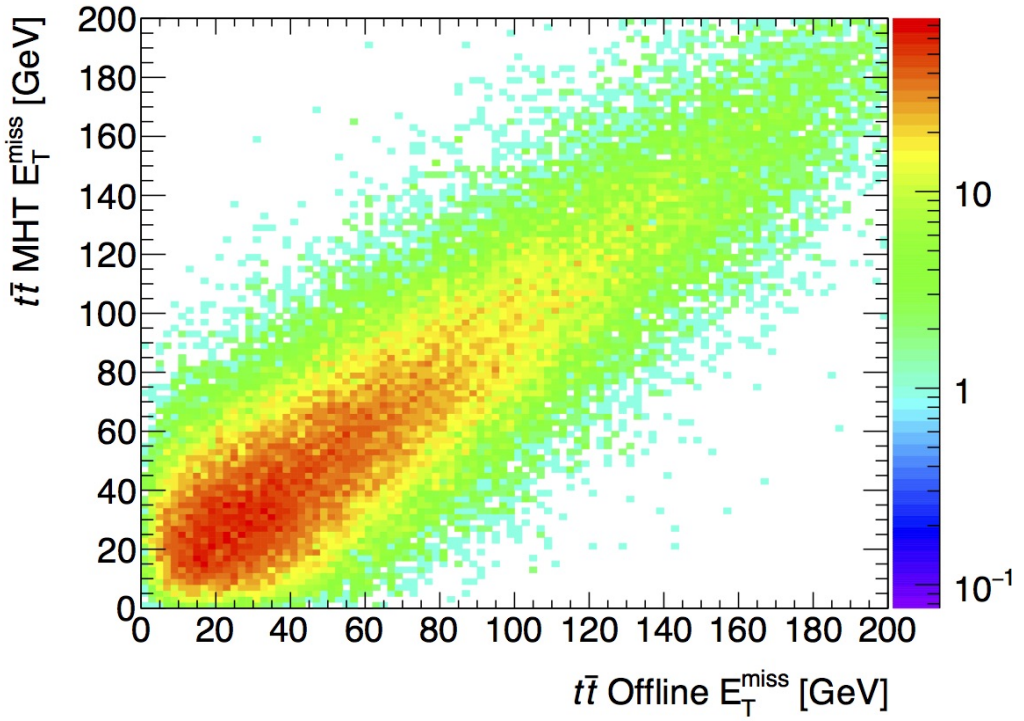

(c) $H_{\mathrm{T}}^{\mathrm{miss}}$

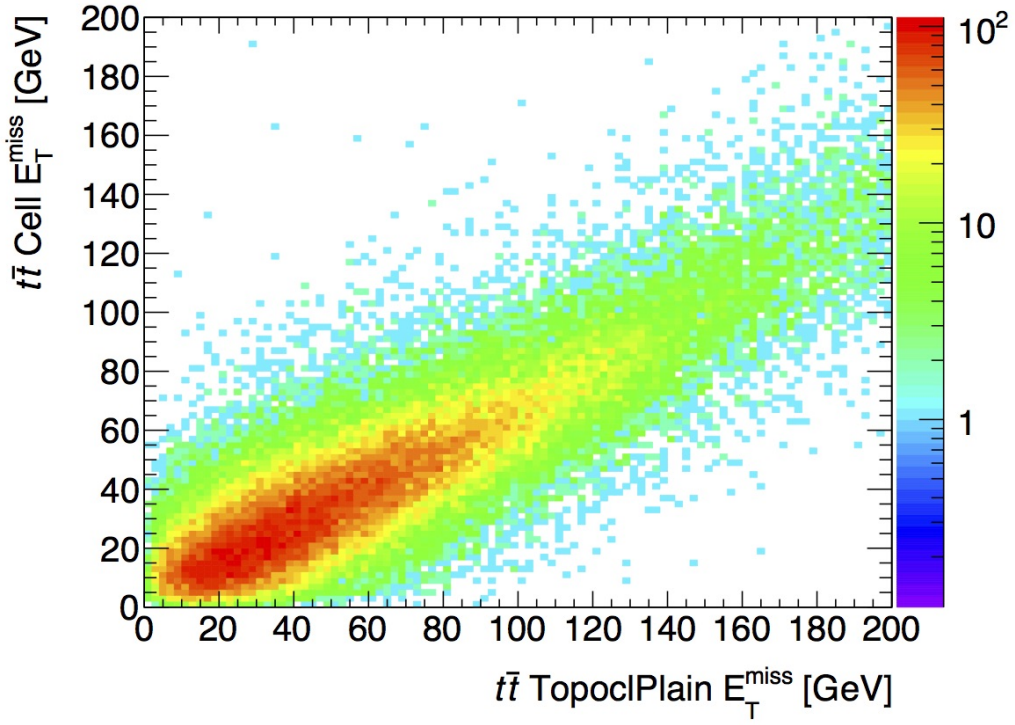

Figure 6.8: Correlation between cell $E_{\mathrm{T}}^{\mathrm{miss}}$ and topocluster $E_{\mathrm{T}}^{\mathrm{miss}}$ in $t\bar{t}$ events.

6.3 Efficiencies

The efficiency of a trigger is the fraction of events that pass a trigger $E_{\mathrm{T}}^{\mathrm{miss}}$ threshold T as a function of the offline $E_{\mathrm{T}}^{\mathrm{miss}}$ [3]. If the trigger $E_{\mathrm{T}}^{\mathrm{miss}}$ matches the offline $E_{\mathrm{T}}^{\mathrm{miss}}$ with perfect precision (i.e. equaling the offline value), then the efficiency of the trigger would be zero for $E_{\mathrm{T}}^{\mathrm{miss}} < T$ and 100% for $E_{\mathrm{T}}^{\mathrm{miss}} \geq T$. In practice, efficiency is never a step function due to effects of resolution, calibration, and background. It is instead a smooth function (e.g. sigmoid) that "turns-on" around the threshold cut, T.

The steepness of the turn-on behaviour is dependent on the trigger $E_{\mathrm{T}}^{\mathrm{miss}}$ resolution and threshold of the turn-on midpoint is dependent on the scale of the trigger $E_{\mathrm{T}}^{\mathrm{miss}}$. The turn-on midpoint (i.e. at 50% efficiency) for hadronic scale trigger $E_{\mathrm{T}}^{\mathrm{miss}}$ will occur at a lower value of offline $E_{\mathrm{T}}^{\mathrm{miss}}$ than for electromagnetic scale trigger $E_{\mathrm{T}}^{\mathrm{miss}}$. In order reflect operational behaviour, the thresholds used to calculate efficiency should be close to their respective operational values. However, algorithms can differ in rate when compared at the same threshold due to algorithmic differences in determining $E_{\mathrm{T}}^{\mathrm{miss}}$. The response to genuine $E_{\mathrm{T}}^{\mathrm{miss}}$ differs between hadronic scale $E_{\mathrm{T}}^{\mathrm{miss}}$ and electromagnetic scale $E_{\mathrm{T}}^{\mathrm{miss}}$ – as demonstrated by the correlation plots – and gives rise to different trigger rates. Since rate is the main driver in determining operational thresholds, $E_{\mathrm{T}}^{\mathrm{miss}}$ trigger algorithms should be compared at equal rates. To do this, the threshold used to calculate efficiency for each algorithm was derived by fixing the rate for the algorithm in question to the rate of `HLT_xe80` (cell $E_{\mathrm{T}}^{\mathrm{miss}}$) for `HLT_mu24_imedium`-triggered events [4].

Shown in Fig. 6.9 are the trigger efficiencies for signal-selected events passing the `L1_XE50` trigger with the applied thresholds indicated. The `L1_XE50` trigger was required in addition to a threshold on HLT in order to reflect the overall efficiency of the trigger chains in operation.

Monte Carlo simulations prior to "Run-2" indicated that cell $E_{\mathrm{T}}^{\mathrm{miss}}$ out-performed topocluster $E_{\mathrm{T}}^{\mathrm{miss}}$ in terms of efficiency. In 2015 data, topocluster $E_{\mathrm{T}}^{\mathrm{miss}}$ and $H_{\mathrm{T}}^{\mathrm{miss}}$ performed equally as well as cell $E_{\mathrm{T}}^{\mathrm{miss}}$ in terms of efficiency, and in some cases better than cell $E_{\mathrm{T}}^{\mathrm{miss}}$ (depending on the signal in question). There were effectively no differences for analyses working in the plateau region (i.e. those with an offline $E_{\mathrm{T}}^{\mathrm{miss}}$ cut of 180 GeV). For analyses working in the turn-on region, topocluster $E_{\mathrm{T}}^{\mathrm{miss}}$ and $H_{\mathrm{T}}^{\mathrm{miss}}$ provided sharper turn-on and higher efficiency at the same rate. The efficiency

[3] Efficiency is calculated by counting, in bins of offline $E_{\mathrm{T}}^{\mathrm{miss}}$, the number of events with trigger $E_{\mathrm{T}}^{\mathrm{miss}} > T$ and then dividing by the number of total events.

[4] 10 GeV above the lowest unprescaled threshold in 2015 operation.

Figure 6.9: HLT $E_{\mathrm{T}}^{\mathrm{miss}}$ trigger efficiencies at equal rate in events passing signal selections and `L1_XE50`.

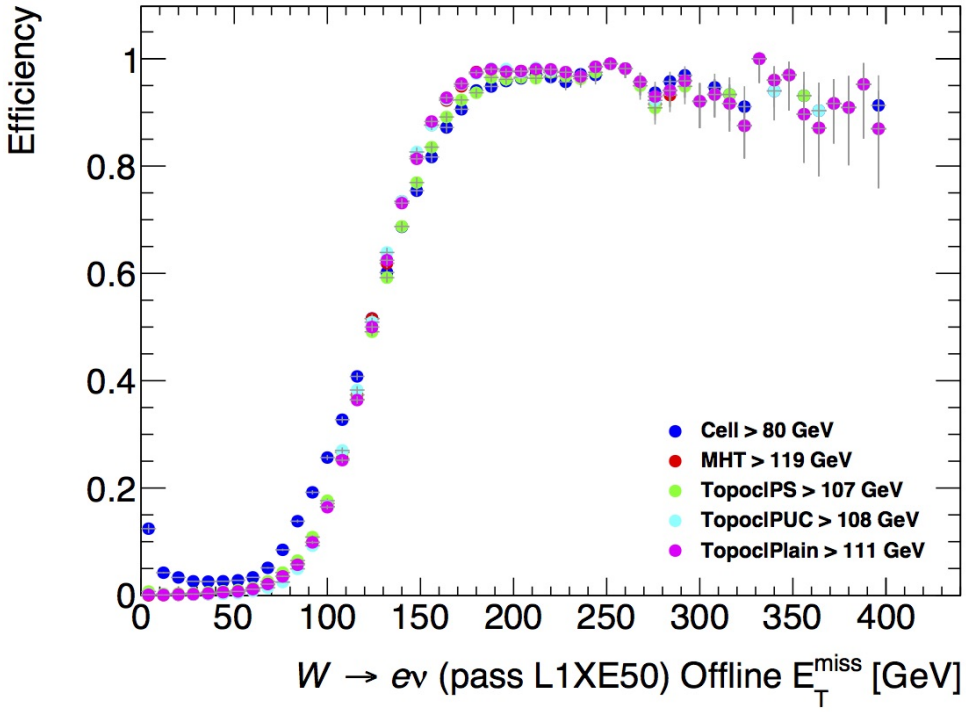

(a) With $W \to e\nu$ selection

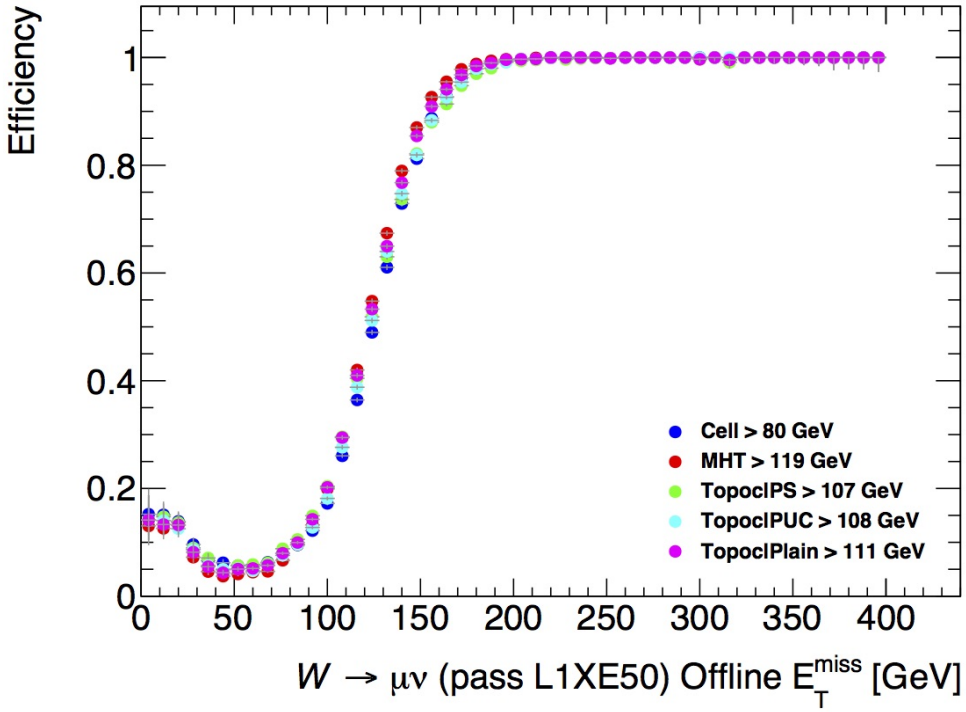

(b) With $W \to \mu\nu$ selection

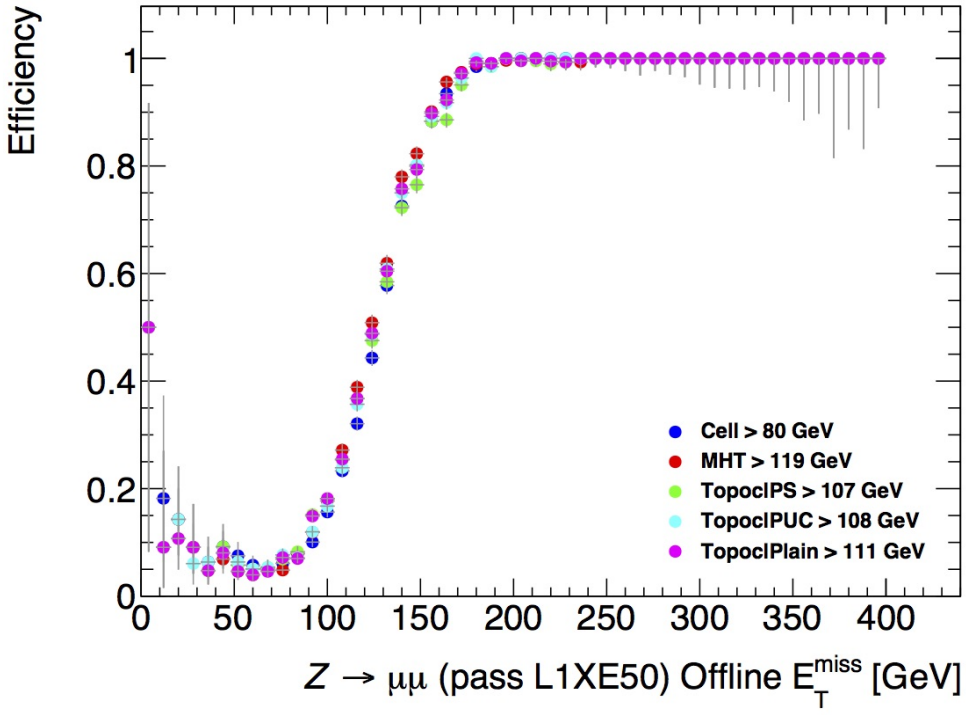

(c) With $Z \to \mu\mu$ selection

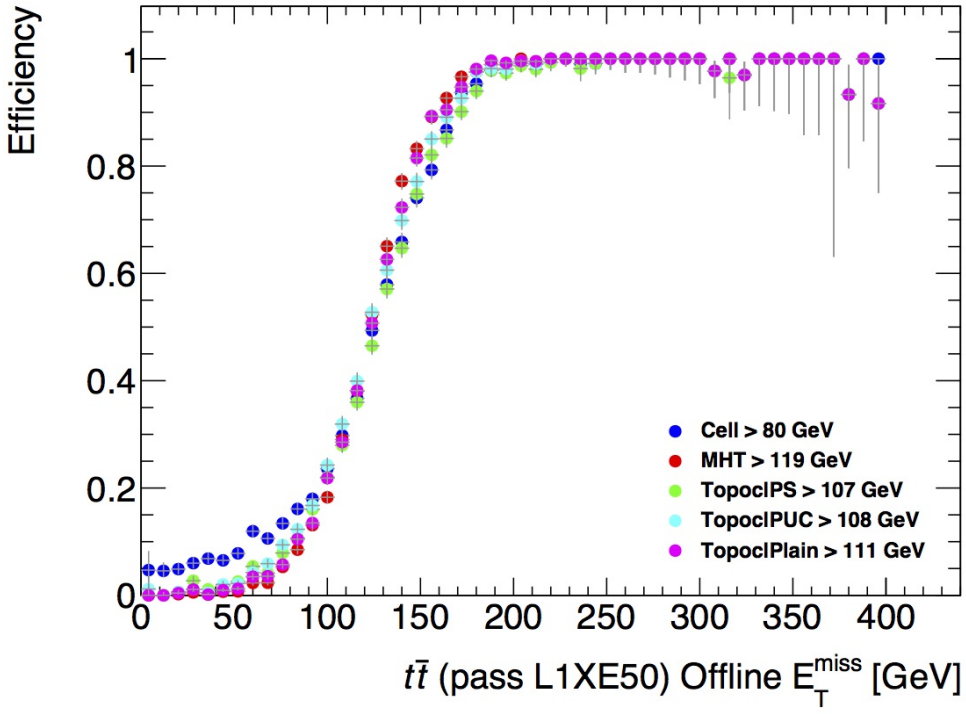

(d) With $t\bar{t}$ selection

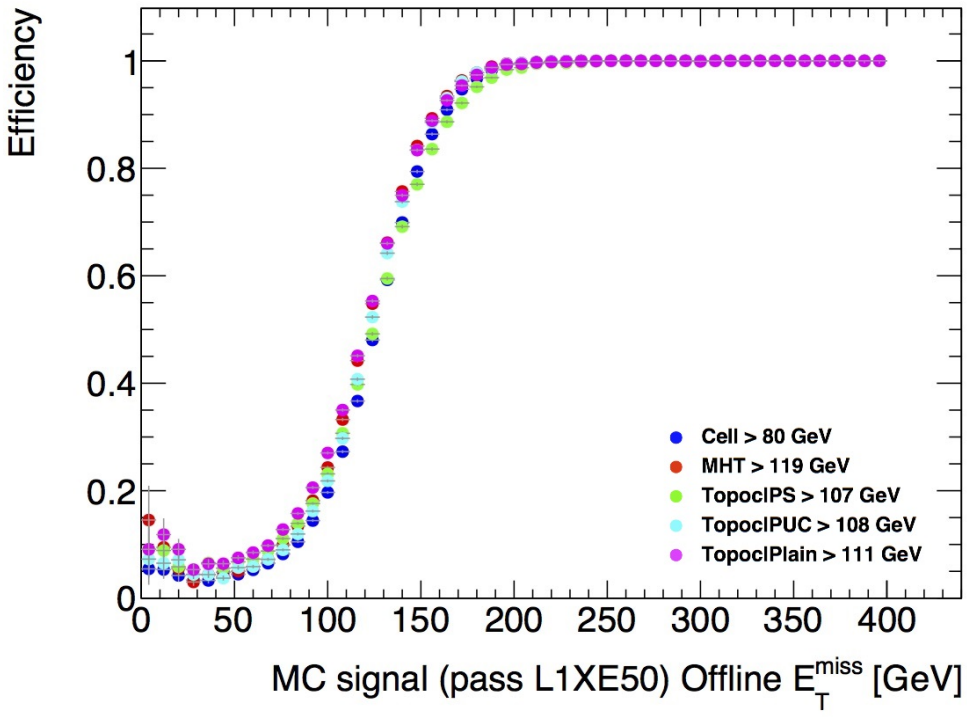

Figure 6.10: HLT $E_{\mathrm{T}}^{\mathrm{miss}}$ trigger efficiencies in simulated $ZH \to \nu\bar{\nu}b\bar{b}$ events passing `L1_XE50`.

plots shown in Fig. 6.9 show similar behaviour in the turn-on midpoint region for all algorithms. In the case of $W \to e\nu$ and $t\bar{t}$ (Fig. 6.9a and 6.9d, respectively) the turn-on is less sharp for cell $E_{\mathrm{T}}^{\mathrm{miss}}$. The drop in efficiency for $W \to e\nu$ events at offline $E_{\mathrm{T}}^{\mathrm{miss}}$ past 250 GeV could be due to electrons going into a region with overlapping calorimetry and having their energy mis-measured. The statistics in this range are poor because very few $W \to e\nu$ have $E_{\mathrm{T}}^{\mathrm{miss}}$ in this range. The non-zero efficiency at low $E_{\mathrm{T}}^{\mathrm{miss}}$ results from the non-zero resolution in $E_{\mathrm{T}}^{\mathrm{miss}}$ even when the offline $E_{\mathrm{T}}^{\mathrm{miss}}$ is zero.

Aside from efficiency, topocluster $E_{\mathrm{T}}^{\mathrm{miss}}$ and $H_{\mathrm{T}}^{\mathrm{miss}}$ were recommended by the $E_{\mathrm{T}}^{\mathrm{miss}}$ trigger group because while their energy scales were higher than cell $E_{\mathrm{T}}^{\mathrm{miss}}$ due to hadronic calibration of their constituents, they operated at or close to the same thresholds as cell $E_{\mathrm{T}}^{\mathrm{miss}}$ (70 GeV). Since the lowest unprescaled thresholds for all the HLT $E_{\mathrm{T}}^{\mathrm{miss}}$ triggers were the same, the differences in energy scale imply that the efficiency curves of hadronic trigger $E_{\mathrm{T}}^{\mathrm{miss}}$ would be to the left of electromagnetic trigger $E_{\mathrm{T}}^{\mathrm{miss}}$ (with turn-on midpoints at lower thresholds).

Shown in Fig. 6.10 is the efficiency for $ZH \to \nu\bar{\nu}b\bar{b}$ simulated events with $\langle\mu\rangle =$

21. As described in Ch. 5, $ZH \to \nu\nu b\bar{b}$ is triggered on $E_{\mathrm{T}}^{\mathrm{miss}}$ and jets; therefore, it is sensitive to the performance of the $E_{\mathrm{T}}^{\mathrm{miss}}$ trigger and its operating thresholds. As a candidate signal sample, it is preferred over $t\bar{t}$ since $t\bar{t}$ decays that produce neutrinos also produce charged leptons that can be triggered by a lepton trigger whereas $ZH \to \nu\bar{\nu}b\bar{b}$ cannot be triggered with a lepton trigger.

Judging from the efficiency for $ZH \to \nu\bar{\nu}b\bar{b}$ and $t\bar{t}$ signals, the $E_{\mathrm{T}}^{\mathrm{miss}}$ trigger operated acceptably in 2015 and at the time of writing this thesis, has been used in eight ATLAS publications on 2015 data. At equal trigger rates, the efficiencies of the various algorithms are similar in the turn-on and plateau regions. Most importantly, they reach near perfect efficiency before entering the range of offline $E_{\mathrm{T}}^{\mathrm{miss}}$ cuts ($\gtrsim 180\,\mathrm{GeV}$). Topocluster $E_{\mathrm{T}}^{\mathrm{miss}}$ and $H_{\mathrm{T}}^{\mathrm{miss}}$ performed marginally better by providing a slightly sharper turn-on.

The strategy for 2016 operation, formulated from conclusions on 2015 data, is to dedicate the majority of the overall HLT $E_{\mathrm{T}}^{\mathrm{miss}}$ trigger rate to the topocluster $E_{\mathrm{T}}^{\mathrm{miss}}$ trigger and the $H_{\mathrm{T}}^{\mathrm{miss}}$ trigger. At luminosities up to $1.2 \times 10^{34}\,\mathrm{cm^{-2}\,s^{-1}}$, the lowest unprescaled trigger is planned to be `HLT_xe100_mht_L1XE50`. The evolution of rates in 2016 is discussed at the end of the following section.

6.4 Rates

The rate of a trigger will increase or decrease inversely with its operating threshold. This threshold must be optimized such that sensitivity to physics of interest is maximized at a computationally sustainable rate. Analyses cutting on $E_{\mathrm{T}}^{\mathrm{miss}}$ in the turn-on region are especially sensitive to increases in the trigger threshold. The maximum bandwidth allocated to the $E_{\mathrm{T}}^{\mathrm{miss}}$ trigger was $\mathcal{O}(200\,\mathrm{Hz})$ for the HLT and $\mathcal{O}(16\,\mathrm{kHz})$ for L1.

The trigger rates of various HLT triggers and of each stream are shown in Fig. A.3 and A.4 in Appendix A. At a peak luminosity of $5 \times 10^{33}\,\mathrm{cm^{-2}\,s^{-1}}$, the `L1_XE50` rate was $\mathcal{O}(0.7\,\mathrm{kHz})$ and the `HLT_xe70_cell_L1XE50` rate was $\mathcal{O}(50\,\mathrm{Hz})$. This represents a L1 reduction factor of $\mathcal{O}(10^4)$ (from a filled bunch crossing rate of 25 to 30 MHz) [5] and a HLT reduction factor of $\mathcal{O}(10^1)$. The overall HLT $E_{\mathrm{T}}^{\mathrm{miss}}$ trigger rate, including combined $E_{\mathrm{T}}^{\mathrm{miss}}+X$ triggers and other HLT $E_{\mathrm{T}}^{\mathrm{miss}}$ algorithms (all operating at 70 GeV) was $\mathcal{O}(200\,\mathrm{Hz})$.

[5] While the bunch crossing rate is 40 MHz, not all bunches are filled by the LHC.

Significant increases in rate were observed in early 2016 operation, as shown in Fig. 6.11. The instantaneous luminosity was increased from $4 \times 10^{33}\,\mathrm{cm}^{-2}\,\mathrm{s}^{-1}$ to $8 \times 10^{33}\,\mathrm{cm}^{-2}\,\mathrm{s}^{-1}$ (corresponding to an increase in $\langle\mu\rangle$ from approximately 20 to 30). This increased the rate for topocluster-based $E_{\mathrm{T}}^{\mathrm{miss}}$ from $\sim 30\,\mathrm{Hz}$ to $\sim 230\,\mathrm{Hz}$ and for $H_{\mathrm{T}}^{\mathrm{miss}}$ from $\sim 25\,\mathrm{Hz}$ to $\sim 130\,\mathrm{Hz}$. Cell-based $E_{\mathrm{T}}^{\mathrm{miss}}$ was less susceptible to the increase in pileup, with an increase to only $\sim 15\,\mathrm{Hz}$ from $\sim 5\,\mathrm{Hz}$. Methods of reducing the rate by adjusting clustering thresholds and/or requiring a p_{T} threshold on forward jets were being discussed at the time of writing.

Figure 6.11: Trigger rates observed in early 2016 operation [36].

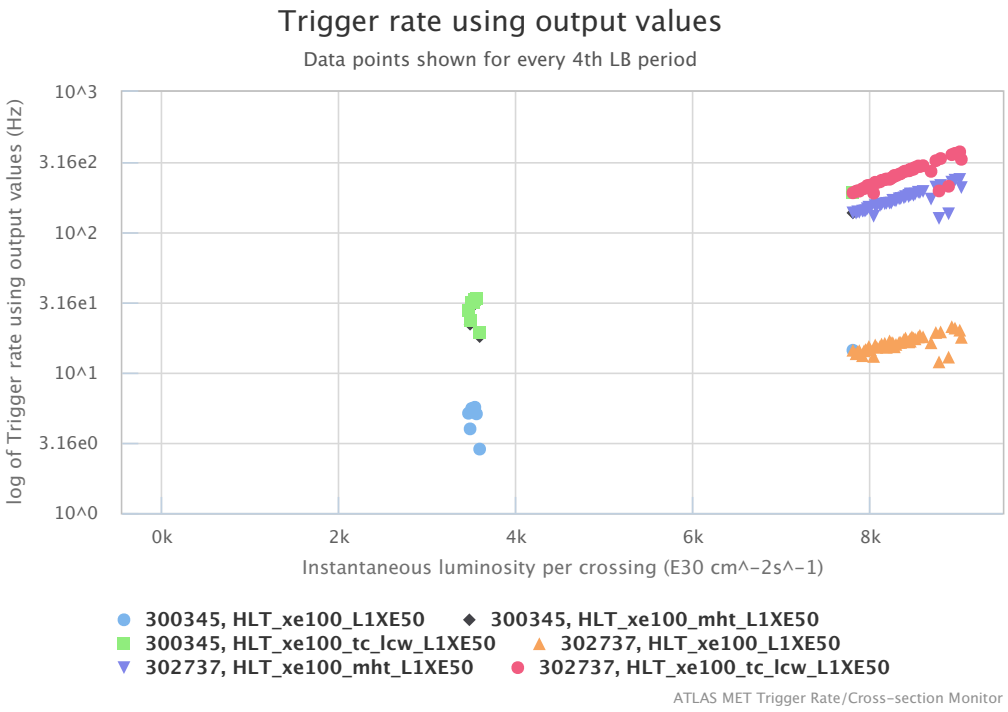

(a) Versus instantaneous luminosity

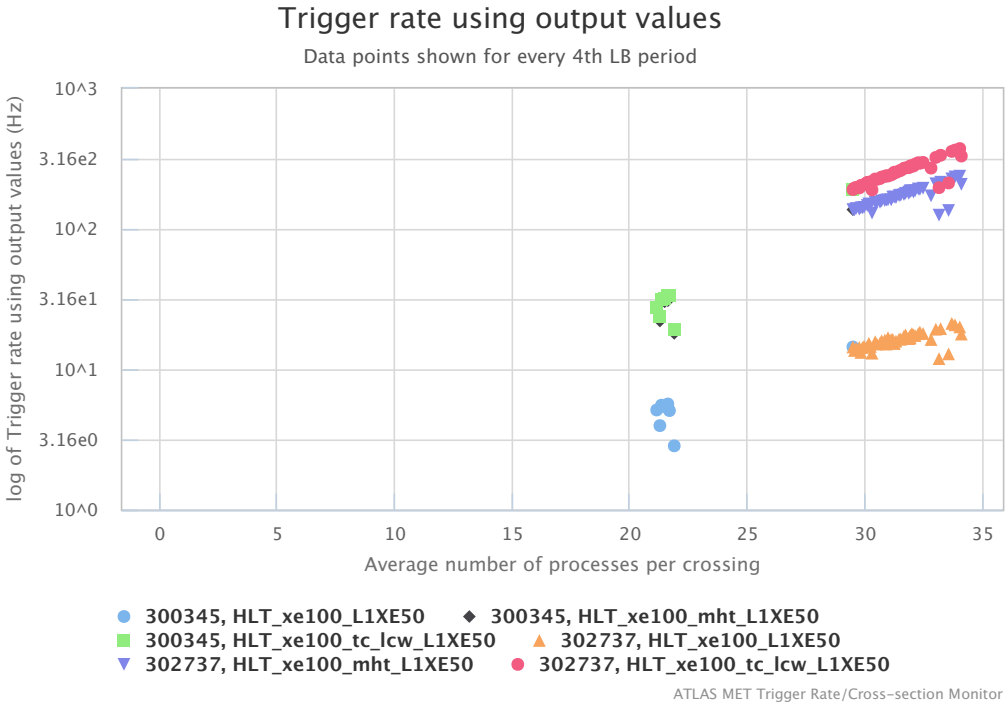

(b) Versus average number of interactions per bunch crossing, $\langle\mu\rangle$

Chapter 7

Conclusions

A study of the performance of the ATLAS HLT $E_{\mathrm{T}}^{\mathrm{miss}}$ trigger in 2015 operation was performed. In 2015, the trigger operated at a higher centre-of-mass energy and shorter bunch spacing than in previous operation. The studies were made as data was collected, and were used to make recommendations on which algorithms and thresholds should be used. The final results from 2015 were shown in this thesis and were used to formulate a strategy for 2016 operation.

Prior to 2015 operation, simulations indicated that cell-based $E_{\mathrm{T}}^{\mathrm{miss}}$ out-performed topocluster-based $E_{\mathrm{T}}^{\mathrm{miss}}$ in terms of efficiency by providing a sharper turn-on. This behaviour was unexpected as topoclusters were intended to improve the pileup and noise resistance (when compared to using calorimeter cells individually). A value of $\langle\mu\rangle$ higher or comparable to the value seen in 2012 operation ($\langle\mu\rangle = 21$) was expected in 2015 operation. This would have enabled studies of the effects of higher pileup on the $E_{\mathrm{T}}^{\mathrm{miss}}$ trigger.

The performance was studied in the context of various physics signals and trigger streams. In each context, the efficiency, correlation, and rates of the various HLT $E_{\mathrm{T}}^{\mathrm{miss}}$ algorithms were produced and studied. The topocluster-based $E_{\mathrm{T}}^{\mathrm{miss}}$ pileup subtraction and correction algorithms and the $H_{\mathrm{T}}^{\mathrm{miss}}$ algorithm were studied for the first time. Within the limited range of $\langle\mu\rangle$ in the data that was studied, the efficiency curves indicated that differences between algorithms were marginal. Topocluster-based $E_{\mathrm{T}}^{\mathrm{miss}}$ and $H_{\mathrm{T}}^{\mathrm{miss}}$ performed slightly better than cell-based $E_{\mathrm{T}}^{\mathrm{miss}}$ in the turn-on region of $E_{\mathrm{T}}^{\mathrm{miss}}$. This was contrary to what was observed in simulation prior to 2015 operation (as discussed above). Due to the hadronic calibration on topoclusters and jets, topocluster-based $E_{\mathrm{T}}^{\mathrm{miss}}$ and $H_{\mathrm{T}}^{\mathrm{miss}}$ demonstrated markedly better performance in terms of correlation with offline reconstructed $E_{\mathrm{T}}^{\mathrm{miss}}$. Combined with the fact that the

trigger thresholds of topocluster-based $E_{\mathrm{T}}^{\mathrm{miss}}$, cell-based $E_{\mathrm{T}}^{\mathrm{miss}}$, and $H_{\mathrm{T}}^{\mathrm{miss}}$ were equal in 2015 operation, topocluster-based $E_{\mathrm{T}}^{\mathrm{miss}}$ and $H_{\mathrm{T}}^{\mathrm{miss}}$ operated effectively at a lower threshold. The χ^2 minimization-based pileup subtraction algorithm did not improve efficiency but suppressed pileup by its application of a threshold cut on tower E_{T}. The $E_{\mathrm{T}}^{\mathrm{miss}}$ trigger was found to perform acceptably and at the time of writing this thesis, the trigger has been used in eight ATLAS publications on 2015 data. The strategy for 2016 operation, formulated in part from the studies in this thesis on 2015 data, is to dedicate the majority of the overall HLT $E_{\mathrm{T}}^{\mathrm{miss}}$ trigger rate to the topocluster $E_{\mathrm{T}}^{\mathrm{miss}}$ trigger and the $H_{\mathrm{T}}^{\mathrm{miss}}$ trigger.

Significant increases in rate were observed in early 2016 operation. The data collected in 2015 had a lower-than-expected amount of pileup ($\langle\mu\rangle = 14$). This, and the narrow range of $\langle\mu\rangle$ available in 2015 data, limited the possibility of studying the effects of higher pileup. An increase to $\langle\mu\rangle = 23$ was observed in early 2016 operation. Such studies could be made by considering 2016 data.

Appendix A

Additional Information

A.1 Physics signal selections

Object selections common to $W \to e\nu$, $W \to \mu\nu$, and $Z \to \mu\mu$:

Electron selection: Medium likelihood score, $p_{\mathrm{T}} > 25\,\mathrm{GeV}$, $|\eta| < 2.47$ (excluding crack region of 1.37 to 1.52), and gradient level isolation.

Muon selection: Medium ID muon (imposes $|\eta| < 2.4$), $p_{\mathrm{T}} > 25\,\mathrm{GeV}$, and gradient level isolation.

$W \to e\nu$ event selection:

Trigger: Event must pass `HLT_e24_lhmedium_iloose_L1EM20VH` or `HLT_e60_lhmedium` (medium likelihood score with loose isolation in the calorimeter).

Lepton and electron multiplicity: Event must contain exactly one good lepton, with the lepton being the electron.

W **mass:** The reconstructed transverse W boson mass, calculated from the p_{T} of the electron and offline $E_{\mathrm{T}}^{\mathrm{miss}}$ [1], must be greater than $50\,\mathrm{GeV}$.

$W \to \mu\nu$ event selection:

Trigger: Event must pass `HLT_mu20_iloose_L1MU15` or `HLT_e50`.

[1] $m_T = \sqrt{2p_T^{\ell} E_{\mathrm{T}}^{\mathrm{miss}}[1 - cos\Delta\phi(p_T^{\ell}, E_{\mathrm{T}}^{\mathrm{miss}})]}$

Lepton and muon multiplicity: Event must contain exactly one good lepton, with the lepton being the muon.

W mass: The reconstructed transverse W boson mass, calculated from the p_{T} of the muon and offline $E_{\mathrm{T}}^{\mathrm{miss}}$, must be greater than 50 GeV.

$Z \to \mu\mu$ event selection:

Lepton and muon multiplicity: Event must contain exactly two good leptons, with the leptons being the two muons.

Charge: The muon pair must have opposite charge.

Di-muon mass: The invariant di-muon mass must be within $66\,\mathrm{GeV} < m_{\mu\mu} < 116\,\mathrm{GeV}$.

$t\bar{t}$ event selection:

Lepton multiplicity: At least one good lepton (selected using the object criteria above).

Jet multiplicity: At least four jets.

B-tagged jet multiplicity: At least two b-tagged jets.

A.2 GCW and GS calibration schemes

In the Global Cell Weighting (GCW) scheme, the constituent cells of reconstructed jets are assigned calibration weights depending on the cell's energy density and the calorimeter layer in which the cell resides. The re-weighted energy of the cells is summed to give a preliminary calibrated jet energy. The weights are then re-calculated by χ^2 minimization of the jet energy resolution (represented by the ratio of the preliminary calibrated jet energy to the true jet energy). The first step accounts for the lower hadronic response and the second step accounts for energy lost in cracks. Note that only the cells within the reconstructed jets matched with truth jets are calibrated; hence, this scheme is "global" in the sense that it cannot be applied to all cells for use in $E_{\mathrm{T}}^{\mathrm{miss}}$ reconstruction, for example.

In the Global Sequential Calibration (GS) scheme [37], the jet energy resolution of EM+JES calibrated jets is further optimized while preserving the jet energy scale.

Like in the JES scheme, the response of simulated jets is considered in bins of $p_{\mathrm{T}} - \eta$. For each bin, a multiplicative correction factor is derived for the response as a function of jet p_{T}, η, and one of five other jet variables by inverting the jet response. This derivation is done for five variables (the number of tracks, the track widths, the number of track segments in the MS, and two representing how the jet energy is divided between calorimeter layers). The correction factors are then applied sequentially to remove the dependence on each variable, and the jet energy scale is rescaled back to its original value. These correction factors improve the resolution, reduce the dependence on the flavour of the originating parton, and account for any jet energy lost beyond the calorimeter.

A.3 LAr calorimeter readout

Shown in Fig. A.1.

A.4 Level-1 nMCM pre-processor

The nMCMs – numbering 1984 in total – each have a analog-to-digital converter that can sample at 80 MHz and have a maximum output throughput of 960 MBps. Both are twice that of the old MCMs and were implemented in order to cope with the higher instantaneous luminosity in "Run-2". The nMCMs first digitizes the analog trigger towers and applies dynamic pedestal subtraction and autocorrelation filters [2]. The pedestal subtraction and filtering have a significant effect on $E_{\mathrm{T}}^{\mathrm{miss}}$; the L1 $E_{\mathrm{T}}^{\mathrm{miss}}$ threshold can be reduced by approximately 10 GeV while maintaining a L1 trigger rate of 100 kHz [38]. A peak finder then associates the digitized signal with the bunch crossing it originates from. The trigger towers are then duplicated into two streams and calibrated with look-up tables; one is calibrated at electromagnetic scale (for identification of electrons, photons, and taus) and the other is calibrated at hadronic scale (for identification of jets and calculation of $E_{\mathrm{T}}^{\mathrm{miss}}$ and ΣE_{T} [3]). In the latter

[2] The pedestal is the electronic "baseline" on which the signal is overlaid. The pedestal shifts depending on the current position in the bunch train (a group of bunches) and on the amount of pile-up (which is higher in the forward regions). The dynamic pedestal subtraction – new for "Run-2" – re-computes the pedestal subtraction depending on the position in the bunch train. The autocorrelation filters reduce the effect of out-of-time pileup by applying a finite impulse response filter that uses coefficients derived from past bunch crossings.

[3] This was not used for calculating L1 $E_{\mathrm{T}}^{\mathrm{miss}}$ in 2015 operation

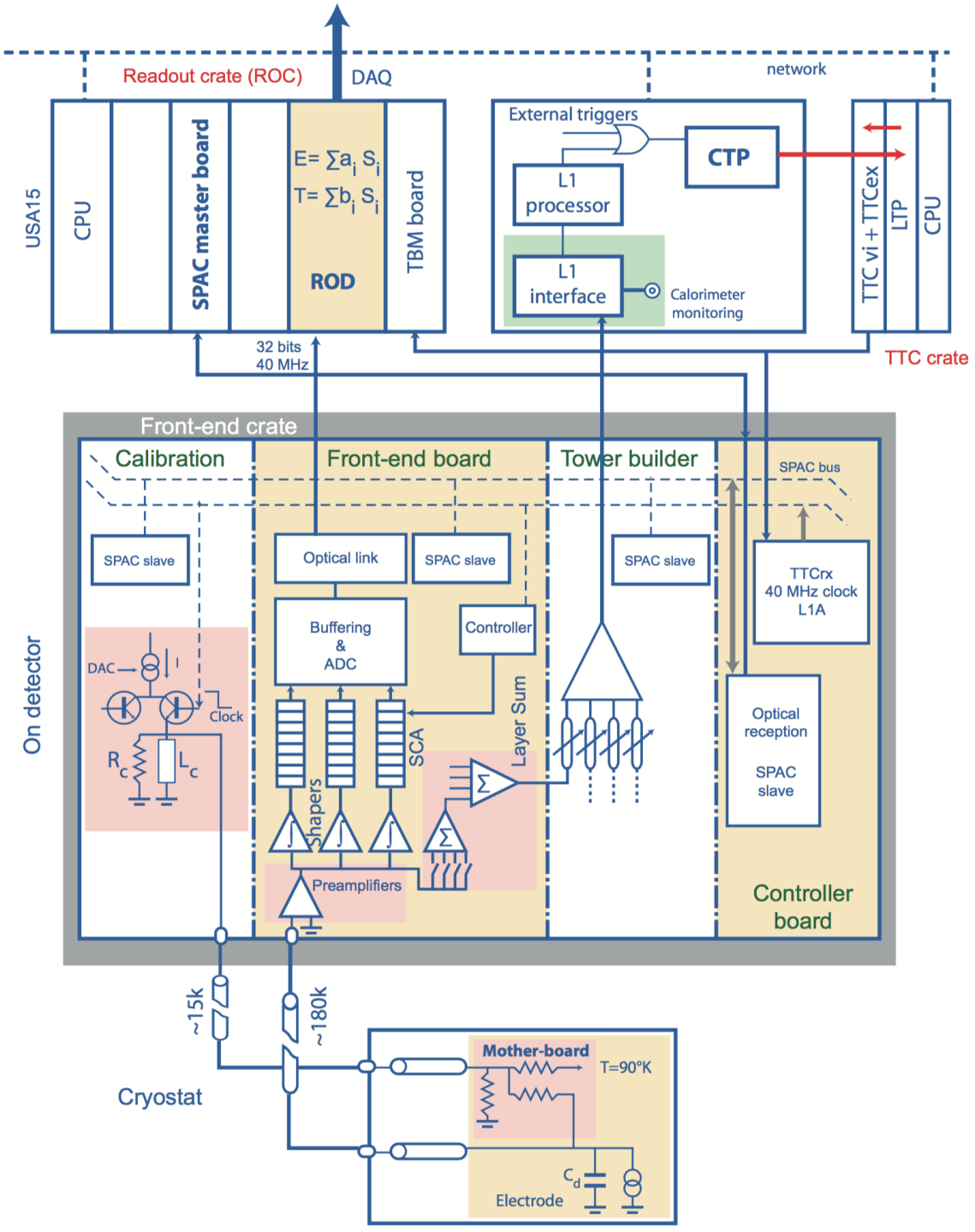

Figure A.1: Layout of the LAr calorimeter front-end electronics [17].

Trigger	Typical offline selection	Trigger Selection		Level-1 Peak Rate (kHz)	HLT Peak Rate (Hz)
		Level-1 (GeV)	HLT (GeV)	$L = 5 \times 10^{33}$ cm^{-2}s^{-1}	
Single leptons	Single iso μ, $p_{\mathrm{T}} > 21$ GeV	15	20	7	130
	Single e, $p_{\mathrm{T}} > 25$ GeV	20	24	18	139
	Single μ, $p_{\mathrm{T}} > 42$ GeV	20	40	5	33
	Single τ, $p_{\mathrm{T}} > 90$ GeV	60	80	2	41
Two leptons	Two μ's, each $p_{\mathrm{T}} > 11$ GeV	2×10	2×10	0.8	19
	Two μ's, $p_{\mathrm{T}} > 19, 10$ GeV	15	18, 8	7	18
	Two loose e's, each $p_{\mathrm{T}} > 15$ GeV	2×10	2×12	10	5
	One e & one μ, $p_{\mathrm{T}} > 10, 26$ GeV	20 (μ)	7, 24	5	1
	One loose e & one μ, $p_{\mathrm{T}} > 19, 15$ GeV	15, 10	17, 14	0.4	2
	Two τ's, $p_{\mathrm{T}} > 40, 30$ GeV	20, 12	35, 25	2	22
	One τ, one μ, $p_{\mathrm{T}} > 30, 15$ GeV	12, 10 (+jets)	25, 14	0.5	10
	One τ, one e, $p_{\mathrm{T}} > 30, 19$ GeV	12, 15 (+jets)	25, 17	1	3.9
Three leptons	Three loose e's, $p_{\mathrm{T}} > 19, 11, 11$ GeV	15, 2×7	17, 2×9	3	< 0.1
	Three μ's, each $p_{\mathrm{T}} > 8$ GeV	3×6	3×6	< 0.1	4
	Three μ's, $p_{\mathrm{T}} > 19, 2 \times 6$ GeV	15	18, 2×4	7	2
	Two μ's & one e, $p_{\mathrm{T}} > 2 \times 11, 14$ GeV	2×10 (μ's)	2×10, 12	0.8	0.2
	Two loose e's & one μ, $p_{\mathrm{T}} > 2 \times 11, 11$ GeV	2×8, 10	2×12, 10	0.3	< 0.1
One photon	one γ, $p_{\mathrm{T}} > 125$ GeV	22	120	8	20
Two photons	Two loose γ's, $p_{\mathrm{T}} > 40, 30$ GeV	2×15	35, 25	1.5	12
	Two tight γ's, $p_{\mathrm{T}} > 25, 25$ GeV	2×15	2×20	1.5	7
Single jet	Jet ($R = 0.4$), $p_{\mathrm{T}} > 400$ GeV	100	360	0.9	18
	Jet ($R = 1.0$), $p_{\mathrm{T}} > 400$ GeV	100	360	0.9	23
$E_{\mathrm{T}}^{\mathrm{miss}}$	$E_{\mathrm{T}}^{\mathrm{miss}} > 180$ GeV	50	70	0.7	55
Multi-jets	Four jets, each $p_{\mathrm{T}} > 95$ GeV	3×40	4×85	0.3	20
	Five jets, each $p_{\mathrm{T}} > 70$ GeV	4×20	5×60	0.4	15
	Six jets, each $p_{\mathrm{T}} > 55$ GeV	4×15	6×45	1.0	12
b−jets	One loose b, $p_{\mathrm{T}} > 235$ GeV	100	225	0.9	35
	Two medium b's, $p_{\mathrm{T}} > 160, 60$ GeV	100	150, 50	0.9	9
	One b & three jets, each $p_{\mathrm{T}} > 75$ GeV	3×25	4×65	0.9	11
	Two b & two jets, each $p_{\mathrm{T}} > 45$ GeV	3×25	4×35	0.9	9
b−physics	Two μ's, $p_{\mathrm{T}} > 6, 4$ GeV plus dedicated b-physics selections	6, 4	6, 4	8	52
Total				70	1400

Figure A.2: Main trigger menu used in 2015 operation for runs at peak luminosity $\mathcal{L} = 5 \times 10^{33}\,\mathrm{cm}^{-2}\,\mathrm{s}^{-1}$ [39].

case, the trigger towers are also summed into *jet elements* of $\Delta\eta \times \Delta\phi = 0.2 \times 0.2$. One stream is sent to a Cluster Processor (CP) and the other stream is sent to a Jet/Energy Processor (JEP).

A.5 Main trigger menu used in 2015 operation and HLT trigger rates

Shown in Fig. A.2, A.3, and A.4.

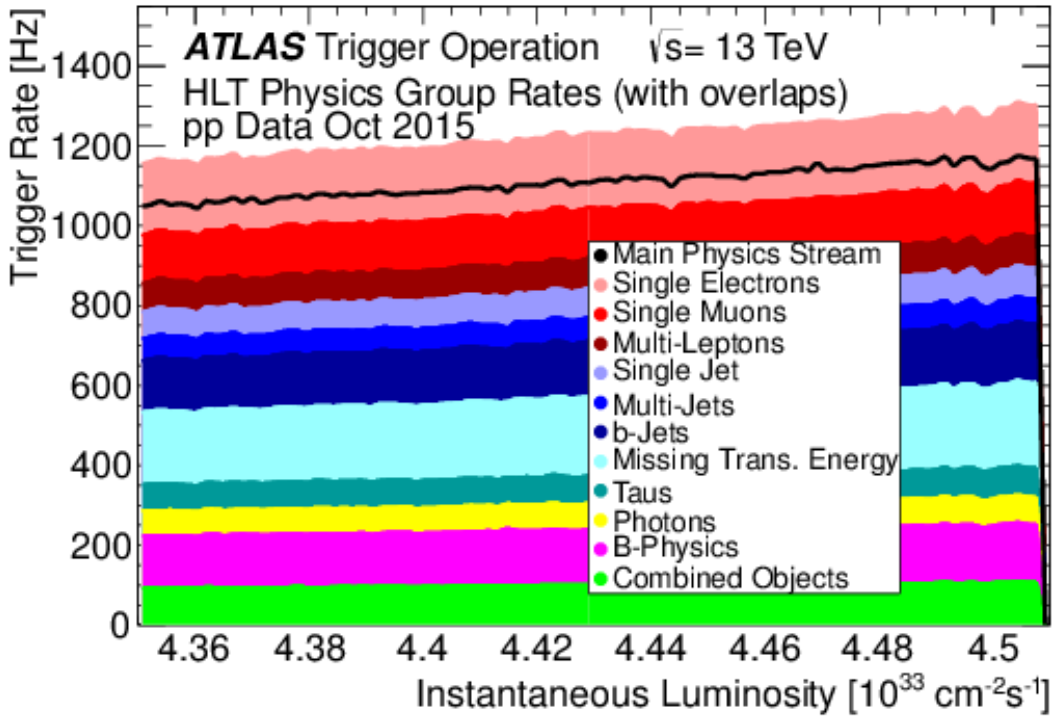

Figure A.3: Trigger rates of various HLT triggers as a function of instantaneous luminosity in a fill taken in October 2015 with a peak luminosity of $\mathcal{L} = 4.6 \times 10^{33}\,\mathrm{cm}^{-2}\,\mathrm{s}^{-1}$ and $\langle\mu\rangle = 15$ [39].

A.6 Author's contributions to HLT $E_{\mathrm{T}}^{\mathrm{miss}}$ trigger

The author made substantial contributions to upgrading, maintaining, and continually assessing the performance of the HLT $E_{\mathrm{T}}^{\mathrm{miss}}$ trigger:

- implemented the η-ring pileup subtraction and χ^2 minimization-based pileup correction algorithms,
- assisted in migrating the trigger to use the xAOD event data model,
- fixed issues with the trigger during operation,
- produced and assessed trigger validation plots during operation,
- implemented derivation streams (automatic reprocessing of data with cuts appropriate for $E_{\mathrm{T}}^{\mathrm{miss}}$ trigger performance studies).

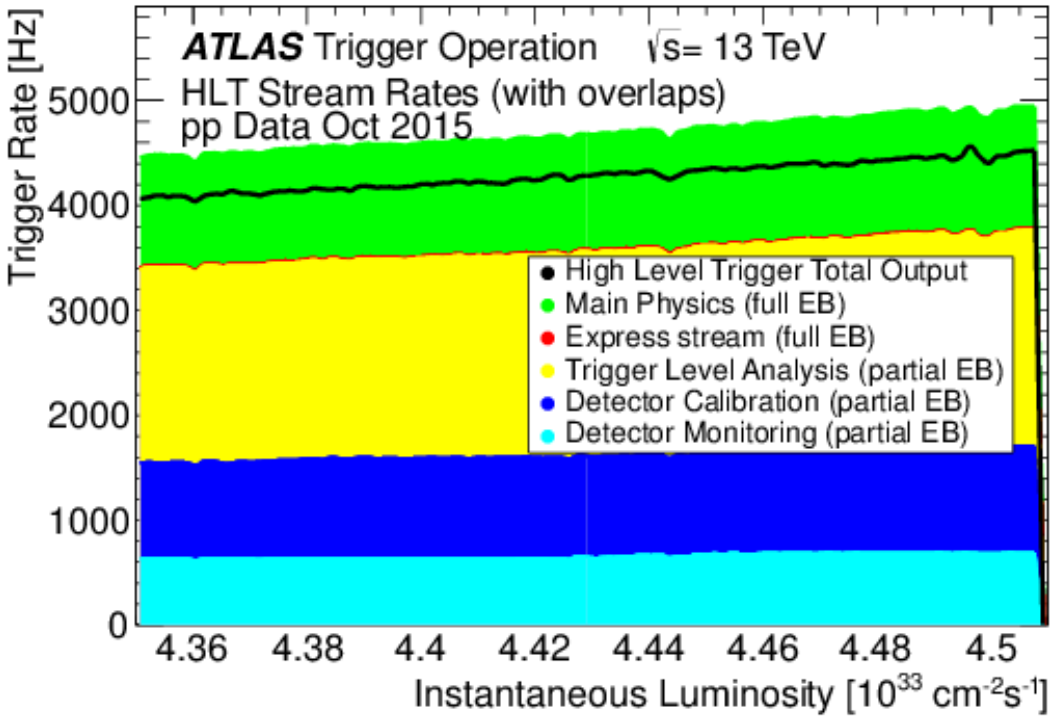

Figure A.4: Total and individual stream trigger rates as a function of instantaneous luminosity in a fill taken in October 2015 with a peak luminosity of $\mathcal{L} = 4.6 \times 10^{33}\,\mathrm{cm}^{-2}\,\mathrm{s}^{-1}$ and $\langle\mu\rangle = 15$ [39].

A.7 Author's contributions to $E_{\mathrm{T}}^{\mathrm{miss}}$ trigger monitoring

The author also made substantial contributions to upgrading and maintaining the HLT $E_{\mathrm{T}}^{\mathrm{miss}}$ trigger monitoring software:

- implemented $W \to e\nu$ and $W \to \mu\nu$ signal selections in the offline monitoring framework. These selections are automatically performed on a run-to-run basis and are used by trigger "expert" shifters to assess the performance of the trigger in operation.
- Assisted in migrating the trigger monitoring software to use the xAOD event data model,
- fixed issues with the trigger monitoring software.

Glossary

$E_{\mathbf{T}}^{\mathbf{miss}}$**, MET** Missing transverse momentum.

$H_{\mathbf{T}}^{\mathbf{miss}}$**, MHT** Missing transverse hadronic momentum.

η**, Pseudorapidity** Coordinate that is Lorentz invariant under boosts, given by $\eta = -ln(\theta/2)$, where θ is the polar angle.

eV**, electronvolt** Unit of energy equal to 1.6×10^{-19} J. The amount of energy gained by an electron after being accelerated by 1 V of electric potential..

pb**, Picobarn** Unit of area equal to $10^{-40}\,\mathrm{m}^2$ and the unit of cross-section.

pb^{-1}**, Inverse picobarn** Unit of inverse area equal to $10^{40}\,\mathrm{m}^{-2}$ and the unit of integrated luminosity.

ASIC Application specific integrated circuit.

B-tagging Process identifying jets originating from bottom quarks.

Bunch crossing Collision of proton bunches in the detector.

Bunch spacing Time between two consecutive bunch crossings..

Cross-section Interaction probability of a physics process per unit flux.

FEX Feature extraction algorithm.

FPGA Field programmable gate array.

GEANT Detector simulator used in ATLAS analyses to simulate detector response. Does not simulate event generation nor object formation or triggering.

L1A Level-1 accept signal.

LHC Large Hadron Collider.

NNLL NNLL: Next-to-next-to-leading-logarithmic order.

NNLO NNLO: Next-to-next-to-leading order.

Pileup Background effects arising from multiple interactions per bunch crossing.

Prescale Filter that reduces trigger rate by accepting only a fraction of events.

PYTHIA Monte Carlo event generator used in ATLAS analyses to simulate interactions. Does not simulate detector.

QCD Quantum chromodynamics: the theory of strong interactions.

QED Quantum electrodynamics: the theory of electromagnetic interactions.

Topocluster Clustering of cells built using the topological clustering algorithm.

Vertexing Process of finding the vertices from which tracks originate.

Bibliography

[1] G. Aad and Others, *Search for dark matter in events with a hadronically decaying W or Z boson and missing transverse momentum in pp collisions at $\sqrt{s} = 8$ TeV with the ATLAS detector*, Phys.Rev.Lett. **112** (2014) 41802, arXiv:1309.4017 [hep-ex].

[2] G. Aad and Others, *Search for dark matter candidates and large extra dimensions in events with a jet and missing transverse momentum with the ATLAS detector*, JHEP **1304** (2013) 75, arXiv:1210.4491 [hep-ex].

[3] G. Aad and Others, *Search for supersymmetry at $\sqrt{s}$=8 TeV in final states with jets and two same-sign leptons or three leptons with the ATLAS detector*, JHEP **1406** (2014) 35, arXiv:1404.2500 [hep-ex].

[4] G. Aad and Others, *Search for squarks and gluinos with the ATLAS detector in final states with jets and missing transverse momentum using 4.7 fb^{-1} of $\sqrt{s} = 7$ TeV proton-proton collision data*, Phys.Rev. **D87** (2013) 12008, arXiv:1208.0949 [hep-ex].

[5] G. Aad and Others, *Search for charged Higgs bosons decaying via $H^+ \to \tau\nu$ in top quark pair events using pp collision data at $\sqrt{s} = 7$ TeV with the ATLAS detector*, JHEP **1206** (2012) 39, arXiv:1204.2760 [hep-ex].

[6] G. Aad and Others, *Search for the Standard Model Higgs boson produced in association with a vector boson and decaying to a b-quark pair with the ATLAS detector*, Phys.Lett. **B718** (2012) 369–390, arXiv:1207.0210 [hep-ex].

[7] G. Aad and Others, *Measurement of the W to $\tau\nu$ Cross Section in pp Collisions at $\sqrt{s} = 7$ TeV with the ATLAS experiment*, Phys.Lett. **B706** (2012) 276–294, arXiv:1108.4101 [hep-ex].

[8] G. Aad and Others, *Measurement of τ polarization in $W->\tau\nu$ decays with the ATLAS detector in pp collisions at sqrt(s) = 7 TeV*, Eur.Phys.J. **C72** (2012) 2062, arXiv:1204.6720 [hep-ex].

[9] ATLAS Collaboration, *Run-2 public event displays*, https://twiki.cern.ch/twiki/bin/view/AtlasPublic/EventDisplayRun2Collisions.

[10] K. A. Olive and Others, *Review of Particle Physics*, Chin. Phys. **C38** (2014) 90001.

[11] ATLAS Collaboration, *Standard Model public results*, https://twiki.cern.ch/twiki/bin/view/AtlasPublic/StandardModelPublicResults.

[12] S. Dittmaier and Others, *Handbook of LHC Higgs Cross Sections: 1. Inclusive Observables*, arXiv:1101.0593 [hep-ph].

[13] ATLAS Collaboration, *Run-2 luminosity public results*, https://twiki.cern.ch/twiki/bin/view/AtlasPublic/LuminosityPublicResultsRun2.

[14] G. Aad and Others, *Topological cell clustering in the ATLAS calorimeters and its performance in LHC Run 1*, arXiv:1603.02934 [hep-ex].

[15] CERN, *Luminosity Calibration calculator*, https://lpc.web.cern.ch/lumi2.html.

[16] CERN, *Layout of accelerators and detectors at CERN*, http://te-dep-epc-oms.web.cern.ch/te-dep-epc-oms/general-fr/pagesources/Cern-Accelerator-Complex.jpg.

[17] G. Aad and Others, *The ATLAS Experiment at the CERN Large Hadron Collider*, JINST **3** (2008) S08003.

[18] V. A. Mitsou, *The ATLAS transition radiation tracker*, pp. , 497–501. 2003. arXiv:hep-ex/0311058 [hep-ex]. http://weblib.cern.ch/abstract?ATL-CONF-2003-012.

[19] G. Aad and Others, *The ATLAS Inner Detector commissioning and calibration*, Eur. Phys. J. **C70** (2010) 787–821, arXiv:1004.5293 [physics.ins-det].

[20] Y. Takubo, *The Pixel Detector of the ATLAS experiment for the Run2 at the Large Hadron Collider*, JINST **10** (2015) C02001, arXiv:1411.5338 [physics.ins-det].

[21] M. Capeans, G. Darbo, K. Einsweiller, M. Elsing, T. Flick, M. Garcia-Sciveres, C. Gemme, H. Pernegger, O. Rohne, and R. Vuillermet, *ATLAS Insertable B-Layer Technical Design Report*, Tech. Rep. CERN-LHCC-2010-013. ATLAS-TDR-19, CERN, Geneva, Sep, 2010. https://cds.cern.ch/record/1291633.

[22] G. Aad and Others, *Operation and performance of the ATLAS semiconductor tracker*, JINST **9** (2014) P08009, arXiv:1404.7473 [hep-ex].

[23] A. Andronic and J. Wessels, *Transition radiation detectors*, Nuclear Instruments and Methods in Physics Research A **666** (2012) 130–147, arXiv:1111.4188 [physics.ins-det].

[24] N. Nikiforou, *Performance of the ATLAS Liquid Argon Calorimeter after three years of LHC operation and plans for a future upgrade*, in *Proceedings, 3rd International Conference on Advancements in Nuclear Instrumentation Measurement Methods and their Applications (ANIMMA 2013)*. 2013. arXiv:1306.6756 [physics.ins-det]. https://inspirehep.net/record/1240499/files/arXiv:1306.6756.pdf.

[25] R. Wigmans, *Calorimetry: Energy Measurement in Particle Physics*. International series of monographs on physics. Clarendon Press, 2000. https://books.google.ca/books?id=vD9RFluMD5sC.

[26] M. Swiatlowski, *Light-quark and Gluon Jet Discrimination in pp Collisions at $\sqrt{s} = 7$ TeV with the ATLAS Detector*, https://cds.cern.ch/record/1708873.

[27] CERN, *Proc. of the 1998 European School of High-Energy Physics*. CERN, Geneva, 1999. https://cds.cern.ch/record/342530.

[28] G. Aad and Others, *Jet energy measurement with the ATLAS detector in proton-proton collisions at $\sqrt{s} = 7$ TeV*, Eur. Phys. J. **C73** (2013) 2304, arXiv:1112.6426 [hep-ex].

[29] G. Aad and Others, *Jet energy resolution in proton-proton collisions at $\sqrt{s} = 7$ TeV recorded in 2010 with the ATLAS detector*, Eur. Phys. J. **C73** (2013) 2306, arXiv:1210.6210 [hep-ex].

[30] G. Aad and Others, *Muon reconstruction performance of the ATLAS detector in proton–proton collision data at $\sqrt{s}$ =13 TeV*, Eur. Phys. J. **C76** (2016) 292, arXiv:1603.05598 [hep-ex].

[31] Y. Nakahama, *The ATLAS Trigger System: Ready for Run-2*, J. Phys. Conf. Ser. **664** (2015) 82037.

[32] M. Palka, *Operation of the enhanced ATLAS First Level Calorimeter Trigger at the start of Run-2*, JINST **11** (2016) C02059.

[33] M. Cacciari, G. P. Salam, and G. Soyez, *The Anti-k(t) jet clustering algorithm*, JHEP **04** (2008) 63, arXiv:0802.1189 [hep-ph].

[34] G. Aad and Others, *Measurement of $W^{\pm}$ and Z-boson production cross sections in pp collisions at $\sqrt{s} = 13$ TeV with the ATLAS detector*, Phys. Lett. **B759** (2016) 601–621, arXiv:1603.09222 [hep-ex].

[35] M. Aaboud and Others, *Measurement of the $t\bar{t}$ production cross-section using $e\mu$ events with b-tagged jets in pp collisions at $\sqrt{s}$=13 TeV with the ATLAS detector*, Phys. Lett. **B761** (2016) 136–157, arXiv:1606.02699 [hep-ex].

[36] ATLAS Collaboration, *ATLAS MET Trigger Rate/Cross-section Monitor*, https://rewang.web.cern.ch/rewang/xmon/cgi-bin/xmon.cgi.

[37] ATLAS Collaboration, *Jet global sequential corrections with the ATLAS detector in proton–proton collisions at $\sqrt{s} = 8$ TeV*, ATLAS-CONF-2015-002, 2015, http://cdsweb.cern.ch/record/2001682.

[38] A. Daniells and I. Hristova, *Level-1 Missing E_T Trigger Rates from high luminosity simulation*, Tech. Rep. ATL-COM-DAQ-2013-150, CERN, Geneva, Nov, 2013. https://cds.cern.ch/record/1631717.

[39] ATLAS Collaboration, *Trigger operation public results*, https://twiki.cern.ch/twiki/bin/view/AtlasPublic/TriggerOperationPublicResults.